WATER SORPTION HYSTERESIS AND WOOD CELL WALL NANOPORE STRUCTURE

by

Jingbo Shi

B.Eng., M.Sc., Nanjing Forestry University, 2011

A THESIS SUBMITTED IN PARTIAL FULFILLMENT OF
THE REQUIREMENTS FOR THE DEGREE OF

DOCTOR OF PHILOSOPHY
in
THE FACULTY OF GRADUATE AND POSTDOCTORAL STUDIES
(Wood Science)

THE UNIVERSITY OF BRITISH COLUMBIA
(Vancouver)

May 2017

Abstract

The origin of sorption hysteresis in the wood-water system is still under debate. In this study, cell walls are considered as micro-mesoporous materials and capillary condensation in the entire hygroscopic region is proposed as an alternative sorption mechanism.

Initially, the pore connectivity was investigated by observing five experimentally generated hysteresis patterns at 25 and 40^{o}C. Consistent patterns were found for the species-temperature combinations. Further, the satisfactory congruency and wiping-out properties indicate the dominance of independent cell wall pores. After this experimental phase, the geometric interpretations derived from the Preisach model, the mathematical form of the independent domain model, was used to explain the observed hysteresis patterns. Additionally, a modification to the aforementioned model was suggested that involves a numerical implementation, which avoids the use of unknown parameters. The low prediction errors and well-maintained wiping-out property support the suitability of our approach.

In the next phase, grand canonical Monte Carlo (GCMC) technique was applied in a simplified wood-water system to simulate sorption isotherms and hysteresis at 25 and 40°C. In the simulation system, wood is represented by a cell wall model that is composed of solid substances and evenly distributed independent cylindrical nanopores with sizes in the range of 0.6 – 2.2nm. Two types of pore-wall compositions regarding polysaccharides and lignin have been considered. The hydroxyl groups are modeled as negative energy pits attached to walls whereas water is represented by the SPC/E model. Results demonstrated that hysteresis can be well explained by the existence of metastable states associated with capillary condensation and evaporation of water

in cell wall pores. The alternative sorption mechanism driven by capillary condensation is also strongly supported by the simulation.

In the last phase, the cell wall pore size distributions in the hygroscopic range were explored for the three species from a "trial and error" calculation approach. This approach was indirectly examined by comparing derived volumetric strain of cell walls and the density of adsorbed water in the hygroscopic range with literature data. The qualitative agreement indicates the soundness of assumptions made on the cell wall swelling process and proposed calculation procedures.

Lay Summary

The key goal of this project was to investigate a long-standing problem in wood science, namely, the water sorption hysteresis. The fundamental explanation of sorption hysteresis helped us identify the relationship between the hysteresis and cell wall nanostructure. Then, we focused on the water behavior inside the wood cell walls and used water molecules to unlock the wall structure. The molecular simulation approach was applied to overcome the challenges brought in by nanoscale confinement caused by cell wall nanopores. Significant insight regarding the sorption process was gained through the simulations. One of the main findings is that the water sorption is more likely to be driven by capillary condensation, rather than the formation of monolayer water or water clusters. Our findings contribute to a better understanding of water sorption in wood, cell wall nanostructure and subsequent application to wood products in service.

Preface

In this research program, I identified the research questions, and designed and executed all experiments. I performed all testing and analysis regarding experimental data, modeling and simulations.

A version of chapters 2, 3, 4 and 5 has been accepted for publication.

Shi, J., Avramidis, S. (2017) Water sorption hysteresis in wood: I review and experimental patterns — geometric characteristics of scanning curves. Holzforschung 71(4): 307-316.

Shi, J., Avramidis, S. (2017) Water sorption hysteresis in wood: II mathematical modeling — functions beyond data fitting. Holzforschung 71(4): 317-326.

Shi, J., Avramidis, S. (2017) Water sorption hysteresis in wood: III physical modeling by molecular simulation. Holzforschung (accepted April 2017).

I conducted all the testing and analysis, and wrote most of the manuscripts.

Table of Contents

List of Tables

List of Figures

List of Symbols

c	concentration of probe solution (g solute/g solution)
C_v	a constant in the volume strain calculation
d_p	diameter of the simulated pore (nm)
d_{eff}	effective diameter of the simulated pore (nm)
e	elementary charge, approximately 1.602 × $10-^{19}$C
F	Helmholtz free energy (J)
G	a defined function based on the moisture content values from the boundary ascending curve and primary descending curves
H	relative humidity (%)
j	the volume weight for the simulated pore
k_B	Boltzman constant (1.38066×10^{-23}J K^{-1})
L	the interface line in the geometric interpretation of the Preisach model
l_p	simulated pore length
M	moisture content (%)
MOE	modulus of elasticity (MPa)
MSE	defined mean of squared error for model evaluation
N_A	Avogadro constant (6.02×10^{-23})
N_s	number density of wall atoms (m^{-3})
$NMSE$	defined normalized mean of squared error for model evaluation
n_{HB}	number of sorption sites
nps_c	number of pits in the lateral direction of the simulated pore

nps_l	number of pits in the longitudinal direction of the simulated pore
p	pressure (Pa)
p_0	saturated pressure at a constant temperature (Pa)
q	particle charge (C)
PSD	pore size distribution
Q	released heat (J)
r	displacement between two LJ particles (nm)
R	gas constant (8.314J mol^{-1} K)
R_p	the radius of the simulated sphere pore (nm)
r_p	radius of the simulated cylindrical pore (nm)
s_1	the distance of the water molecule from the pore center (nm)
S^+	the subdivision of T with operators $\hat{\gamma}_{ul}$ equal to 1
S^-	the subdivision of T with operators $\hat{\gamma}_{ul}$ equal to 0
SSE	defined sum of squared error for model evaluation
t_c	the thickness of adsorbed films prior to condensation (nm)
T	the focused half-plane in the geometric interpretation of the Preisach model
U	the internal or interaction energy (J)
u_{LJ}^{ij}	the LJ potential energy between particle i and j with (J)
V	volume (m^3)
V_L	mole volume of the bulk liquid (m^3/mol)
v	specific volume (cm^3/g)
w	mass (g)

W	the width of the simulated slit pore (nm)
x	the distance of the water molecule from the left wall in the slit pore model (nm)
ρ	density (g cm^{-3})
δ	total cell wall pore volume (cm^{-3})
ϕ	cell wall porosity
λ	wave length (nm)
θ	angle (°)
μ	chemical potential (J/particle)
ξ	weight function in the Preisach model
Ω	the grand thermodynamic potential (J)
$\hat{\gamma}$	elementary hysteresis operator in the Preisach model
τ	temperature (°C)
ω	the maximum or minimum value of input relative humidity (%)
γ	surface tension of the liquid (J m^{-2})
ε	one of the LJ potential parameter: the depth of the minimum energy well (J)
ε_v	volumetric strain of wood (%)
ε_{vcw}	volumetric strain of the cell walls (%)
σ	another LJ potential parameter: the collision diameter (nm)
Δ	the distance of two neighboring layers of the slit pore wall (nm)
χ	mean value of the pore sizes (nm)
ψ	standard deviation of the pore sizes (nm)

List of Abbreviations

BET	Brunauer–Emmett–Teller
D-fir	Douglas-fir
DBdB	Derjaguin-Broekhoff-de Boer
dtMC	discrete time Markov chains
DFT	density function theory
DSC	differential scanning calorimeter
DVS	Dynamic Vapor Sorption
emc	equilibrium moisture content
FSD	the mathematical hysteresis model developed by Frandsen et al. (2007)
fsp	fiber saturation point
GCMC	Grand Canonical Monte Carlo
HPLC	high-performance liquid chromatograph
IDM	independent domain model
IUPAC	International Union of Pure and Applied Chemistry
LJ	Lennard-Jones
MF	microfibrils
MPM-A	a version of modified Preisach model
MPM-B	another version of modified Preisach model
NMR	nuclear magnetic resonance
P-model	Preisach model
PAC	pores associated with cellulose

PAH	pores associated with hemicellulose
PAL	pores associated with lignin
PAT	total cell wall pores
PW	pore wall substance
PEG	polyethylene glycols
SPC/E	extended simple point charge water model
TAPPI	Technical Association of the Pulp and Paper Industry
UBC	University of British Columbia
WRC	western red cedar

Acknowledgements

I would like to acknowledge my supervisor Dr. Stavros Avramidis, who introduced me to the field of wood physics, a fantastic interesting and challenging area. Thank you for securing a NSERC grant to study the fundamental wood-water relationship and supporting me for five years. I am very glad that we went through this project together.

I offer my enduring gratitude to my committee members: Dr. Savvas Hatzikiriakos, Dr. Frank Lam and Dr. Gregory Smith. Thank you for being with me since Feb. 2013. You taught me humbleness and patience, some qualities I am still learning. Your questioning and high expectations made this research way better.

For experimental works, I owe thanks to Diana Hastings, Winfield Liu, Lawrence Gunther, Vincent Leung, George Lee and Foster Hart in the Department of Wood Science, Sally Finora in the Department of Mining Engineering, Dr. Guillaume Bussiere in the Department of Chemistry. For simulation works, special thanks go to Dr. Aleksey Vishnyakov at Rutgers University, and Vasilii Triandafilidis in the UBC-Department of Chemical and Biological Engineering.

Many thanks to every group member and friend I met since May 2012. Special thanks go to Janet Samra and visiting professor Ye Peng.

Special thanks are owed to my parents and sister, who supported me throughout my years in Canada, both morally and financially.

Dedication

To those pioneers in wood physics,

whose works always inspire me.

Chapter 1: Introduction

1.1 Water in Wood

From its presence in trees to every stage in processing and use, water is an indispensable part of the xylem matrix and directly affects service performance. Therefore, when considering wood properties and utilization, the amount of water in it must always be considered.

Wood is a porous and hygroscopic biopolymer of anisotropic nature that swells or shrinks when it gains or loses water within the hygroscopic range, i.e. water concentration from 0% to about 30% dry-basis. This dimensional instability could result in significant performance and service life length problems. That is because almost all wood properties (mechanical, thermal, electrical, adhesion, machining, etc.) are strongly affected by the type and quantity of water in wood.

That water in wood is found in two different forms, namely, free water in the cell lumens and bound water within the cell walls. Moisture content of wood (M), numerically defines the amount of water present in wood as a percentage of its oven-dry weight and can range from 0% up to 300% and few times, beyond that. The fiber saturation point (M_{fsp}), is defined as the moisture content (taken as 30% for practical purposes) at which all the water in the lumen has been removed, but at which the cell walls are still fully saturated (Tiemann 1906). That M_{fsp} is a crucial point where these two forms of water can be practically distinguished and where abrupt property changes are observed. According to this definition, below M_{fsp} (M = 0 to 30% commonly called the "hygroscopic range"), only bound water exists, whereas, above M_{fsp}, both bound and free water co-exist. Above M_{fsp}, there is also no appreciable change in many physical and mechanical properties of wood—it is the water in the cell walls (bound water) that enormously affects the properties of wood.

1.2 Water Sorption Isotherm and Hysteresis

A basic method to study water in wood is to observe and analyze the water sorption isotherm. Wood will adsorb or desorb water to achieve an equilibrium state in a specific relative humidity (*H*) environment. This *M–H* relationship under constant temperature for the whole *H* spectrum of 0 to 100% is called the water sorption isotherm.

There are six types of sorption isotherms (Fig. 1.1) according to the classification of International Union of Pure and Applied Chemistry (IUPAC) (Gregg and Sing 1982).

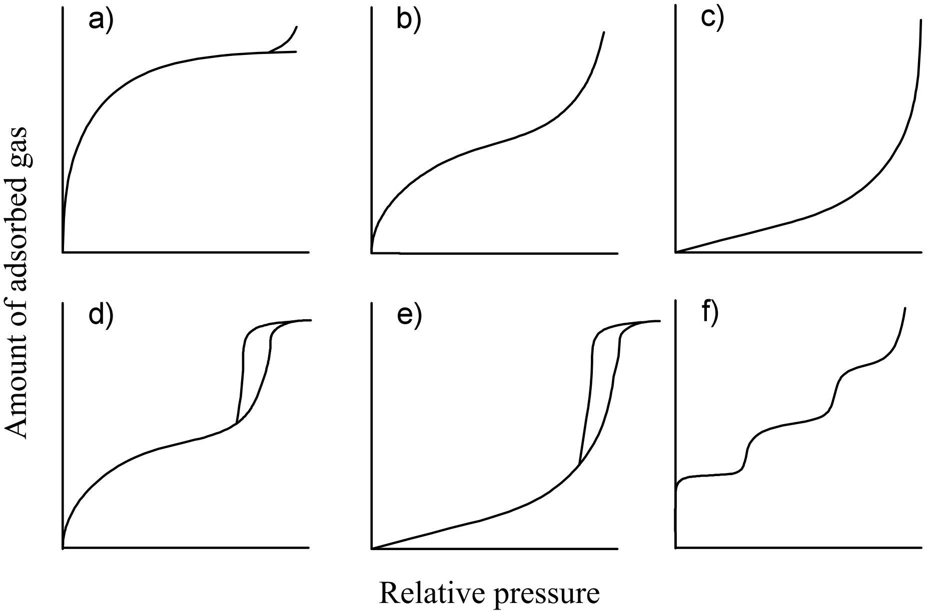

Figure 1.1: a) – f), type I to type VI sorption isotherms.
Modified from Fig. 1.1 in Gregg and Sing (1982).

The isotherm of wood water sorption is represented by a sigmoid curve (Fig. 1.2) that belongs to Type II sorption isotherm. The upper curve in Fig. 1.2 is called the desorption isotherm, representing the process when wood loses water while it is exposed to a lower H, whereas the lower curve is called the adsorption isotherm, representing the opposite process. The difference between the two curves at the same temperature is defined as hysteresis, an important phenomenon that has been recognized since the early 20th century (Pidgeon and Maass 1930, Seborg and Stamm 1931). The magnitude (or size) of the hysteresis loop can be calculated as $\frac{M_{des}-M_{ads}}{M_{ads}}$, where M_{des} and M_{ads} are the equilibrium moisture contents (M_{emc}) at specified Hs in the desorption and adsorption process, respectively.

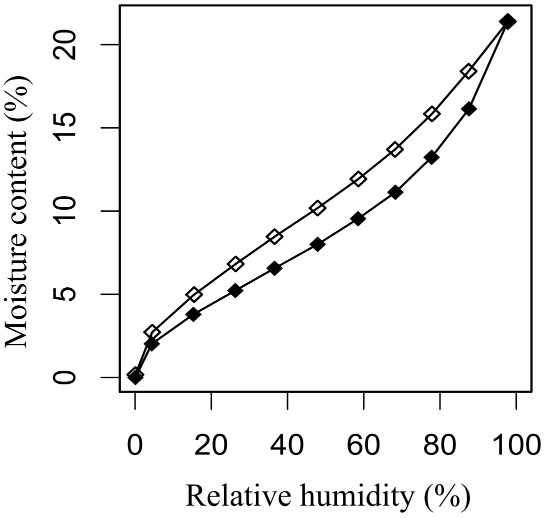

Figure 1.2: Sorption isotherm and hysteresis of a Douglas-fir wood powder sample at 24.8°C. Solid and open symbols represent the adsorption and desorption process, respectively.

The hysteresis loop is limited by the adsorption-desorption curves otherwise called boundary curves, namely, ascending and descending, respectively (Fig. 1.3). Furthermore, families of ascending and descending curves within the boundary curves are defined as scanning curves. The primary descending curve starts from the boundary ascending curve; similarly, the primary ascending curve starts from the boundary descending curve (Fig. 1.3). The secondary descending curve starts from the primary ascending curve, and the secondary ascending curve starts from the primary descending curve (Fig. 1.3); and so forth.

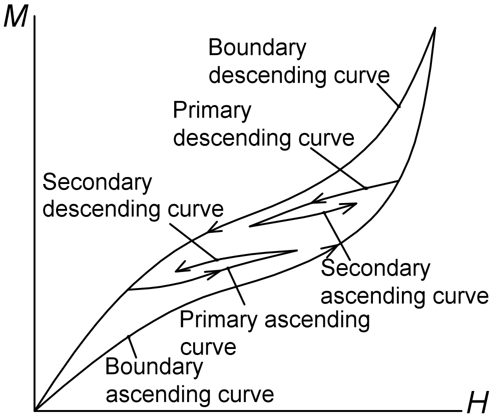

Figure 1.3: Definition of scanning curves.

1.3 Motivation

The origin of hysteresis and its relationship to cell wall nanostructure is still open to debate. The emerging nanoporous material and sorption science, provide significant insight into relating hysteresis to the cell wall pore structure. Not only does it provide an attractive alternative explanation of the hysteresis mechanism, but it also suggests a theoretical way of probing the cell wall pore structure.

The elucidation of nanoscale cell wall architecture, and especially its variation with *M*, is a long-standing conundrum in wood and plant science. Recently, more and more effort is devoted to better understand the cell wall organization, largely due to the growing need for biofuels and bioproducts with better in-service performance and higher strength that are also carbon neutral. However, the interaction of cell wall biopolymers and a far more complicated biosynthetic process are making this task very challenging. The hysteresis-based approach can fully take advantage of modeling and simulation, thus appropriately simplifying the study of cell wall-water system.

1.4 Objectives

The aim of this study was the understanding of the underlining physical phenomena related to water sorption hysteresis in wood under isothermal conditions and its relationship to cell wall porosity evolution during sorption. Specifically, the study is divided into four phases each with the following sub-objective,

1. to reveal the basic physicochemical phenomena that underline hysteresis;
2. to develop a mathematical model which can accurately predict scanning curves;
3. to develop a physical model that can describe and predict the mechanisms that give rise to hysteresis, and;
4. to predict pore sizes and distributions of the major cell wall polymers from the developed physical model.

1.5 Methodology

This research was carried out in four phases: experimental, mathematical modeling, physical modeling, and cell wall pore structure analysis. The point of origin of this thesis is a proposed hysteresis theory based on common features shared by wood and nanoporous materials like zeolites and silicates. Firstly, the proposed theory was examined during the experimental phase through systematic observation of scanning curve geometric characteristics. Material characterization regarding cell wall density, porosity, pore size distribution, chemical composition and crystallinity was also included in this phase. Then, in phase two, a mathematical model was developed to explain those geometric characteristics, and predict the scanning curves quantitatively. In phase three, a physical model was constructed to simulate the sorption and hysteresis. The focus of this phase was origin of hysteresis, a further examination of the proposed theory. In the last phase, the cell wall pore structure was explored through the developed physical model.

1.6 Deliverables

Firstly, the explanation and modeling of sorption hysteresis was largely advanced. It was the first time that the geometric characteristics of high-order scanning curves were thoroughly studied. The collected sorption data were highly valuable in assessing the developed model in this study and previous models in literature. Secondly, the elucidated cell wall pore structure could provide new insights into the formation, deformation, modification, and degradation of cell walls, and inspire the development of new techniques to better characterize cell walls experimentally.

Chapter 2: Literature Review and Proposed Theory

This chapter is dedicated to the review the sorption hysteresis theories in literature, and the introduction of the proposed theory. The specific review on mathematical and physical modeling of hysteresis will be presented in the introduction of chapters 4 and 5, respectively.

2.1 Literature Review of Sorption Hysteresis in Wood

2.1.1 Characteristics of hysteresis loops

Sorption hysteresis has been observed in many systems (e.g., sorption of nitrogen or argon in active carbons, zeolites and silica etc., and water sorption in biological systems such as soil and food), with curve loops of different shapes and sizes (Gregg and Sing 1982, Basu et al. 2006,

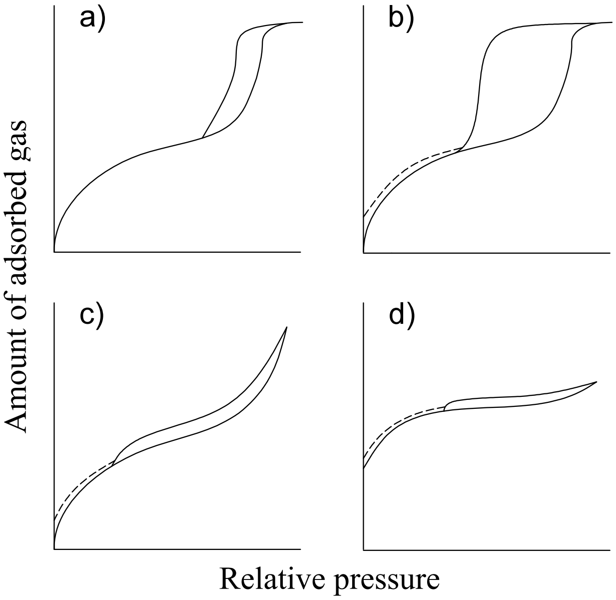

Figure 2.1: a) – d), type H1 – H4 hysteresis loops. Modified from Fig. 4.8 in Lowell et al. (2004).

Arthur et al. 2016). Fig. 2.1 illustrates an empirical classification of hysteresis loops, namely, H1, H2, H3, and H4, was given by the IUPAC (Lowell et al. 2004). For the wood-water system, this phenomenon has been observed and modeled from the early 20th century (Pidgeon and Maass 1930; Seborg and Stamm 1931; Peralta 1995b; Carmeliet et al. 2005; Frandsen et al. 2007).

Fundamentally, there are three typical characteristics in hysteresis loops of wood. Firstly, there are two types of hysteresis ─ the irreproducible one from the green or rewetted states and the reproducible one from the subsequent sorption cycles (Fig. 2.2).

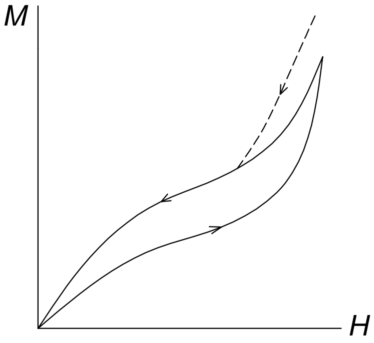

Figure 2.2: An illustration of irreproducible sorption hysteresis loop (dashed line) and reproducible one (solid line).

The reproducibility has been confirmed by repeating the full sorption consecutive cycles twice or thrice using dynamic sorption for most species, with the exception of larch latewood (*Larix kaempferi* Lamb.) (Jalaludin 2012; Hill et al. 2012b, 2015; Popescu and Hill 2013; Kymäläinen et al. 2015). Secondly, the distinction between the first desorption curve from green state with the subsequent desorption curves is only possible in the upper *H* range (i.e. above 60%) (Spalt 1958; Hartley 1994). However, the reproducible hysteresis exists in the entire hygroscopic range. Thirdly, the reproducible hysteresis loop seems to present a combined feature of types H1, H3 and

H4, which makes its classification complicated. It is reasonable therefore, to look for specific explanations for irreproducible and reproducible hysteresis.

2.1.2 Origin of hysteresis

The irreproducible hysteresis was explained as forming a more compact gel-structure caused by bonds between active groups in the first desorption process (Urquhart 1929; Spalt 1958). Recent drying studies on green wood and pulp by deuterium-hydrogen exchange coupled with FT-IR analysis demonstrated that water removal in the primary drying process leads to irreversible alterations of the cell wall structure, namely, part of accessible hydroxyl groups in the green state became inaccessible after initial drying (Suchy et al. 2010a, 2010b). This observation supports the above-mentioned hypotheses.

The origin of reproducible hysteresis (subsequently called “hysteresis”) is still open to debate. A classical explanation, firstly proposed by Urquhart (1929), attributes that to reduced sorption sites in the adsorption processes due to lateral hydroxyl bonding. The initial water molecular layer forms by direct bonding to wood hydroxyls, and is commonly named “monolayer” water. Spalt (1958) firstly questioned this explanation based on his analysis that total hysteresis over the entire hygroscopic range is predominantly influenced by water in multilayers rather than in a monolayer. This explanation has been challenged by the relationship between the number of accessible hydroxyls and H. Taniguchi et al. (1978) found by the hydrogen-deuterium exchange method that the quantity of accessible hydroxyls increased with H and reached a maximum at around 60%. Accordingly, in the hygroscopic range above 60% H, hysteresis is not caused by different numbers of sorption sites. Moreover, the compelling role of accessible hydroxyls in the overall M_{emc} is also questionable. Rautkari et al. (2013) reported a poor correlation between the quantities of accessible hydroxyls and M_{emc} , and suggested the consideration of additional sorption mechanisms.

Alternatively, Spalt (1958) described hysteresis as "the outgrowth of two series of equilibrium gel configurations attained by cell wall polymers, starting in one instance from a dispersed state, and in the other, from a more highly aggregated state". Chen and Wangaard (1968) explained hysteresis from the perspective of capillary condensation in the upper hygroscopic range ($H > 60\%$). The authors assumed that different contact angles, namely, the advancing angle in the adsorption process and the receding angle in the desorption process, caused hysteresis. Chirkova et al. (2007) proposed that hysteresis in wood is caused by the low modulus of elasticity (*MOE*) of cell walls, "whose pores were closed upon removal of a part of the sorbate, blocking the complete release of the sorbate from the sorbent's pores". Hill et al. (2010) explained hysteresis from the time lag in reaching thermodynamic equilibrium states for the cell wall molecular configurations, which are disturbed by incoming and departing water molecules in the adsorption and desorption process. An attractive part of this theory is that the time lag could be related to the rigidity of the cell wall and the rigidity could be further related to the lignin composition due to its cross-linking structure. According to this theory, more lignin content would cause more hysteresis, which is consistent with the observed relationship between lignin content and the magnitude of hysteresis (Hill et al. 2009, 2010, 2012a). The lag time is temperature dependent, and the theory could explain the decrease of hysteresis magnitude with temperature rise and capable to also predict the disappearance of hysteresis above the glass transition temperature (T_g).

2.2 Theory Development Foundation

The proposed theory, existence of metastable states in capillary condensation of cell wall pores, arises from the micro-mesoporous nature of the wood cell wall and sorption studies of nanoporous materials like zeolites and silicates.

2.2.1 Simplification of swelling of cell walls

The hysteresis interpretation is largely complicated by the swelling and shrinkage behavior (i.e. dimensional instability) of cell walls as a function of *M*. Focusing on the final equilibrium states, the swelling leads to different pore size distributions at different *M*s, and then each point at the gross sorption isotherm can be obtained by superimposition of individual sorption isotherms at each specific pore size. In summary, without considering the details of the swelling process, the cell walls can be treated as a non-swelling porous material.

2.2.2 Sorption studies on nanoporous materials

The wood cell wall can be considered as a micro-mesoporous material. Research under this premise, at dried and fully swollen wall states has indicated that in the hygroscopic range, pore sizes are in the range of 0.6 – 4nm, and the average pore size becomes larger at higher *M*s (Stone and Scallan 1968; Papadopoulos 2005; Hill 2006; Kojiro et al. 2010). According to IUPAC's pore classification system, part of wood cell walls falls into the category of micropores (< 2nm) whereas the rest falls into the mesopores (2 – 50nm) category (Lowell et al. 2004). In this sense, the cell wall is indeed a micro-mesoporous material.

Despite all differences, hysteresis in wood shares some common features with nanoporous materials like zeolites and silicates. Firstly, the magnitude of the hysteresis loop decreases in such materials with decreasing pore size (Kruk et al. 1997; Neimark et al. 1998; Thommes et al. 2000; Ohba and Kaneko 2007). In wood, the magnitude of hysteresis decreases after acetylation and increases after thermal modification (Chirkova et al. 2007; Xie et al. 2011; Hill et al. 2012 b; Olek et al. 2013; Popescu et al. 2014). The pore sizes in the chemically modified cell wall are supposed to be smaller based on the increased crosslinking of wall polymers (Xie et al. 2011), however, the opposite was observed in the thermally modified cell wall (Hietala et al. 2002). Secondly, the magnitude of hysteresis of nanoporous materials decreases with increasing temperature and eventually it disappears (Ravikovitch et al. 1995; Thommes et al. 2000; Tanaka et al. 2013), which is also the case in wood (Kelsey 1957; Hill et al. 2010).

Capillary condensation is an accepted contribution to the sorption mechanism in wood at high H levels (Avramidis 1997), but its occurrence at low and intermediate H levels is questionable. For microporous materials, micropore filling by capillary condensation at very low relative pressure supposed to replace the traditional Langmuir or BET sorption mechanisms (Lowell et al. 2004). Capillary condensation for wood at lower hygroscopic ranges is possible in view of its microporous nature, even though the traditional BET (Skaar 1972) and cluster type (Hartley and Avramidis 1993) sorption mechanisms are difficult to justify at this level.

The independent domain model (IDM) is successful for explaining sorption hysteresis of orderly structured inorganic mesoporous materials such as MCM-41 and SBA-15 (Everett and Whitton 1952; Everett and Smith 1954; Everett 1955; Lowell et al. 2004). This model considers the porous material as an assembly of single, idealized pores that can be filled and emptied independently of its neighbors' influence. Sorption hysteresis is considered the result of the existence of metastable states in each pore-fluid system. The vapor-like and liquid-like metastable states usually occur in the confined fluids before capillary condensation and evaporation as shown from the density function theory and molecular simulations (Neimark et al. 2000; Neimark and Ravikovitch 2001). On the other hand, pore network interactions have to be taken into account for amorphous porous materials, where the independency of pores regardless of their sizes (assumed in the ID-model) does not hold (Ramírez and Sierra 2006; Lilly and Hallock 2001). In a network model, the pore blocking effect during evaporation was evoked to explain hysteresis (Lowell et al. 2004).

2.2.3 Proposed theory

Provided the plausibility of capillary condensation in the wood-water system, the origin of hysteresis could also be the existence of metastable states as described in IDM. If the cell wall pores are interacting, additional pore blocking effects could also be possible. Strategically, it is easier to initially evaluate the pore-pore interaction based on the ID-model, and then, in the second step, consider the pore blocking effect as a possibility.

The IDM has recently been applied to hysteresis modeling of wood (Peralta 1995b, 1996; Derome et al. 2008; Patera et al. 2016). Peralta (1995b) provided two interpretations to "domains" ─ i.e. sorption sites with different degrees of accessibility and micro-capillarity with different pore sizes. The latter one is a good basis to reach an agreement with the postulates of ID-model. However, there is no explicit explanation for the "metastable states".

The initial points of consideration in the present work are that the assumptions in the IDM must be reassessed and more effort should be made to interpret the "metastable states" in wood-water systems. Because the role of sorption sites has been strongly questioned, it is more reasonable to interpret the domains as cell wall pores. The first assumption requires independence of the pores regardless of their size. No experimental technique is available for direct determination of pore size distribution and connectivity in the hygroscopic range when the cell wall is partly saturated with water. Some researchers (Salmén 2004; Stevanic and Salmén 2009; Salmén et al. 2011) have argued that the wall polymers most likely are organized along the microfibrils (MF). Following their arguments, the small voids in polymer structure may connect with each other along the MF direction, which form “infinite” long pores while being independent of each other in the transverse direction. Theoretically, the high *MOE* of cell wall polymers at low *M* (Salmén 2004) indicate high rigidity, which makes pores more likely to behave independently. However, water molecules, acting as plasticizers, will cause the wall polymer chains to become more flexible, a fact that has been detected by NMR experiments (Child 1972; Froix and Nelson 1975). A decreased T_g at high *M*s (Kelley et al. 1987; Östberg et al. 1990; Miki et al. 2012) also supports this supposition. Therefore, at high *M*, the significantly increased mobility of both water molecules and wall polymers might result in a breakdown of the pores’ independence.

The second assumption requires the occurrence of capillary condensation as already discussed above. However, this does not necessarily mean the existence of metastable states like oversaturated vapor-like or liquid-like water. To be sure about their existence, the occurrence of the first order phase transition of water in capillary condensation (Kittel and Kroemer 1980) must be verified. The heat of sorption existence for wood (Kelsey and Clarke 1956) indicates the release of latent heat of water, which characterizes the first order phase transition. More detailed analysis, possibly through molecular simulation (Frenkel and Smit 1996), is needed to evaluate the metastable states and the influence of wall-water interaction and hydrogen bonding.

Further rigorously experimental evidence is needed to support the validity of the IDM in the case of wood. In the following chapter, the evaluation of the pore-pore interaction will be introduced through systematic investigation of scanning curves. Then, in chapter 5, the metastable states will be demonstrated by molecular simulation.

Chapter 3: Experimental: Hysteresis Patterns and Material Characterizations

3.1 Introduction

According to the proposed theory, the interpretation of hysteresis starts from the evaluation of the cell wall pore-pore interaction. This can be accomplished by experimental investigations on the geometric characteristics of scanning curves. The steep slopes seen in primary descending curves are supposed to be suitable indications of pore blocking effects due to pore-pore interactions (Garcia-Martinez et al. 2014). The test of the congruency property predicted from ID-model is also a good way to evaluate deviations from the independent pore assumption (no pore-pore interaction) (Grosman and Ortega 2005; Coasne et al. 2005).

The main purpose of this chapter was to observe the geometric properties of hysteresis curves exhibited by the primary and higher order scanning curves through dynamic sorption experiments. The focus was on the slopes of primary scanning curves and testing of the congruency and wiping-out properties in sub-loops (refer to A.1 for a brief explanation of these two properties). Additionally, material characterization data including the cell wall density, porosity, pore size distribution (*PSD*), chemical composition and crystallinity were collected for further modeling and cell wall pore structure elucidation purposes (chapter 5 and 7).

3.2 Methodology

3.2.1 Sample preparation

A one-meter-long fresh log of 66-year old Douglas-fir (*Pseudotsuga menziesii*), and 78-year old western red cedar (*Thuja plicata*) (Figs. 3.1a and 3.1b) were cut from trees growing at the UBC Malcolm Knapp Faculty of Forestry Research Forest (Maple Ridge, BC). An 85-year old trembling aspen (*Populus tremuloides*) log (Fig. 3.1c) was cut from a tree growing at UBC Alex Fraser Faculty of Forestry Research Forest (Williams Lake, BC). Since the mature heartwoods dominate the cut wood disks, they were the interest of this study. Wood strips ($7 \times 70 \times 150\text{mm}^3$: tangential, radical, and longitudinal, Fig. 3.2a) were cut with a band-saw from annual rings 41–43, 40–45 and 24–29 from Douglas-fir (D-fir), western red cedar (WRC) and aspen, respectively. Those wood strips were then conditioned in climate chambers (Parameter Generation & Control, US) at 45°C and 60%H for several days, reaching an M_{emc} of 10% to 12%. They were then stored in sealed plastic bags under room temperature before use. The unused green wood was stored in a cold room set at 5°C.

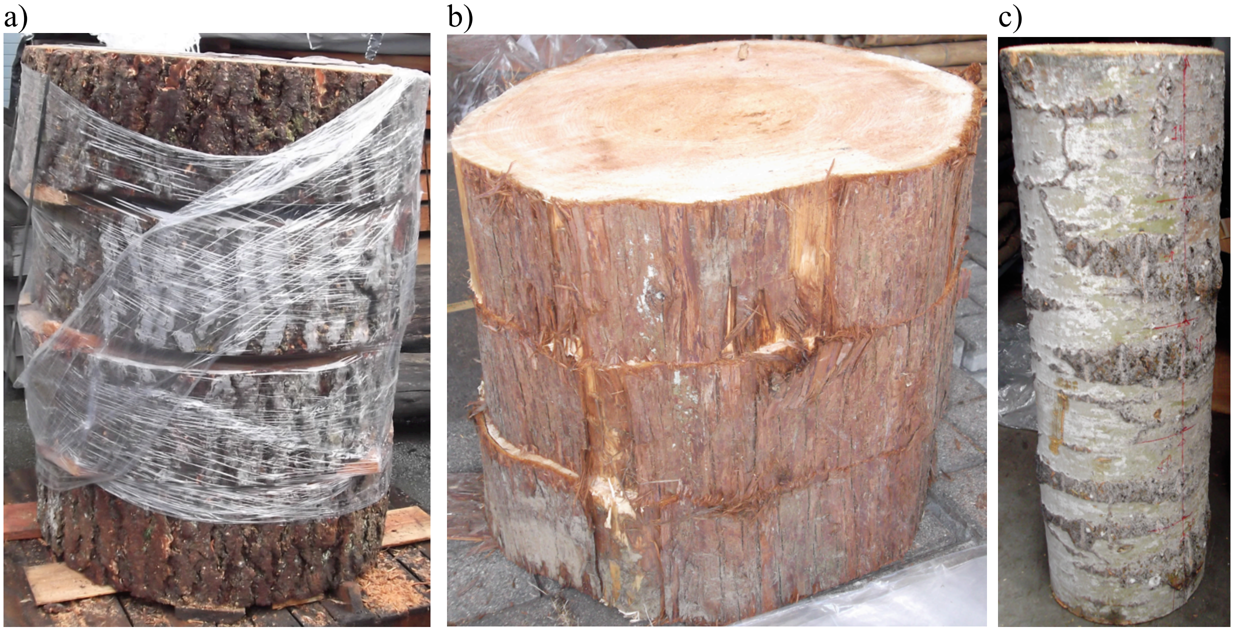

Figure 3.1: three species in this study. a) D-fir; b) WRC; c) aspen.

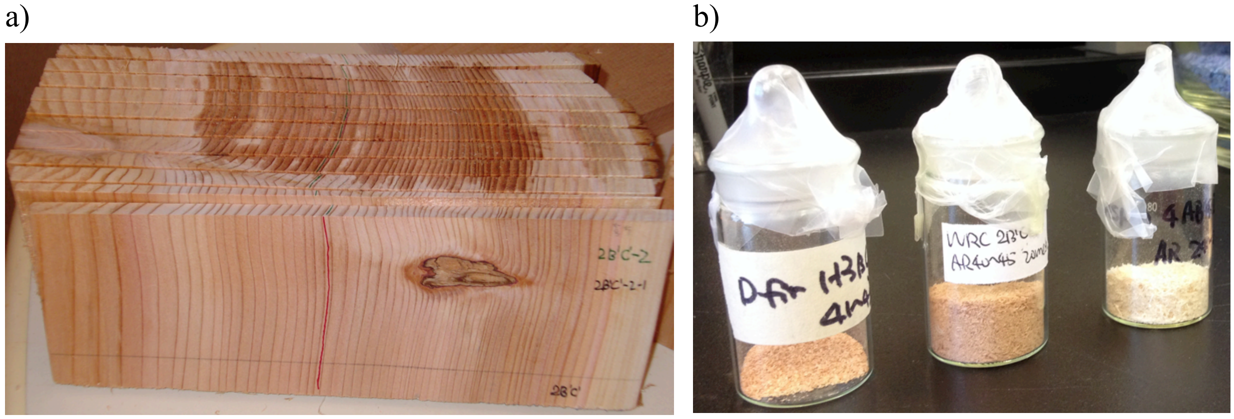

Figure 3.2: a) wood strips with red lines indicating selected annual ring regions; b) wood powder samples.

The conditioned wood strips were randomly chosen to be converted into wood powder. First, they were cut into small sticks (2 × 2 × $10mm^3$) with a small band saw and a knife. Then, the grinding was performed in a Wiley Mill and the material was sieved through 20-mesh or 40-mesh sieves. Therefore, the produced wood powder (Fig. 3.2b) was homogenous mixtures of earlywood and latewood from mature heartwood regions. Sorption specimens made of wood powder samples were randomly taken from this population.

In case of powdered samples, there might be some concern that the observed hysteresis patterns might not hold in the case of larger solid wood samples. Therefore, preliminary tests were also conducted with solid wood samples (2 × 2 × $5mm^3$) for some high-order scanning curves, and no pronounced differences were found between the behavior of solid and powder samples. Certainly, the milling process will cause some destruction of cell walls, but it seems that that does not have a detrimental effect on the overall sorption behavior patterns.

3.2.2 Observation of hysteresis patterns

The geometric characteristics of the 1st to the 4th order scanning curves were observed, and the congruency and wiping-out properties were examined. This approach is different from observations in literature where mostly input data were collected for modeling. Moreover, the framework of this observation is based on seven theories predicted from IDM (Everett and Smith 1954). Here, the hysteresis loops were defined based on the special geometric properties as hysteresis patterns. Patterns (a) and (b) are a family of ascending and descending curves as described in the literature (Peralta 1995a; Carmeliet 2005). Figs. 3.3a and 3.3b present an example of primary scanning curves with focus on slopes of these curves (indicated by color lines). Observation of patterns (c – e) were inspired by the theoretical loops enunciated by Everett and Smith (Fig. 6(a – c) in Everett and Smith 1954). Fig. 3.3c and 3.3e demonstrate ideal

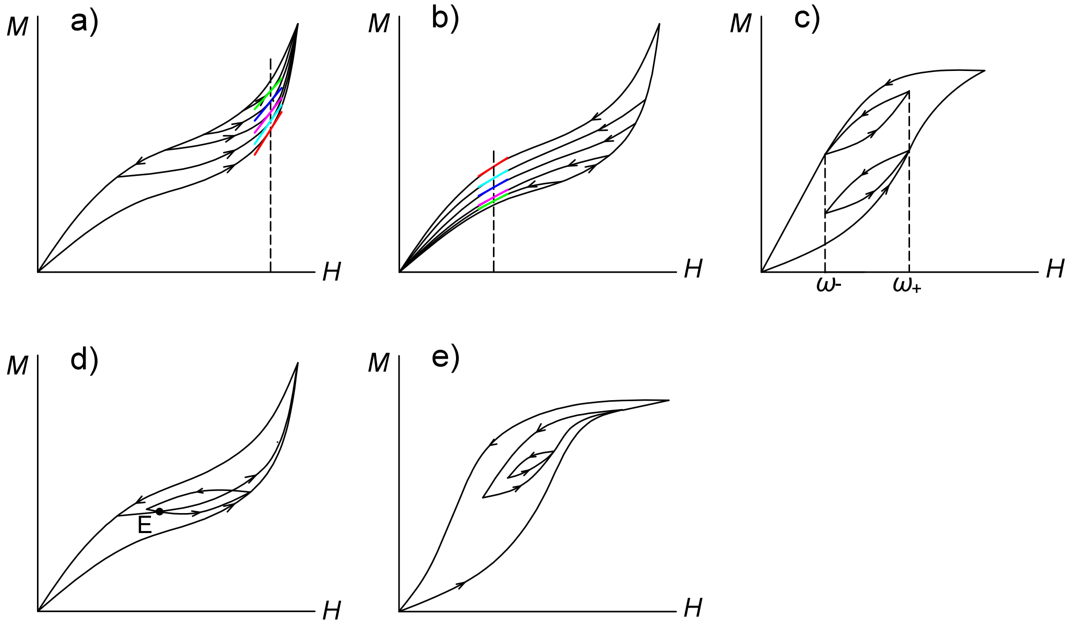

Figure 3.3: illustrations of five hysteresis patterns. a – e: patterns (a – e), modified from Everett and Smith (1954).

patterns conforming to the congruency and wiping-out properties, and Fig. 3.3d demonstrate that any point (E here) within the boundary loop can be reached by more than one way.

The investigations of scanning curves obtained by traditional methods ─ such as saturated salt solutions, climate chambers, and self-made vacuum systems ─ have some deficiencies. One is the accuracy of M_{emc} affected by the uncertainty in weight measurements; another is the long measurement time. The invention of an electronic sorption system based on ultrasensitive microbalances and fully automatic scheduled H cycles are more rapid and reliable. The instrument used here was the Dynamic Vapor Sorption device (DVS-1000, Fig. 3.4, Surface Measurement Systems, North America).

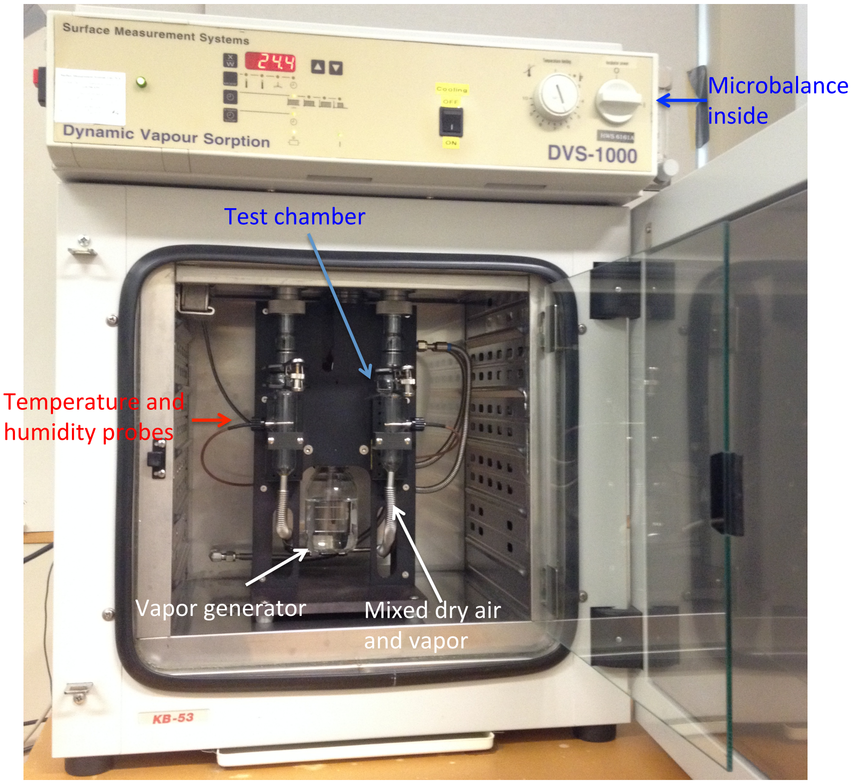

Figure 3.4: The dynamic sorption device: DVS-1000 showing key components.

The humidity of the test chamber was controlled by adjusting the ratio of mixed dry air and vapor with an accuracy of $H \pm 1\%$. The temperature of the chamber was controlled by a combined heating and cooling system with an accuracy of $\tau \pm 0.1^{o}$C. The microbalance inside the device has an accuracy of a part in 10 million gram. Its readings were collected by the computer according to the set intervals from 1s to 1min. The scheduled H cycles could be run by the computer automatically. After each run, the H returned to 0% by default.

In this study, the cycles were set within the 0 to 95%H range in 5% to 15% increments. A series of cycles in ascending and descending order were carried out mostly between 35% and 75% H. All these cycles were completed at 25^{o}C and then at 40^{o}C with a 0.002% mass change rate (*dm/dt*) over 5 min criterion until M_{emc}. The equilibrium criterion is set based on microbalance accuracy and the achievement of constant mass at a specified H.

Fig. 3.5 shows an example concerning the experimental concept. First, H was set to zero until the sample was completely dry ($M = 0$). Then, H was increased monotonically until it

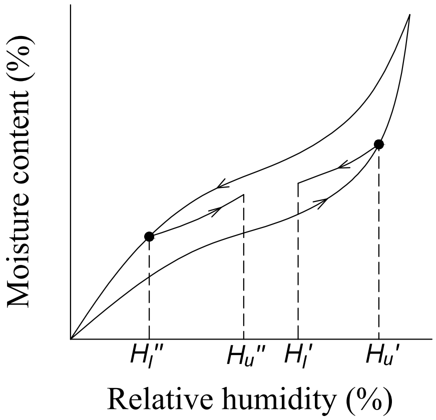

Figure 3.5: Schematic plot of a primary ascending curve and a primary descending curve with corresponding reversible points.

reaches some value H'_u and then H was gradually decreased monotonically to a series values $\{H'_l\}$. In this way, a boundary ascending curve was produced followed by a primary descending curve. By changing the values of H'_u, the family of primary descending curves were obtained. The specific set of H'_u in this study was $\{25, 35, 45, 55, 65, 75, 85\%\}$. $\{H'_l\}$ was set from corresponding H'_u to 0 with 10% H decrease.

The detailed settings of the H cycles are summarized in Table 3.1. There are two reasons that large H intervals were applied. One was that the observations in this work were of the qualitative nature, e.g. close data points sets were not necessary to observe a trend. The other was that large H interval settings reduce time requirements. The small H intervals used in pattern (b) came from further modeling requirements in chapter 4.

Table 3.1: Relative humidity settings for the five hysteresis patterns.

Patterns	H settings (%)																	
a	0	15	35	55	75	95	85	75	85	95	75	55	75	95	75	55	35	55
	75	95	75	55	35	15	35	55	75	95	75	55	35	15	0			
b	0	5	15	25	15	5	0	5	15	25	35	25	15	5	0	5	15	25
	35	45	35	25	15	5	0	5	15	25	35	45	55	45	35	25	15	5
	0	5	15	25	35	45	55	65	55	45	35	25	15	5	0	5	15	25
	35	45	55	65	75	65	55	45	35	25	15	5	0	5	15	25	35	45
	55	65	75	85	75	65	55	45	35	25	15	5	0					
c	0	35	55	75	55	35	55	75	95	75	55	35	55	75	55	35	0	
d	0	35	55	75	55	35	55	75	95	75	55	35	15	35	55	75	95	55
	15	0																
e	0	35	45	55	65	75	65	55	45	35	45	55	65	55	45	55	65	75
	95	75	55	35	0													

Three replicates were randomly selected from the original wood powder material. Each one was between 12 and 16 mg.

3.2.3 Dried cell wall density and porosity measurements

Density of dry cell walls (ρ_{cw}) and wood substance (ρ_{ws}) was determined using the classical pycnometric method (Stamm 1964). The method uses a liquid to replace volume of the tested material. By determining volume change of the replacing liquid, volume of the material can be obtained. Combined with measured mass of the material, its density can be computed. Since the non-polar liquid (white minimal oil here) cannot penetrate the cell wall pores, the volume of cell walls can be determined by exchanged volume of the non-polar liquid. Likewise, the volume of wood substance can be determined from the penetrating polar liquid (water here). The pycnometers and vacuum desiccator used in this study are shown in Fig. 3.6.

Figure 3.6: Pycnometers and vacuum desiccator used in this study.

The 40-mesh wood powder sample (4 replicates) was used for this measurement. All procedures were conducted within an air-conditioned lab environment (21 – 23°C). Dry, pre-weighed 25ml pycnometers (w_0) were filled with 2.5 – 3.0g samples and then dried to constant weight (w_1) at 103°C. The pycnometers were then filled with distilled water or white mineral oil (Sigma-Aldrich, Canada) to a level at least fully covering the sample. Then, they were placed in vacuum desiccators until all the bubbles in the sample were removed, which usually took 4 to 6 hours. After releasing the vacuum, distilled water or mineral oil was added to the pycnometers such that the pycnometers as well as capillary holes in the stoppers were filled with the displacing liquids. Any excess liquid leaked from the stopper were dried using Kimwipes* Wipers and final weight was recorded (w_2 for water as displacing liquid, w_3 for mineral oil).

The accurate volume of each pycnometer (V_0) was obtained by fully filling the pycnometers with distilled water and the weight was recorded as w_4. The density of mineral oil (ρ_{oil}) at the operating temperature was determined by fully filling the pycnometers with mineral oil and the weight was recorded as w_5. V_0 , ρ_{oil} , ρ_{cw} and ρ_{ws} were calculated as:

$$V_0 = \frac{w_4 - w_0}{\rho_w} \tag{3.1}$$

where ρ_w is water density, equal to 0.9977735 g/cc at 22 °C (Harris, 2003).

$$\rho_{oil} = \frac{w_5 - w_0}{V_0} \tag{3.2}$$

$$\rho_{cw} = \frac{w_1 - w_0}{V_0 - \frac{w_3 - w_1}{\rho_{oil}}} \tag{3.3}$$

$$Apparent \ \ \rho_{ws} = \frac{w_1 - w_0}{V_0 - \frac{w_2 - w_1}{\rho_w}} \tag{3.4}$$

Since the density of bound water is larger than that of free water, the actual volume of replaced water should be larger. 0.0052 cc/g is usually used to correct this extra volume of replaced water (Skaar 1972). Let v_{ws} and v_{cw} be the specific volume of cell wall substance and cell wall respectively, then

$$corrected\ v_{ws} = apparent\ v_{ws} + 0.0052\ cc/g \tag{3.5}$$

$$corrected\ \ \rho_{ws} = \frac{1}{v_{ws}} \tag{3.6}$$

Finally, the total cell wall pore volume (δ) and cell wall porosity (ϕ) is calculated as:

$$\delta = v_{cw} - v_{ws} \tag{3.7}$$

$$\phi = \frac{v_{cw} - v_{ws}}{v_{cw}} \times 100\% \tag{3.8}$$

3.2.4 Characterization of nanopores in dried cell walls

Mesopore and micropore size distributions in dried cell walls were analyzed from N_2 sorption isotherms at -196°C and CO_2 sorption isotherms at 0°C respectively using an automatic gas adsorption device, AUTOSORB-1 (Quantachrome, USA) (Fig. 3.7).

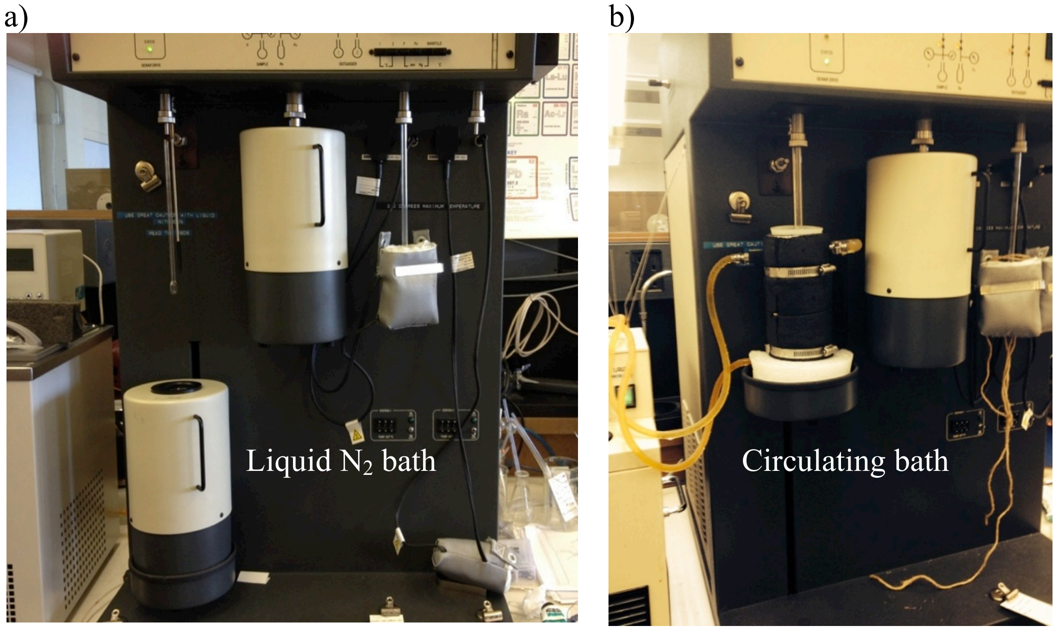

Figure 3.7: AUTOSORB-1 instrument. a) standard N_2 test set up; b) developed CO_2 test setup.

The 20-mesh wood powder sample (3 replicates) was added to 9mm (stem diameter) large bulb sample cell (3/4 and 2/3 volume percentages for mesopore and micropore tests, respectively) and outgassed for 8 hours or more at 60°C until passing a 20 microns/min leak test at room temperature. Depending on the species, dried sample mass was in the range of 0.7 – 2g. The N_2 test temperature (-196°C) was well controlled by the liquid N_2 bath under 1atm (Fig. 3.7a). The CO_2 test temperature (0.3 ± 0.5°C) was controlled by a circulating bath (Lauder WKL 230) (Fig. 3.7b). To prevent freezing in the circulation bath, 50% (volume percentage) ethylene glycol solution was added. For the N_2 tests, 79 equal-distance points in the range of 0.025–0.995 relative pressure were chosen to obtain the full adsorption and desorption isotherms. For the CO_2 tests, 56 points in the range of 0.0001–0.029 relative pressure (more intensive points in the lower range 0.0001–0.01) were chosen to obtain part of the adsorption and desorption isotherms. The adsorption time was set at 5 minutes chosen for both tests. Density function theory (DFT) included in the AUTOSORB-1 software was used to analyze the total pore volume and pore size distribution for both mesopores and micropores.

3.2.5 Characterization of nanopores in fully saturated cell walls

The solute exclusion method developed by Stone and Scallan (1968) was used to analyze the pore size distributions of fully saturated cell walls. Dextrans and polyethylene glycols (PEG), are often chosen as probe molecules due to their good water solubility, inert interaction with cell wall materials both chemically and physically, and fairly narrow range of molecular weight fraction (Stone and Scallan 1968, Van Dyke 1972, Lin et al. 1987, Wang et al. 2011). Glucose, Maltose, Detran T40 and five PEG series, whose molecular weights and corresponding solute diameters are summarized in Table 3.2, were used in this study.

Table 3.2: Molecular weight and solution diameters of sugars and PEG.

Solutes	Molecular Weight	Solute Diameter (nm)	Manufacturer
Glucose	180	0.8	Sigma
Maltose	342	1.0	Sigma–Aldrich
PEG 400	380-420	1.8	Sigma
PEG 600	570-630	2.1	Sigma

Solutes	Molecular Weight	Solute Diameter (nm)	Manufacturer
PEG 1000	950-1050	2.7	Sigma
PEG 1500	1400-1600	3.3	Sigma
PEG 8000	7000-9000	8.4	Sigma
Dextran T40	35000-45000	9.0	Pharmacia

Note: Solute diameters of sugars are from Stone and Scallan (1968), and solute diameters of PEG series are from Van Dyke (1972).

40-mesh wood powder samples (5 replicates) were firstly thoroughly washed with distilled water until free of all water-soluble materials, which could be examined from the refractive index of washed water. This washing step was very important since a small concentration difference could lead to a very large relative error in the pore volume calculation (Van Dyke 1972). Then,

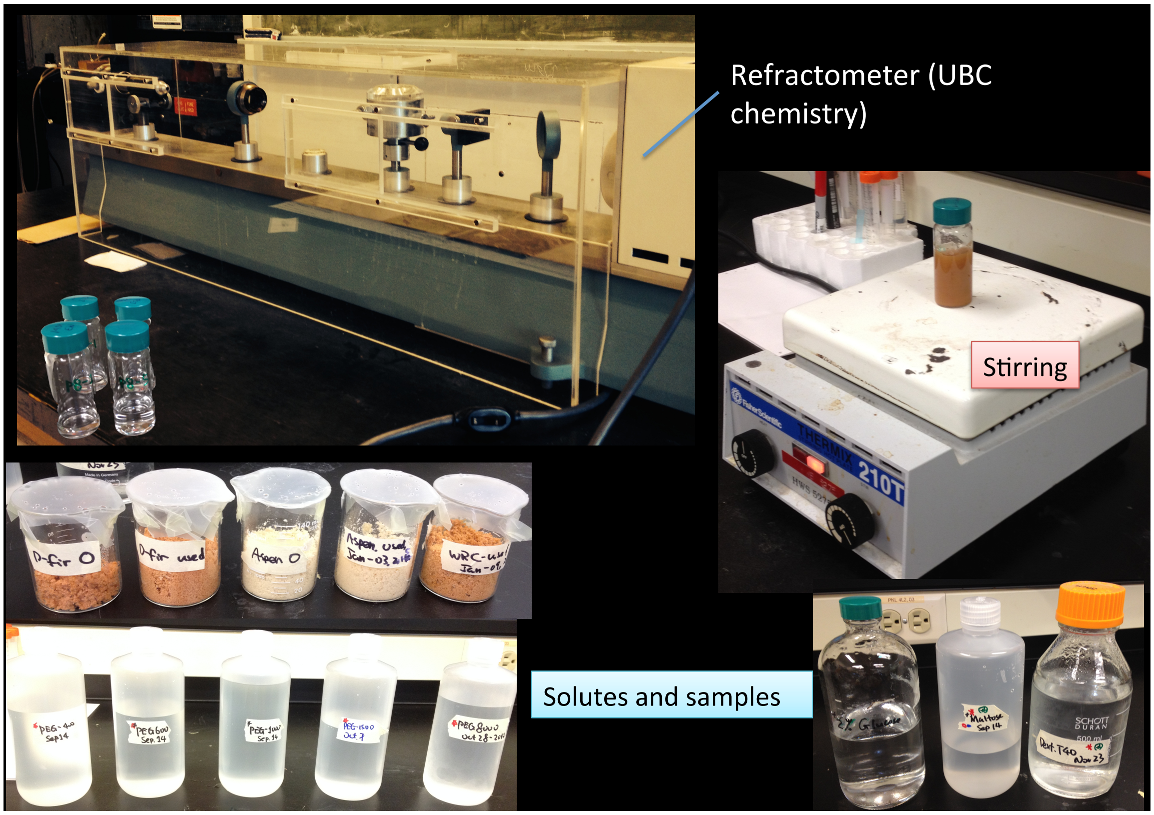

Figure 3.8: Solute exclusion test related samples, solutes and instrument.

residual water in the sample was drained off under mild vacuum to achieve 250%–300% *M* (Fig. 3.8). 2.5 – 3g wet material was accurately weighted into a 30ml glass bottle with a completely water proof screw cap. About 12ml of 2% stock solution of a solute was then added and the bottle reweighted. The bottles were allowed to stand for two days with periodic (4-hour) magnetic stirring (Fig. 3.8).

After this time, about 6ml aqueous phase was decanted into centrifuge tubes. The centrifuge was set at 10000 rpm for 10 minutes. The supernatants were then filtered through 0.2µm syringe filters. The concentrations of the initial and final probe solutions were determined by a differential refractometer (Fig. 3.8), which was calibrated by a series of standard solutions with concentrations from 1.4% to 2.4% for each solute. There were two ways to obtain the dried mass of the sample. One was to wash the sample free of solutes, filtered and dried at 103°C. The other was to take one sample directly for *M* measurement by oven-dried method every 3 or 4 samples, and use it as an average *M*. These two approaches were compared, and it was concluded that if the wet samples were thoroughly mixed before the test, the later method was reliable. Thus, the later method, which saves a large amount of time and effort, was adopted. The inaccessible water w_{iw} (g/g dry wood) is given by:

$$w_{iw} = \frac{w_s + w_q}{w_p} - \frac{w_q}{w_p}\frac{c_i}{c_f} \tag{3.9}$$

where $w_p$is dried mass of sample (g); w_q is mass of water in sample (g); w_s is mass of added probe solution (g); $c_i$is initial concentration of the probe solution (g/g solution); c_f is final concentration of probe solution (g/g solution).

The cumulative pore volume at each probe solutes size is the same as the volume of inaccessible water. Assuming the density of inaccessible water is 1.0 g/cc, the cumulative pore volume is w_{iw} cc/g dry wood.

3.2.6 Crystallinity measurements

Crystallinity of cell walls was determined using a Brucker D8 Discover X-Ray diffraction unit (Fig. 3.9a). The X-Ray diffraction method is based on analysis of the specific diffraction patterns (Fig. 3.9b) caused by the crystalline region of the cell wall.

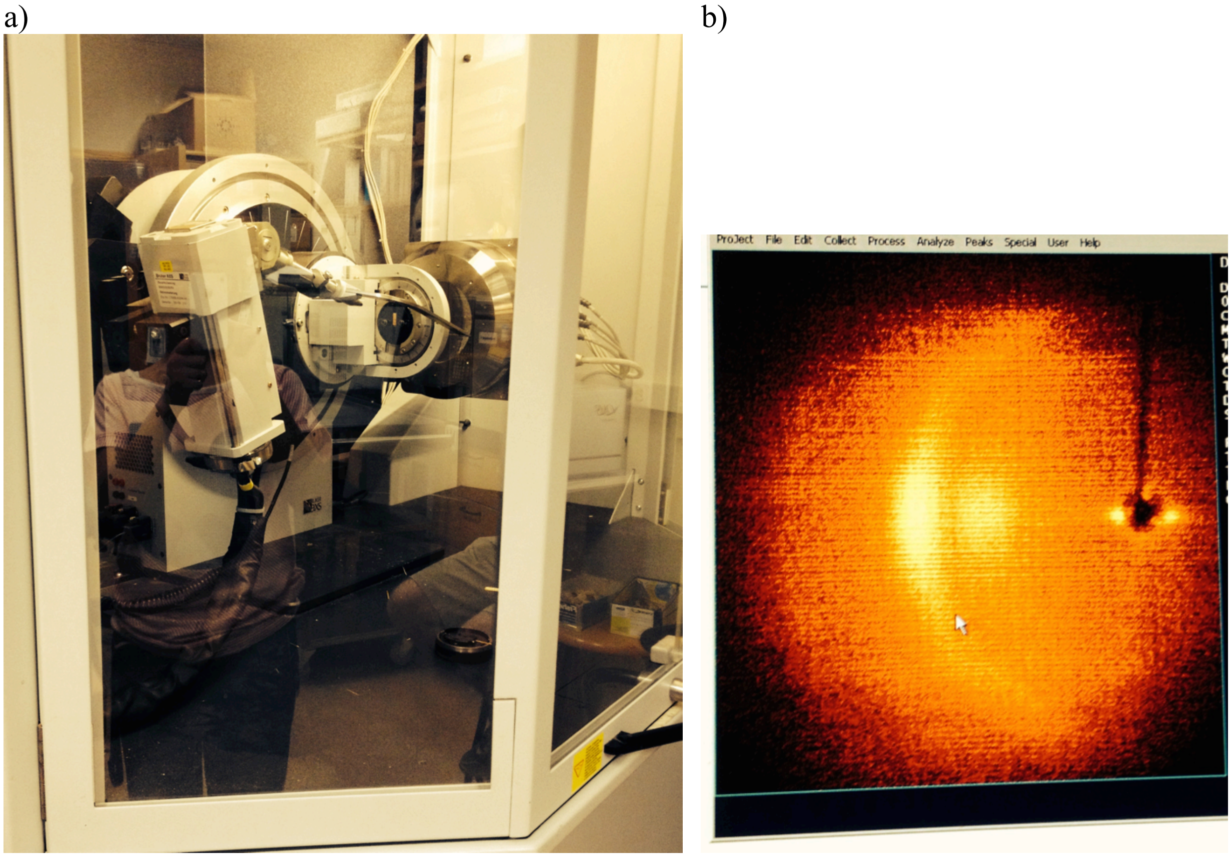

Figure 3.9: a) the Brucker D8 Discover X-Ray diffraction unit; b) a typical diffraction pattern.

The 1.68mm (tangential direction) thin slides (5 replicates) were produced from the dried wood strips using a twin–blade pneumatic saw. The setup of the instrument followed that in Rayirath et al. (2008). The 002-diffraction arc T-values were collected on the radial face of both earlywood and latewood portions for each sample. Wide-angel diffraction was used in the transmission mode, and CuKα1 radiation ($\lambda = 1.54$Å) was used. The X-ray source was set to $2\theta = 17.5°$ and the detector was set to $\theta = 0°$. The crystallinity was then calculated by fitting collected data using the method described in Vonk (1973).

3.2.7 Chemical composition measurements

The carbohydrate composition, and acid-insoluble lignin, was determined according to the Klason protocol described in TAPPI Method T 249 cm-09 and T 222 om-11. The acid-soluble lignin was measured according to TAPPI Useful Method UM250, 1991. The 40-mesh wood powder samples (3 replicates) were firstly extracted overnight with acetone at 70°C with a Soxhlet apparatus. The sulfuric acid was then added to the oven dried samples to hydrolyze the cellulose and hemicellulose to monosaccharide constitutes, the quantity of which was determined using high-performance liquid chromatograph (HPLC) system. The acid insoluble lignin was filtered with medium coarse sintered-glass filter and quantified gravimetrically; the acid soluble lignin was determined by measuring absorbance at 205nm. The extractive contents were determined gravimetrically by accurately weighting 1.0 – 1.5g samples (two replicates) before and after extraction.

3.3 Results and Discussion

3.3.1 Hysteresis patterns

3.3.1.1 Five patterns for D-fir at 25°C

Fig. 3.10 shows representative plots of observed hysteresis patterns (a – e) for a D-fir sample at 25^{o}C. The reproducibility of these patterns is confirmed by the other two samples.

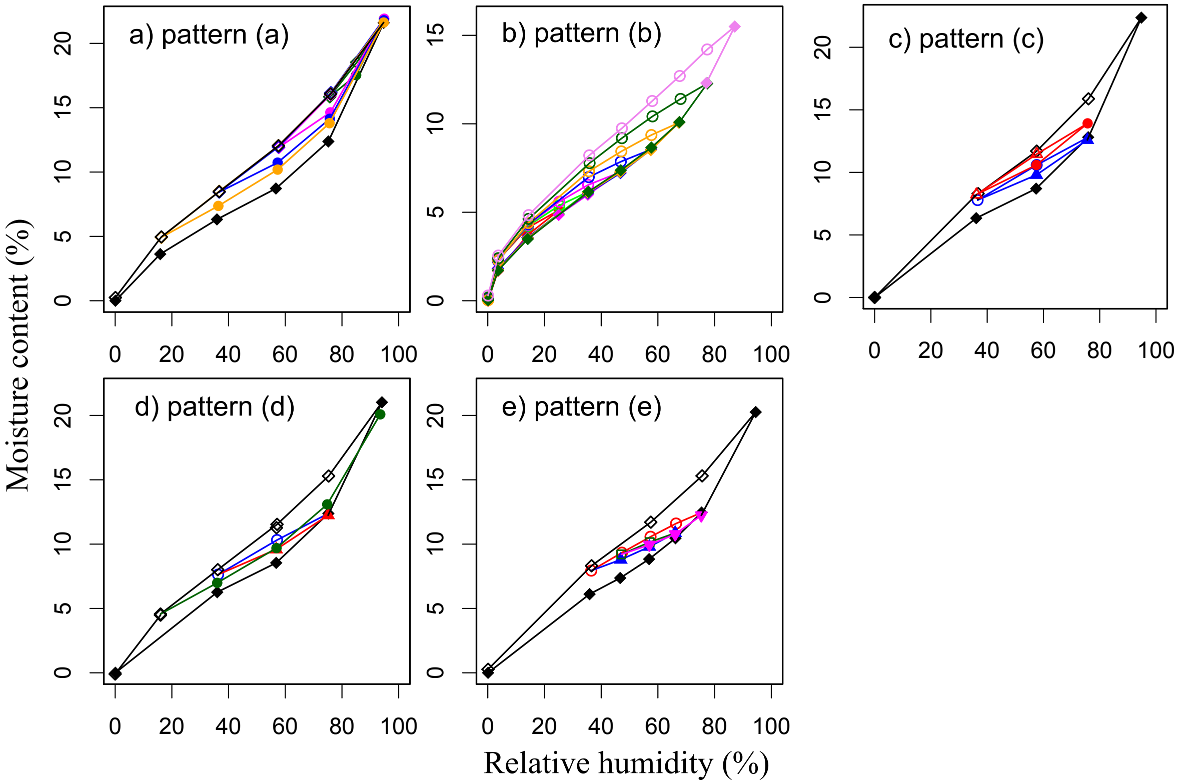

Figure 3.10: Hysteresis patterns for D-fir at 25°C. Solid symbols represent adsorption process and open symbols represent desorption. Symbol diamond indicates the boundary curve points, and symbols circle, triangle, square, and inverted triangle indicate the primary to 4th scanning curve points.

Pattern (a) in Fig. 3.10a demonstrates that the primary ascending curves are not intersecting with each other below the highest *H* considered (around 95%). At the highest *H*, the points are not matched perfectly. This is caused by the difficulty of controlling the high *H* accurately and reaching an equilibrium. Furthermore, limited by instrumentation, a 100%H cannot be set. However, the trend in pattern (a) strongly indicates that these primary ascending curves will eventually merge at M_{fsp}.

Similarly, pattern (b) in Fig. 3.10b clearly demonstrates that primary descending curves are not intersecting with each other and show a tendency to merge at the origin. Because the absolute dry state is better defined than M_{fsp}, this test result appears more convincing than the previous one from the primary ascending curves.

The crossover of primary descending curves with the boundary descending one was reported by Peralta (1995a) for yellow poplar (*Liriodendron tulipifera* L.). Initially, this crossover property was considered as species related, however, after examining pattern (b) of the other two species, the probability is high that the reported crossover was caused by the relative large experimental errors in salt-solution-based self-designed vacuum systems. For materials with narrow pore size distributions, the crossover is usually indicative for pore independence (Everett and Smith 1954; Grosman and Ortega 2005). As the cell walls have wide pore size distributions, the crossover cannot be simply evaluated in terms of pore connectivity. However, it is visible from pattern (b), that all primary descending curves change gradually with H, showing no sign of the characteristic cavitation step (curves with very steep slope) at any point, i.e. the absence or the presence of weak pore blocking effect can be deduced (Garcia-Martinez et al. 2014).

Pattern (c) in Fig. 3.10c presents two sub-loops between the same two consecutive extrema. Qualitatively, these two loops have similar shape and size, but because of small uncertainty in controlling H, the two consecutive extrema are not the same. For example, in Fig. 3.10c, the extrema of the upper and lower loops are {36.6%, 75.5%, 36.5%} and {76%, 36.3%, 75.5%}, respectively. The range for the left extremum is 36.5% - 36.6%, and 75.5% - 76% for the right one. Therefore, it cannot be expected that the observed two loops have the exact same shape and area. To compare the two sub-loops more closely, the left end points are offset to overlap as shown in Fig. 3.11a.

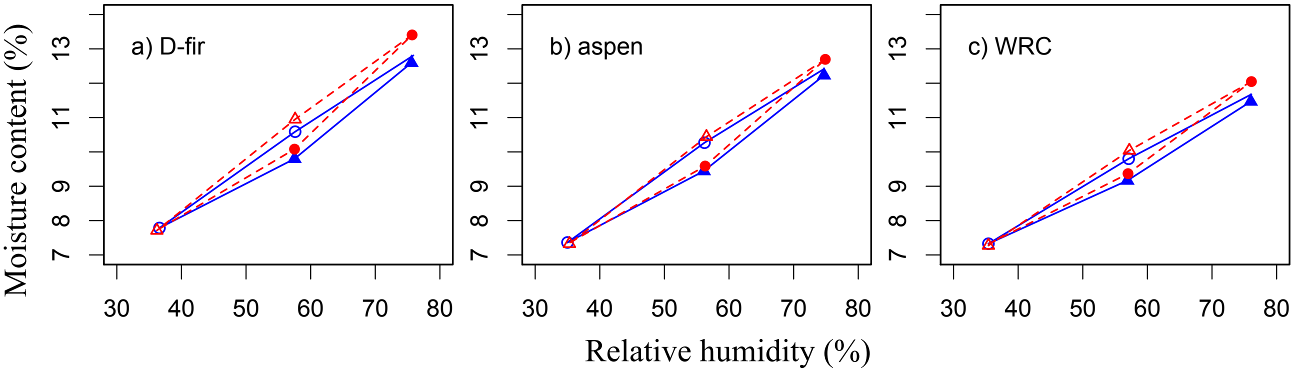

Figure 3.11: Comparison of two sub-loops in pattern (c) for the three species at 25°C. The left endpoint of each sub-loop is offset to overlap. The loops are nearly congruent. Solid symbols represent adsorption process and open symbols represent desorption. Symbols circle and triangle indicate the primary and 2nd scanning curve points.

According to Mayergoyz 1991, these two loops are congruent if they coincide after the offset. The extent of congruency for the three species is different (Fig. 3.11a – c), so to evaluate the extent of congruency, the area of the two loops were compared quantitatively. Firstly, the data points were interpolated by the cubic spline method and then the integration was performed over the two consecutive extrema based on the trapezoidal rule. Table 3.3 summarizes the results from the three species.

Table 3.3: Summary of loop area differences in hysteresis pattern (c) for three wood species at 25°C with three replicates each.

Species	Average. Δarea (%)
D-fir	6.63%
Aspen	1.10%
WRC	3.82%

The average relative loop area difference of D-fir is much larger than that of other two species, but still less than 10%. The congruency property satisfaction has been used to evaluate the validity of assumptions in IDM, which reflects indirectly the presence of independent pores (Lilly and Hallock 2001; Coasne et al. 2005). Compared to the reported experimental sub-loops of other porous materials according to Wootters and Hallock (2000), Lilly and Hallock (2001), and Grosman and Ortega (2005), the congruency observed in the present study was very high, and thus the theory of independent cell wall pores is supported.

The intersection points in pattern (d) as in Fig. 3.10d shows that these points can be reached more than one way, namely, some from lower and some from higher *H*. There is no restriction on the intersection points, and thus this property can be further generalized, i.e. any point within the hysteresis loop can be reached in many ways. This is consistent with the known fact that the future *M* of wood depends on its hygroscopic history. However, it is also known that once wood is fully dried or fully saturated, the influence of the previous “history” disappears, i.e. the “history influence” is connected to certain conditions. The following discussion of pattern (e) is dedicated to this point.

Pattern (e) in Fig. 3.10e illustrates the behavior of high-order scanning curves under a series of cycles of *Hs* with decreasing amplitudes. To observe this pattern more clearly, the central sub-loops were plotted with the expanded scale in Fig. 3.12.

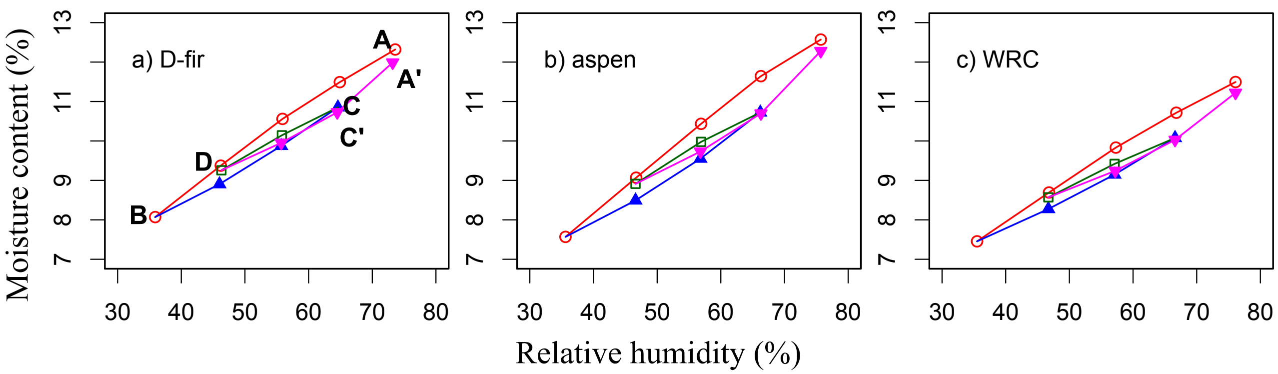

Figure 3.12: Pattern (e) for three wood species at 25°C. The sub-loops show wiping-out property. Solid symbols represent adsorption process and open symbols represent desorption. Symbols circle, triangle, square, and inverted triangle indicate the primary to 4th scanning curve points.

Let A to D be the reversal points of the primary to the 4th scanning curves (Fig. 3.12a). Starting from point D, the 4th ascending curve moves towards C and A with a slight deviation. The actual returning points are denoted as C' and A'. Then the differences can be compared from the pairs {C, C'} and {A, A'} (Fig. 3.12a). However, considering experimental errors, theoretically C and C' can be coincident, and the same for A and A'. This is a sign of the wiping-out property. Assuming the coincidences, the 4th ascending curve returns to the track of the 2nd ascending curve (BCA) after passing point C as if the smaller sub-loop CD would not exist. Then, the curve returns to the boundary ascending curve after passing point A as if the bigger sub-loop AB would not exist. In this way, the history of loops CD and AB is wiped out. As summarized by Mayergoyz (1991), the larger sub-loops can wipe out the history of the smaller ones.

3.3.1.2 Effect of species

Overall, a consistent five patterns were observed for the three species at 25°C. Figs. 3.11 and 3.12 show that congruency and wiping-out properties hold for all species, but with different degrees of satisfaction. In Fig. 3.13a, pattern (b) for the three species are overlapped for a closer comparison.

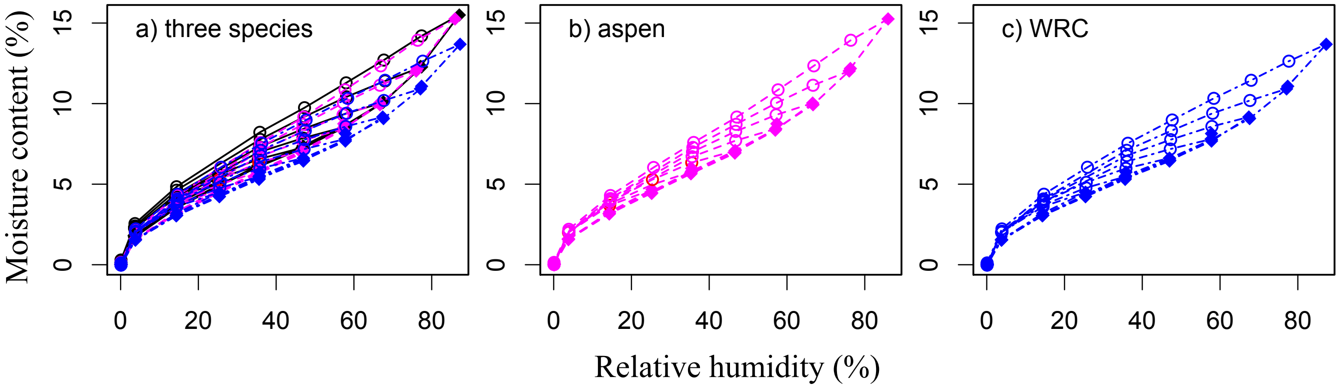

Figure 3.13: Hysteresis pattern (b) for three wood species at 25°C. Solid symbols represent adsorption process and open symbols represent desorption. Symbol diamond indicates the boundary curve points, and symbol circle indicates the primary scanning curves.

Slight differences of sorption behavior are probably due to the differences in chemical, physical, mechanical and anatomical properties of these the woods (Mullins and McKnight 2000). However, the trend of the primary curves (non-intersecting) remains the same (Figs. 3.13b and 3.13c), indicating a consistent pattern (b) among the species. This consistency might be related to some common species characteristics, i.e. cell wall density and porosity, which has been reported to be fairly universal for most wood species (Kellogg and Wangaard 1969; Stamm 1964).

3.3.1.3 Effect of temperature

Fig. 3.14 shows the central part of the pattern (e) of the three species at 25 and 40°C. The sub-loops become narrower at the higher temperature, however, the wiping-out property is maintained well.

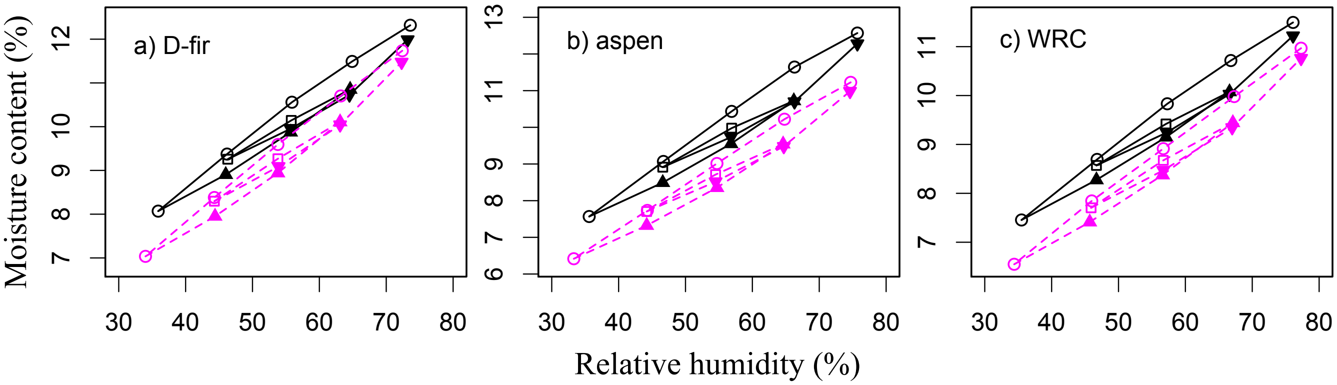

Figure 3.14: Comparison of hysteresis patterns (e) at 25 and 40°C. Solid lines represent scanning curves at 25°C and dashed lines for 40°C. Solid symbols represent adsorption process and open symbols represent desorption. Symbols circle, triangle, square, and inverted triangle indicate the primary to 4th scanning curve points.

By further examining the other four patterns, it can be concluded that these five patterns were observed at 25°C hold at 40°C. This temperature independence implies comparable hysteresis origins within the 25 to 40°C range.

3.3.1.4 Congruency and wiping-out properties

It is found that the extent of satisfaction of the wiping-out property is better than that of the congruency property (Fig. 3.14 vs. Fig. 3.12). This is consistent with the reported experimental scanning curves from other nanoporous systems (Lilly et al. 1993; Lilly and Hallock 2001). Furthermore, theoretical network models also demonstrated that the interaction of pores would affect the congruency, but not the wiping-out property (Enderby 1956; Rojas et al. 2001). Interestingly, Coasne et al. (2005) emphasized the importance of adsorbed films with smaller size pores (such as cell wall pores) in applying the ID-model principle. Based on their idea, the presence of a thin film before capillary condensation would cause deviation of the congruency property. Derome et al. (2008) took this into account in applying ID-model to wood, but later, this approach was not followed (Patera et al. 2016). The congruence observed in this study is interpreted as a suggestion that the role of the thin film hypothesis is less important than that of the capillary condensation. Furthermore, a thin film requires the existence of empty pores, and if this would dominate the cell wall pores, large empty cell wall pores would have been observed at various moisture contents. According to Skaar (1972), cell wall pores are empty of water at 0%M, but they begin to fill up as M increases, and they become fully saturated with water at M_{fsp}. This implies the thin film hypothesis is not valid, thus suggesting the dominance of capillary condensation during sorption.

3.3.2 Dried cell wall density and porosity

Table 3.4 presents the mean value and standard deviation of the cell wall substance specific volume, cell wall specific volume, and the calculated mean and 95% confidence interval of cell wall pore volume at the absolute dried state for D-fir, WRC and aspen. The cell wall density and porosity can be obtained according to Eqs. (3.6) and (3.8).

Table 3.4: Cell wall specific volume and pore volume of D-fir, aspen and WRC

Species	Cell wall substance specific volume (cc/g)			Cell wall specific volume (cc/g)			Cell wall pore volume (cc/g)	
	Sample size	Mean	Standard deviation	Sample size	mean	Standard deviation	mean	95% confidence interval
D-fir	7	0.654	0.003	4	0.687	0.001	0.033	(0.030, 0.036)
Aspen	4	0.662	0.002	4	0.6926	0.0006	0.031	(0.027, 0.034)
WRC	5	0.667	0.002	4	0.6992	0.0006	0.032	(0.030, 0.035)

3.3.3 Mesopores and micropores in dried cell walls

Fig. 3.15 shows N_2 sorption isotherms at -196°C and CO_2 sorption isotherms at 0.3°C of dried D-fir, aspen, and WRC samples. Since the saturated pressure of CO_2 at 0°C is 3.471MPa

(Quantachrome Instruments 2011) and the maximum pressure the instrument can achieve is around 1atm, the measured relative pressure on CO_2 isotherms is below 0.03.

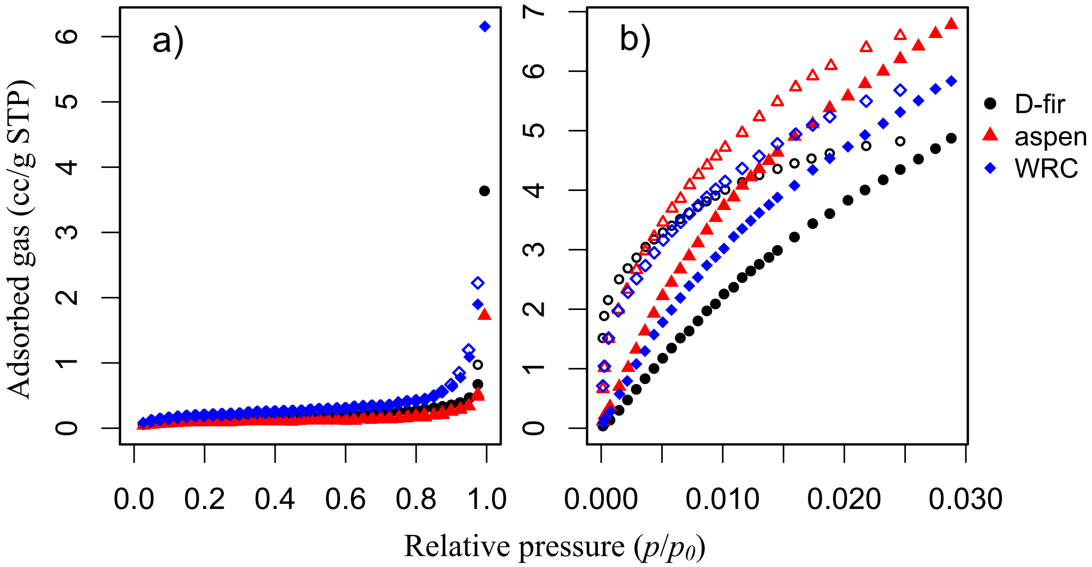

Figure 3.15: Gas sorption isotherms for D-Fir, aspen and WRC. a) N_2 sorption isotherms at -196°C; b) CO_2 sorption isotherms at 0.3°C. Solid symbols represent adsorption and open symbols represent desorption.

Hysteresis is found at the high relative pressure region of the N_2 sorption isotherms, and the entire investigated region on CO_2 sorption isotherms. The magnitude of hysteresis seems to depend on the species. This phenomenon is very interesting, but beyond the scope of the study. Fig. 3.16 presents the cumulative mesopore and micropore size distributions calculated from the N_2 and CO_2 sorption isotherms, respectively with density function theory (DFT) based on the carbon slit pore model. By default, the desorption branch on the N_2 isotherm and the adsorption branch on the CO_2 isotherm were selected for the above calculations in the AUTOSORB-1 software.

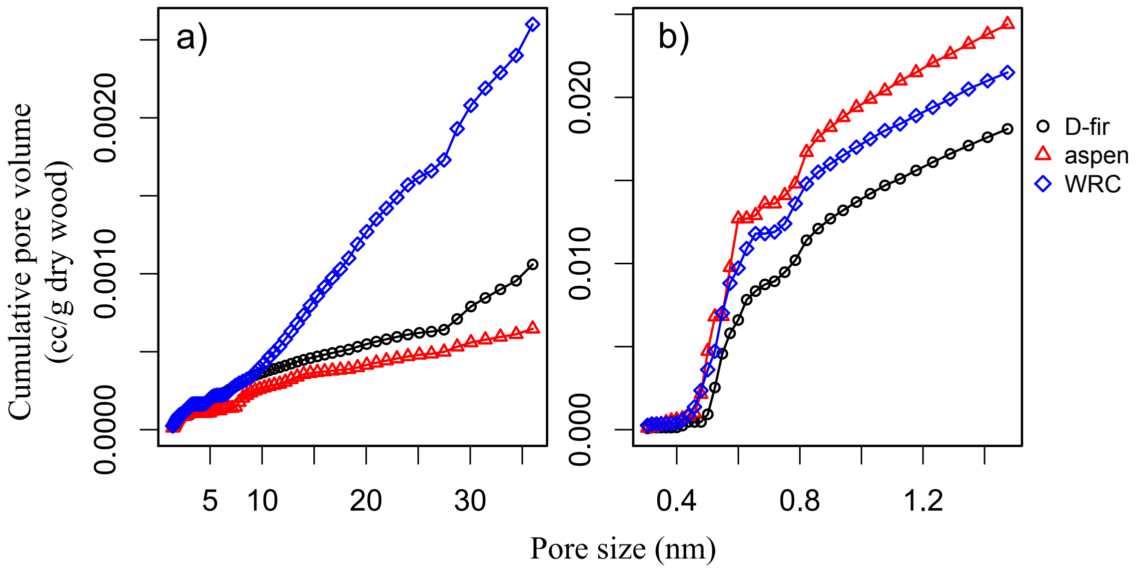

Figure 3.16: Cumulative pore volumes for D-fir, aspen and WRC.
a) mesopore; b) micropore.

3.3.4 Nanopores in fully saturated cell walls

Fig. 3.17 shows the calibration curve of the differential refractometer for the PEG-600 solute. For all solutes in Table 3.2, the correlation coefficient of calibration curve is above 0.99, demonstrating high accuracy of measured solute concentrations.

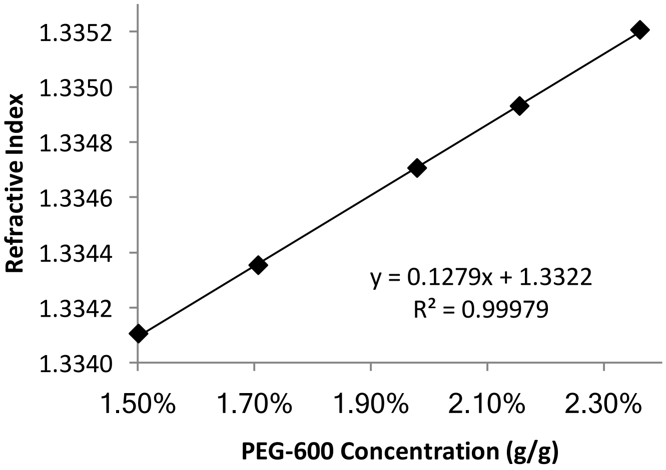

Figure 3.17: The calibration curve for PEG-600.

The mean value and standard deviation of the cumulative pore volume of the fully saturated cell wall at each solute size for D-fir, aspen and WRC are presented in Table 3.5. Large uncertainties are found for some measurements, e.g. the highlighted data in Table 3.5. Great caution is required to perform every step in the solute exclusion procedures as a small concentration difference of the solution will lead to a large deviation of the pore volume.

Table 3.5: Cumulative pore volume of fully saturated cell walls.

Solutes	Solute Size nm	Cumulative Pore Volume cc/g dry wood D-fir	aspen	WRC
Glucose	0.8	0.39 ± 0.04	0.35 ± 0.04	0.39 ± 0.03
Maltose	1.0	0.33 ± 0.02	0.44 ± 0.06	0.42 ± 0.06
PEG-400	1.8	0.39 ± 0.04	0.52 ± 0.06	0.40 ± 0.06
PEG-600	2.1	0.5 ± 0.1	0.66 ± 0.05	0.39 ± 0.02
PEG-1000	2.7	0.65 ± 0.04	0.82 ± 0.02	0.55 ± 0.02
PEG-1500	3.4	0.68 ± 0.04	0.75 ± 0.05	0.65 ± 0.08
PEG-8000	8.4	0.70 ± 0.02	0.86 ± 0.06	0.9 ± 0.2
Detran T40	9.0	0.74 ± 0.08	0.93 ± 0.06	0.84 ± 0.06

Figure 3.18 illustrates the shape of cumulative pore distributions based on data in Table 3.5. Overall the cumulative pore volume increases with the solute size, demonstrating a satisfactory trend.

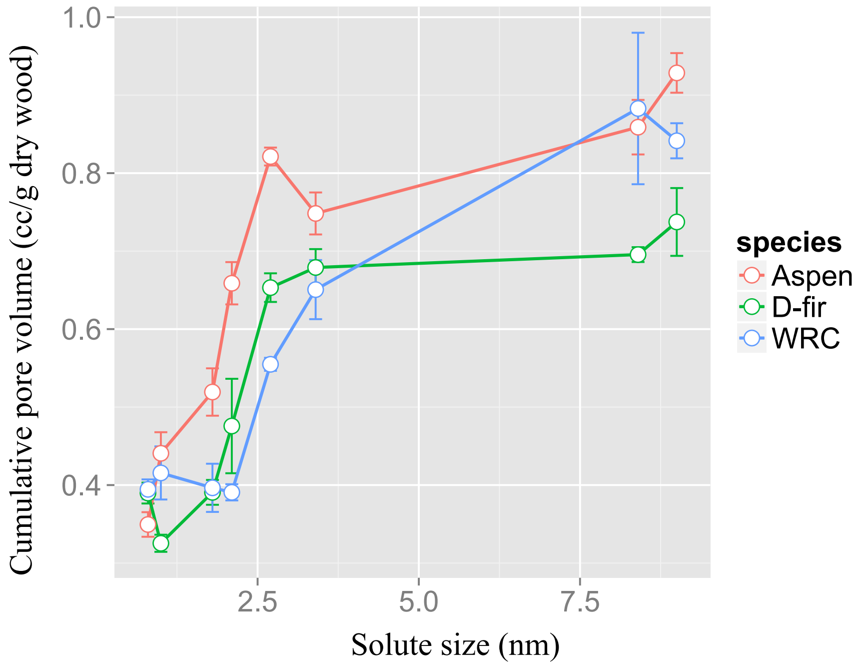

Figure 3.18: Cumulative pore volume curve for D-fir, WRC and aspen. Circles indicate mean values and bars indicate standard error.

3.3.5 Crystallinity

The mean value and standard deviation of cell wall crystallinity for the three species are given in Table 3.6.

Table 3.6: Cell wall crystallinity for D-fir, aspen and WRC.

Species	Crystallinity (%)
D-fir	50 ± 2
Aspen	41 ± 2
WRC	45 ± 2

3.3.6 Chemical composition

The mean value and standard deviation of the extractive, cellulose, hemicellulose and lignin contents for the three species are summarized in Table 3.7.

Table 3.7: Chemical composition for D-fir, WRC and aspen.

Species	Extractives (%)	Cellulose (%)	Hemicelluloses (%)	Soluble lignin (%)	Insoluble lignin (%)	Total lignin (%)
D-fir	4.2 ± 0.1	44.1 ± 0.5	21.5 ± 0.3	1.2 ± 0.2	26.7 ± 0.2	27.9 ± 0.3
Aspen	2.4 ± 0.1	51.0 ± 0.5	20.6 ± 0.2	7 ± 1	16.7 ± 0.6	24 ± 1
WRC	10.4 ± 0.1	44.2 ± 0.4	13.1 ± 0.3	1.5 ± 0.2	30.8 ± 0.3	32.2 ± 0.4

Note: the cellulose content is from the glucan; and hemicellulose content is from sum of arabina, glacta, xylan and mannan.

3.4 Conclusion

Five hysteresis patterns revealing important geometric properties of scanning curves ─ such as the slopes, the congruency, and wiping-out properties ─ were investigated by means of an automatic vapor sorption instrument on Douglas-fir, aspen and western red cedar at 25 and 40°C. It is found that the primary ascending and descending curves are not intersecting with each other and the curves tend to merge at the fiber saturation point and the origin, respectively. Furthermore, the sub-loops of all the species showed a good congruency and even better wiping-out properties, indicating that interactions among cell wall pores are negligible. The independence of the hysteresis patterns concerning the influence of species and temperature can be interpreted in the following way: the origin of hysteresis is related to some common characteristics of woods like cell wall porosity. This hypothesis is consistent with the mechanism of the capillary condensation sorption, which is pore structure dependent. More explanations of the hysteresis patterns and quantitative analysis will be given in the next chapter by mathematical modeling.

The pore size characterization tests reveal the wide pore size distribution and dominance of 0.6 – 2.2nm cell wall pores in the hygroscopic range. The other characterization tests results regarding cell wall density and crystallinity and chemical composition are consistent with literature.

Chapter 4: Mathematical Modeling of Sorption Hysteresis in Wood

4.1 Introduction

In chapter 3, five experimental hysteresis patterns were identified for D-fir, aspen and WRC at 25 and 40°C. These patterns revealed interesting geometric characteristics of scanning curves, such as the non-intersection of primary descending curves and the wiping-out property. The quantitative descriptions of these scanning curves are usually performed through mathematical modeling.

Two types of mathematical models related to sorption hysteresis are described in literature. The first is based on the IDM (Everett and Whitton 1952, Everett and Smith 1953, Everett 1954 and 1955), interchangeably also called as the Preisach model (P-model), with Peralta (1995b, 1996) being the first to apply the ID-model to wood. However, great difficulty was experienced in obtaining the bivariate distribution function because of limited experimental data and double integration. Later Peralta and Bangi (1998a) adopted the similarity hypothesis proposed by Mualem (1973) to simplify the IDM distribution functions into a product of the two independent functions. Hysteresis could be predicted only from the data of the boundary curves data due to that hypothesis. However, disagreement was found concerning the slopes of predicted curves at reversal points. Thereafter, Peralta and Bangi (1998b) tried the Mualem (1974) based on the same similarity hypothesis. Carmeliet et al. (2005) also adopted this modeling approach, but they used “sorption sites”, a different interpretation, in characterizing the system. Peralta and Bangi (1998b) and Carmeliet et al. (2005) demonstrated that that model prediction did not agree with the data well.

Derome et al. (2008) further modified the IDM by excluding a non-hysteresis component, referred to as a film forming process, from the hysteresis model. Another contribution was to solve the numerical problems met by Peralta (1995b, 1996) through a combination of a series of functions with parameters fitted from experimental data. Recently, Patera et al. (2016) modeled hysteresis using the same approach found in Derome et al. (2008), but without the film forming non-hysteresis component (in the following referred to as MPM-A).

The second type of model is based on the geometric characteristics of scanning curves. Pedersen (1990) (as quoted in Frandsen et al. 2007) used a simple geometric property: all the scanning curves were constrained by boundary ascending and descending curves. Then the scanning curve slopes were modeled from weighting the slopes of the boundary curves and two shape parameters were introduced in that model. Frandsen et al. (2007) advanced Pedersen's model by adding a geometric assumption that the scanning curves were uniquely defined by the prevailing state (in the following referred to as FSD). Merakeb et al. (2009) modeled the boundary curves through a thermodynamic approach. Minor loops were then modified from boundary curves based on the relative position of the initial point and corresponding curve points.

Direct evaluation of existing models has been largely impeded by limited availability of scanning curve data. For example, in FSD and MPM-A, all dataset points were used for fitting the model parameters, and direct evaluations of the predicted values were not addressed. Another concern comes from the accuracy of available datasets in literature. Most of these were collected based on the salt-solution method (Peralta 1995a, Zillig 2009), the reliability of which is limited because of possible specimen's contamination. Therefore, it is necessary to evaluate the existing models based on datasets produced from a much more accurate sorption system. A more reliable alternative is the pattern (b) dataset in chapter 3 with close humidity interval settings. The pattern (e) dataset may also be proper for model prediction evaluation as it includes high-order minor loops.

The P-model will be applied in this chapter as, traditionally, discussion of IDM is often associated with physical interpretations. Here the mathematical aspects are in the foreground and the observed five hysteresis patterns are explained based on the geometric interpretations derived from the P-model. Then, an alternative nonparametric numerical implementation of the P-model will be attempted, based on the proposals of Mayergoyz (1991), and the results will be compared with existing models based on our own datasets.

4.2 The P-model and Its Geometric Interpretation

The aim of the mathematical model is to predict *M* given a certain history of *H*. The P-model is built by a large set of elementary hysteresis operators $\hat{\gamma}_{ul}$, which are represented by the rectangular loop with two critical values H_u and H_l where switching of operators occurs (Fig. 4.1) (Mayergoyz 1986, 1991).

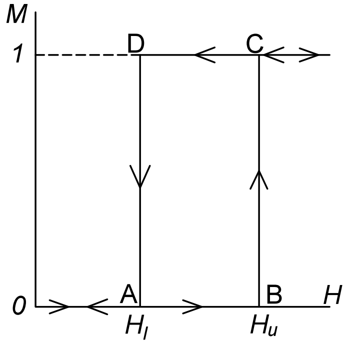

Figure 4.1: Elementary hysteresis operator $\hat{\boldsymbol{\gamma}}_{\boldsymbol{ul}}$.

Only two values, 0 and 1, are assumed for the output of these elementary operators. Then, by assigning an arbitrary weight function $\xi(H_u, H_l)$ to each elemental hysteresis operator, one has:

$$M = \iint_{H_u \geq H_l} \xi(H_u, H_l)\, \hat{\gamma}_{ul}\, H \, dH_u dH_l \tag{4.1}$$

The consideration of H history in this model is highly facilitated by its geometric interpretation. The idea is to construct a plane from H_u and H_l. As H_u is always larger or equal to H_l (Fig. 4.1), the focus is on the half-plane T where $H_u \geq H_l$ (shaded area in Fig. 4.2). Every point (H_u, H_l) in T corresponds to a unique value of $\hat{\gamma}_{ul}$, whereas T is the support of the weighting function $\mu(H_u, H_l)$.

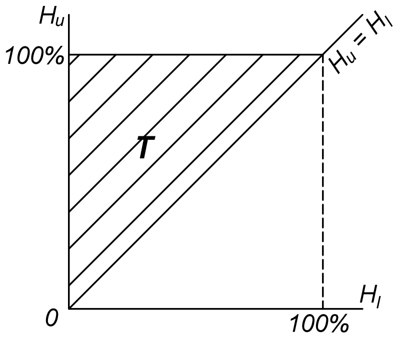

Figure 4.2: Geometric interpretation of the mathematical model: $\boldsymbol{H_u - H_l}$ diagram.

Assuming that wood is initially in an absolute dry state with $H = 0$ and $M = 0$, all the operators $\hat{\gamma}_{ul}$ in the region T are equal to 0. Then, with monotonic increase of H to some maximum value ω_1, all operators $\hat{\gamma}_{ul}$ with switching value H_u less than the current input value of H are turned to 1 from 0. Geometrically, the monotonic increase of H corresponds to the upward movement of the horizontal line $H_u = H$ along the vertical axis H_u (Fig. 4.3a). This upward motion leads to the subdivision of T into two regions, namely, S^+ with operators $\hat{\gamma}_{ul}$ equal to 1, and S^- with operators $\hat{\gamma}_{ul}$ equal to 0 (Fig. 4.3a). The upward movement of horizontal line $H_u = H$ is terminated when H reaches the maximum value of ω_1 (Fig. 4.3b).

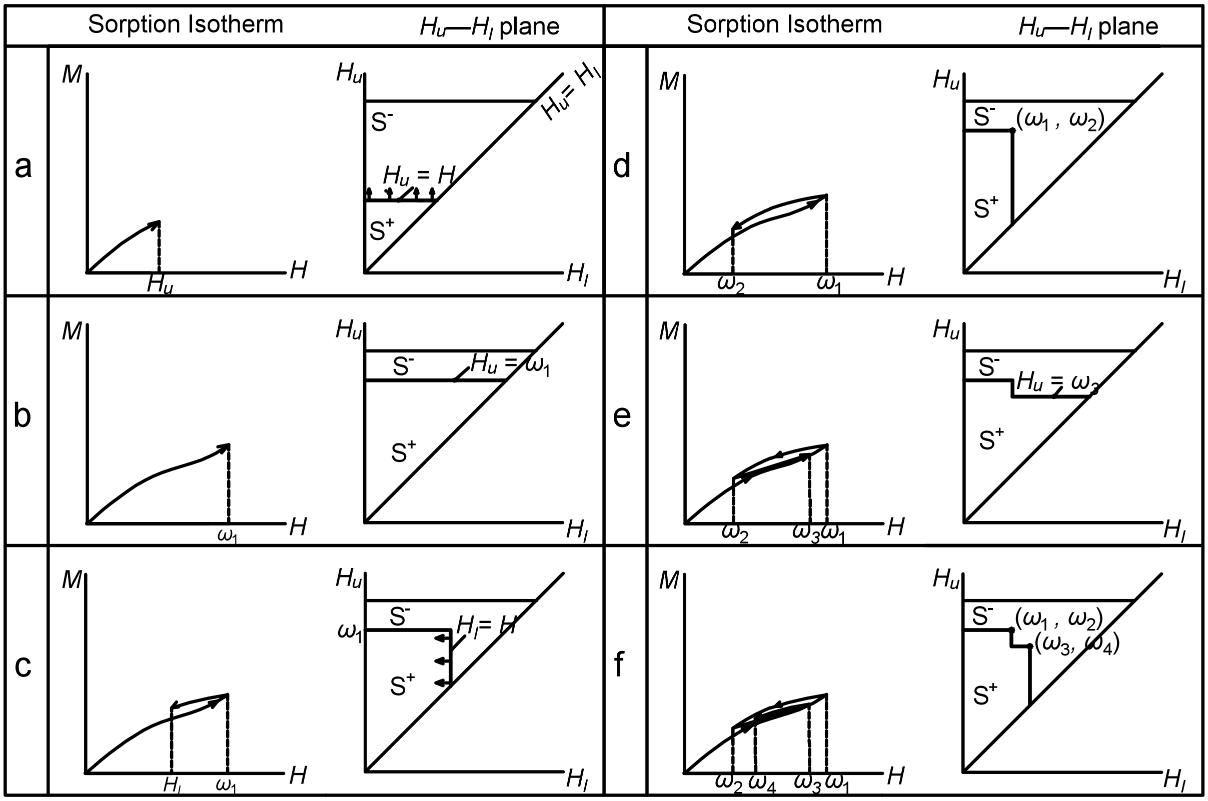

Figure 4.3: Sorption isotherms and corresponding $H_u - H_l$ plane geometric interpretation. a) 1st upward movement; b) termination of 1st upward movement; c) 1st leftward movement; d) termination of 1st leftward movement; e) 2nd upward movement; f) 2nd leftward movement.

Following, with monotonic decrease of H to some minimum value ω_2, all the operators $\hat{\gamma}_{ul}$ with switching value H_l above the current input value of H are turned to 1 from 0. Geometrically, the monotonic decrease of H corresponds to the leftward movement of the vertical line $H_l = H$ along the horizontal axis H_l (Fig. 4.3c). This leftward motion changes the previous subdivision of T—the interface between the regions S^+ and S^- is now constructed by two lines, namely, one horizontal and one vertical (Fig. 4.3c). The leftward movement of the horizontal line $H_l = H$ is terminated when H reaches the minimum value ω_2 (Fig. 4.3d). Should L be the interface line, then at the above specific moment, the coordinates of vertex of L is (ω_1, ω_2) (Fig. 4.3d).

At this point, H is monotonically increased again until some maximum value ω_3 ($\omega_3 < \omega_1$). Geometrically, this H increase results in the upward movement of a new horizontal line $H_u = H$ along the vertical axis H_u, which is terminated when the minimum value ω_3 is reached (Fig. 4.3e).

Subsequently, H is monotonically decreased until some minimum value ω_4 ($\omega_4 > \omega_2$). Geometrically, this decrease results in a second leftward movement of the vertical line $H_l = H$ along the horizontal axis H_l, which is terminated when the minimum value ω_4 is reached (Fig. 4.3f). At this specific moment, the interface L has two vertices with coordinates (ω_1, ω_2) and (ω_3, ω_4).

By repeating the above H cycles, the triangle T is subdivided into two regions: S^+ with operators $\hat{\gamma}_{ul}$ equal to 1, and S^- with operators $\hat{\gamma}_{ul}$ equal to 0. The interface L has vertices with coordinates of local maximum and minimum from the previous H cycles, and the final moving line is attached to the line $H_u = H_l$. Letting ω_t be the terminal value of H, the final line moves upwards if H increases (the horizontal line $H_u = \omega_t$ in Fig. 4.4a), and leftward if H decreases (the vertical line $H_l = \omega_t$ in Fig. 4.4b).

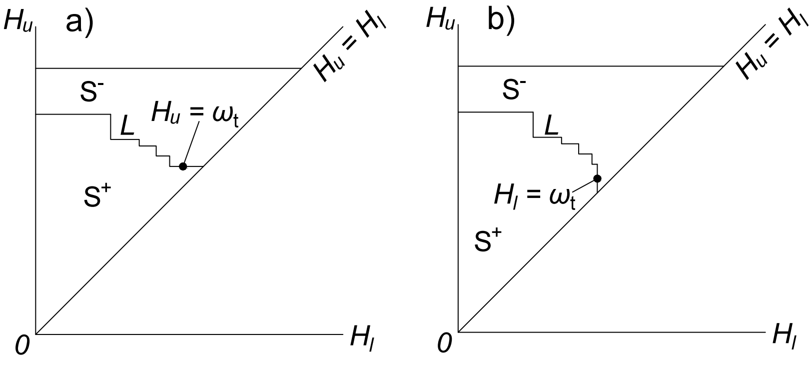

Figure 4.4: Subdivision of T with final line moving: a) upward; b) leftward.

As T is the support of the weighting function $\xi(H_u, H_l)$, the integral in Eq. (4.1) can be summed as two integrals, over S^+ and S^-, respectively:

$$M = \iint_{S^+} \xi(H_u, H_l)\,\hat{\gamma}_{ul}\,H\,dH_u dH_l + \iint_{S^-} \xi(H_u, H_l)\,\hat{\gamma}_{ul}\,H\,dH_u dH_l \tag{4.2}$$

Because

$$\hat{\gamma}_{ul}\,H = 1 \quad \text{if } (H_u, H_l) \in S^+ \tag{4.3}$$

and

$$\hat{\gamma}_{ul}\,H = 0 \quad \text{if } (H_u, H_l) \in S^- \tag{4.4}$$

Eq. (4.2) is simplified to

$$M = \iint_{S^+} \xi(H_u, H_l)\,dH_u dH_l \tag{4.5}$$

It follows that the instantaneous output value M of the model depends on the subdivision of triangle T, which is determined by the particular shape of the interface line L. As the vertices of these shapes come from the local extreme values of past input values of H, in this way, past H values directly affect future behavior of the model.

4.3 Mechanisms Underlying Hysteresis Patterns

An advantage of the P-model is that its geometric interpretation can be used without further quantitative modeling to explain the observed five experimental hysteresis patterns in chapter 3.

Patterns (a) and (b): Patterns (a) and (b) describe the geometric characteristics of the family of primary ascending and descending curves. Those curves do not intersect with each other and eventually merge at origin or M_{fps}. The explanation of these two patterns comes from the direct calculation of $\xi(H_u, H_l)$ and its physical meaning.

The $\xi(H_u, H_l)$ can be calculated from the family of primary scanning curves (Mayergoyz 1991). On a typical primary descending curve (Fig. 4.5a), let $M_{H_u'}$ be the M of the boundary ascending curve at $H = H_u'$, and $M_{H_u'H_l'}$, the M at $H = H_l'$ for the primary descending curve that is attached to the boundary ascending curve at $H = H_u'$.

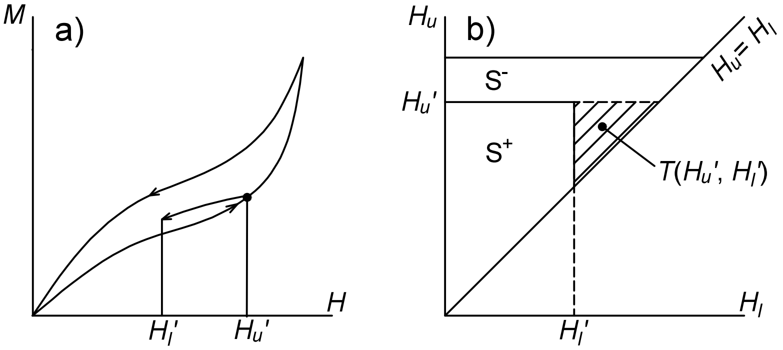

Figure 4.5: a) a typical primary descending curve;
b) corresponding $\boldsymbol{H_u - H_l}$ diagram.

Thereafter, the following function is defined as:

$$G(H_u', H_l') = M_{H_u'} - M_{H_u'H_l'} \tag{4.6}$$

and from the $H_u - H_l$ diagram (Fig. 4.5b):

$$M_{H_u'} - M_{H_u'H_l'} = \iint_{T(H_u',\, H_l')} \xi(H_u, H_l)\, dH_u dH_l \tag{4.7}$$

Then,

$$G(H_u', H_l') = \iint_{T(H_u',\, H_l')} \xi(H_u, H_l)\, dH_u dH_l \tag{4.8}$$

The integral over triangle $T(H_u',\, H_l')$ can be written as the following double integral form:

$$G(H_u', H_l') = \int_{H_l'}^{H_u'} \int_{H_l}^{H_u'} \xi(H_u, H_l)\, dH_u dH_l \tag{4.9}$$

By differentiating Eq. (4.9) twice (first with respect to H_l, and then with respect to H_u),

$$\xi(H_u', H_l') = -\frac{\partial^2 G(H_u', H_l')}{\partial H_u' \partial H_l'} \tag{4.10}$$

Inserting Eq. (4.6) into Eq. (4.10),

$$\xi(H_u', H_l') = \frac{\partial^2 M_{H_u' H_l'}}{\partial H_u' \partial H_l'} \tag{4.11}$$

By now, the formula to calculate $\xi(H_u, H_l)$ has been derived from the primary descending curves. Eq. (4.11) also allows for a geometric interpretation of $\xi(H_u, H_l)$. Assuming a series of experimental primary descending curves as plotted in Fig. 4.6a then, the first derivatives of $M_{H_u' H_l'}$ with respect to H_l' are slopes of these curves.

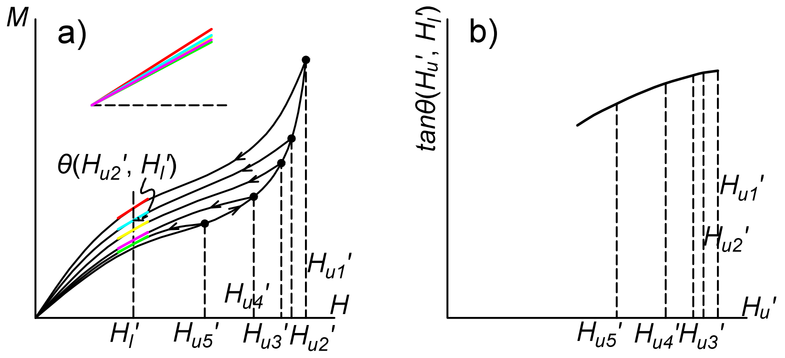

Figure 4.6: a) a family of primary descending curves: the color lines indicate the slopes at $\boldsymbol{H = H_l'}$; b) $\boldsymbol{\tan\theta(H_u', H_l') - H_u'}$ plot at a specified $\boldsymbol{H_l'}$.

Let $\theta(H_u', H_l')$ be the angle between the slope of the primary descending curve $M_{H_u' H_l'}$ and the H axis at the point $H = H_l'$, then

$$\frac{\partial M_{H_u' H_l'}}{\partial H_l'} = \tan\theta(H_u', H_l') \tag{4.12}$$

Eqs. (4.11) and (4.12) results in:

$$\xi(H_u', H_l') = \frac{\partial \tan\theta(H_u', H_l')}{\partial H_u'} \tag{4.13}$$

In Fig. 4.6a, the color lines indicate the slopes at an arbitrary value H_l' ($H_l' \leq H_{ui}', i \in \{1, 2, 3, 4, 5\}$). Then, a $\tan\theta(H_u', H_l') - H_u'$ plot is proceeded at each specified H_l' (Fig. 4.6b).

As M is always positive except for the absolute dry state of zero, it can be concluded that $\xi(H_u', H_l')$ is positive on the $H_u \geq H_l$ half plane except for the origin. From Eq. (4.13), for $\xi(H_u', H_l')$ to be positive, tan $\theta(H_u', H_l')$ must be increasing monotonically as a function of H_u', for any specified H_l'. This condition is satisfied if all primary descending curves are monotonically increasing functions of H_l', and they do not intersect with each other but merge at the origin. By now the formation of pattern (a) has been explained. Similar reasoning can be applied to pattern (b) if $\mu(H_u, H_l)$ is calculated from the family of primary ascending curves.

<u>*Pattern (c)*</u>: Let H_1 and H_2 be two H inputs with different past histories. Starting from some point of time, H_1 and H_2 vary back-and-forth between the same two consecutive extreme values: ω_- and ω_+ (Fig. 4.7a).

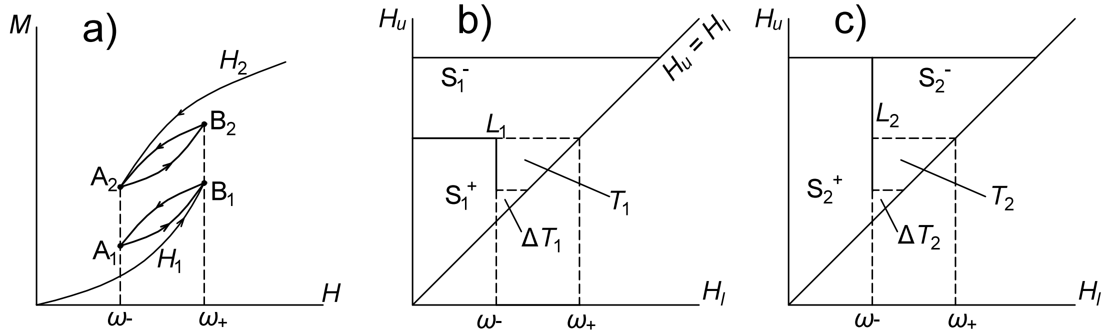

Figure 4.7: a) sorption isotherms H_1 and H_2 for relative humidity varying back-and-forth between the same two consecutive extreme values: ω_- and ω_+; b) $H_u - H_l$ diagram for H_1; c) $H_u - H_l$ diagram for H_2.

If hysteresis loops A_1B_1 and A_2B_2 from H_1 and H_2 have the same shape and size, these loops are defined as congruent by Mayergoyz (1991). The small deviation from this congruency property in experimental pattern (c) has been discussed in chapter 3. It is demonstrated here how this property can theoretically be derived from the P-model. The proof of this property requires that any equal increment of H_1 and H_2 lead to an equal increment of M_1 and M_2.

The $H_u - H_l$ diagrams for H_1 and H_2 (Figs. 4.7b and 4.7c) illustrate that as H_1 and H_2 are moving back and forth between ω_- and ω_+, the final parts of the interface line L_1 and L_2 are moving within the identical triangle T_1 and T_2. Assuming that after achieving the minimum value ω_-, H_1 and H_2 are increased by the same amount: $\Delta H_1 = \Delta H_2 = \Delta H$. Also from Figs. 4.7b and 4.7c, it is apparent that with the increase, the identical triangle ΔT_1 and ΔT_2 are added to the positive sets S_1^+ and S_2^+ and subtracted from the negative sets S_1^- and S_2^-. From Eq. (4.5), the corresponding M increments are given by:

$$\Delta M_1 = \iint_{\Delta T_1} \xi(H_u, H_l)\, dH_u dH_l \tag{4.14}$$

$$\Delta M_2 = \iint_{\Delta T_2} \xi(H_u, H_l)\, dH_u dH_l \tag{4.15}$$

Since $\Delta T_1 = \Delta T_2$,

$$\Delta M_1 = \Delta M_2 \tag{4.16}$$

As ΔH is arbitrary within the range (0, $\omega_+ - \omega_-$), Eq. (4.16) holds for any point in the lower branches of two minor hysteresis loops thus, proving congruence of the lower branches. Similarly, assuming that after achieving the maximum value ω_+, H_1 and H_2 are decreased by the same amount: $\Delta H_1 = \Delta H_2 = \Delta H$. Eq. (4.16) can also be proven to hold true for the upper branches, thus pointing to the fact that the upper branches are also congruent. In sum, the congruence for the whole loops (pattern c) can be considered as proven.

Pattern (d): Pattern (d) reveals that any point within the major hysteresis loop can be reached more than one way. The same *M* means that the integration from the support S^+ in the $H_u - H_l$ diagram is the same, and different hygroscopic histories indicate different interface lines L. Therefore, the proof of this patterns demands the existence of two different interface lines with appropriate supports S^+ that lead to the same integration. Since different supports correspond to different weighting functions $\xi(H_u, H_l)$, the support areas can be different. Fig. 4.8 gives such an example where L_1 and L_2 are two interfaces formed from two different H histories.

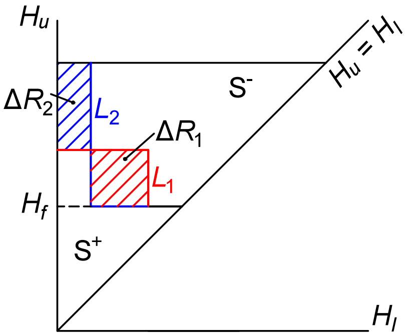

Figure 4.8: A demonstration of the same S^+ with different interface lines L_1 and L_2 in the $H_u - H_l$ diagram.

The differences of the interfaces are indicated by red color for L_1, and blue color, L_2. The differences of the supports are indicated by the shaded rectangular areas ΔR_1 and ΔR_2. Since the areas of ΔR_1 can be finely tuned by the final movement of $H_u = H_f$, the equality of integration based on ΔR_1 and ΔR_2 can be satisfied.

Pattern (e): Patten (e) illustrates the wiping-out property summarized by Mayergoyz (1991). That is also supported by the $H_u - H_l$ diagram. Consider a particular past history characterized by a decreasing sequence $\{\omega_1, \omega_3, \omega_5, \omega_7\}$ of local H maxima and an increasing sequence $\{\omega_2, \omega_4, \omega_6, \omega_8\}$ of local H minima. A typical $H_u - H_l$ diagram is shown in Fig. 4. 9.

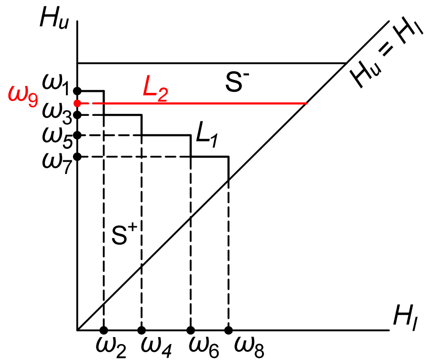

Figure 4.9: $H_u - H_l$ diagram with local extreme sequences $\{\omega_1,\ \omega_3,\ \omega_5,\ \omega_7\}$, $\{\omega_2,\ \omega_4,\ \omega_6,\ \omega_8\}$, and local extreme ω_9 above ω_3.

At this time, H is monotonically increasing to a maximum value of ω_9, which is larger than ω_3. This increment leads to a new division of T as shown from the interface line L_2 in Fig. 4.9. Comparing L_1 and L_2 in Fig. 4.9, it is obvious that all the vertices in L_1 lower than ω_9 have been wiped out. It also means that the H histories associated with these vertices are wiped out.

4.4 A Nonparametric Numerical Implementation of the P-Model

In the following discussion, a numerical approach is demonstrated, which is based on the proposals of Mayergoyz (1991), which does not require any unknown parameters to be estimated from data fitting. This modified P-model shall be named MPM-B contrary to MPM-A developed by Patera et al. (2016).

Assuming that H_{uk} and H_{lk} $(k = 1, 2, 3, \dots, n)$ are alternating past maximums and minimums of H then, a typical $H_u - H_l$ plot is like Fig. 4.10a.

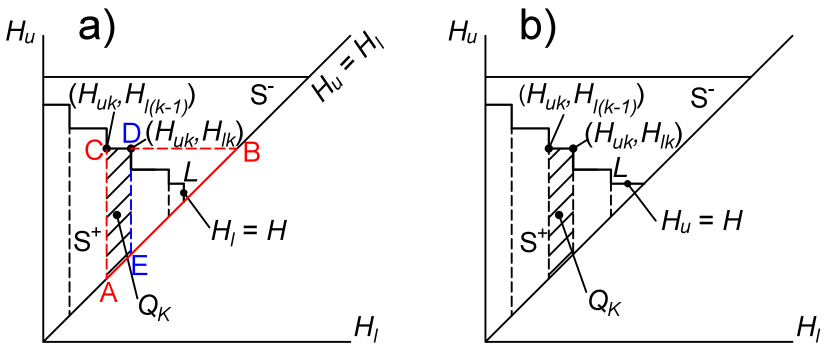

Figure 4.10: Typical $H_u - H_l$ plot for alternating past maxima and minima: H_{uk} and H_{lk} ($k = 1, 2, 3, \ldots, n$). a) H is decreasing at the last stage; b) H is increasing at the last stage.

The positive set S^+ can be divided into a group of trapezoids Q_k. Thus, the following equation can be derived:

$$\iint_{S^+} \xi(H_u, H_l)\, dH_u dH_l = \sum_{k=1}^{n} \iint_{Q_k} \xi(H_u, H_l)\, dH_u dH_l \tag{4.17}$$

Each trapezoid can be calculated as the difference of two triangles, $T(H_{uk}, H_{l(k-1)})$ and $T(H_{uk}, H_{lk})$ (triangles ABC and BDE in Fig. 10a). Thus, each summation element on the right-hand side of Eq. (4.17) becomes:

$$\iint_{Q_k} \xi(H_u, H_l)\, dH_u dH_l =$$

$$\iint_{T(H_{uk}, H_{l(k-1)})} \xi(H_u, H_l)\, dH_u dH_l - \iint_{T(H_{uk}, H_{lk})} \xi(H_u, H_l)\, dH_u dH_l\ ) \tag{4.18}$$

Then from Eq. (4.8),

$$\iint_{T(H_{uk}, H_{l(k-1)})} \xi(H_u, H_l)\, dH_u dH_l = G(H_{uk}, H_{l(k-1)}) \tag{4.19}$$

and

$$\iint_{T(H_{uk}, H_{lk})} \xi(H_u, H_l)\, dH_u dH_l = G(H_{uk}, H_{lk}) \tag{4.20}$$

Introducing Eqs. (4.19) and (4.20) into Eq. (4.18), one has

$$\iint_{Q_k} \xi(H_u, H_l)\, dH_u dH_l = G\left(H_{uk}, H_{l(k-1)}\right) - G(H_{uk}, H_{lk}) \tag{4.21}$$

Then from Eqs. (4.5), (4.17) and (4.21),

$$M = \sum_{k=1}^{n}\left(G\left(H_{uk}, H_{l(k-1)}\right) - G(H_{uk}, H_{lk})\right) \tag{4.22}$$

If at the last stage H decreases, then the final part of interface line L is vertical as indicated in Fig. 4.10a. Then Eq. (4.22) can be written as:

$$M = \sum_{k=1}^{n-1}\left(G\left(H_{uk}, H_{l(k-1)}\right) - G(H_{uk}, H_{lk})\right) + G\left(H_{un}, H_{l(n-1)}\right) - G(H_{un}, H) \tag{4.23}$$

If at the last stage, H is increasing, then the final part of interface line L is horizontal as indicated in Fig. 4.10b. Then Eq. (4.22) can be written as,

$$M = \sum_{k=1}^{n-1}\left(G\left(H_{uk}, H_{l(k-1)}\right) - G(H_{uk}, H_{lk})\right) + G\left(H, H_{l(n-1)}\right) \tag{4.24}$$

According to the definition of $G(H_u, H_l)$, Eq. (4.6), it is found that in case of decreasing H in the last stage:

$$M = \sum_{k=1}^{n-1}\left(M_{H_{uk}H_{lk}} - M_{H_{uk}H_{l(k-1)}}\right) - M_{H_{un}H_{l(n-1)}} + M_{H_{un}H} \tag{4.25}$$

and in case of increasing Hin the last stage:

$$M = \sum_{k=1}^{n-1}\left(M_{H_{uk}H_{lk}} - M_{H_{uk}H_{l(k-1)}}\right) + M_H - M_{H\,H_{l(n-1)}} \tag{4.26}$$

The derived explicit expressions (4.25) and (4.26) for M are based on the experimental data from the boundary ascending and primary descending curves.

The following steps were followed to write the codes in R (version 3.0.2) for performing the numerical calculations:

1) A square mesh covering the limiting triangle T based on experimental datasets from the boundary curves and pattern (b) were created (Fig. 4.11).
2) The dominate alternating maximums and minimums: H_{uk} and H_{lk} ($k = 1, 2, 3, \ldots, n$) were determined from the input H based on its history.

3) The bivariate spline interpolation function (the command “interpp” in the package “akima”) was used to obtain the values of $M_{H_{uk}H_{lk}}$, $M_{H_{uk}H_{l(k-1)}}$, $M_{H_{un}\,H}$ etc. in Eq. (4.25) or Eq. (4.26) based on mesh values.
4) M was calculated by Eq. (4.25) if H is decreasing at the last stage, or by Eq. (4.26) in the opposite case.

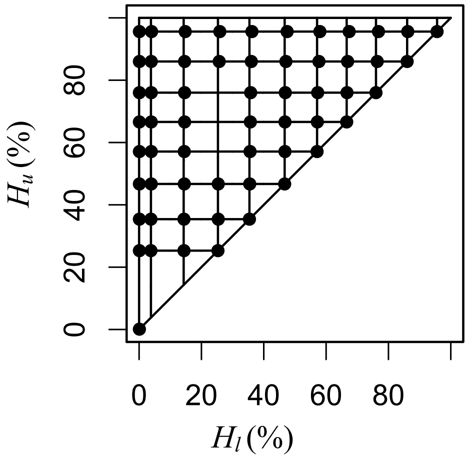

Figure 4.11: Generated square mesh covering the limiting triangle T based on experimental dataset of boundary and primary scanning curves.

4.5 Model Predictive Accuracy

Wood in service is usually subjected to various *H* fluctuations, and therefore it is important to predict high-order scanning curves. *M* is predicted according to the *H* setting in pattern (e) and then, compared to experimental data. Small deviations were found between boundary ascending curve data from pattern (b) and (e), that probably resulted from the equipment’s intrinsic fluctuations. For a better model evaluation, the first reversal point in pattern (e) was offset to be same as the corresponding point in pattern (b).

Figs. 4.12a1–c1 are typical plots of modeled hysteresis patterns for D-fir, aspen, and WRC at 25°C. The dashed line indicates the modeled values, and the solid line, the experimental data points. Separate plots (Figs. 4.12a2–c2) are presented for the two datasets to demonstrate the differences between them more clearly. All predicted curves demonstrate satisfactory wiping-out property, and predicted points match well with data for aspen and WRC. However, for D-fir, the deviation is larger.

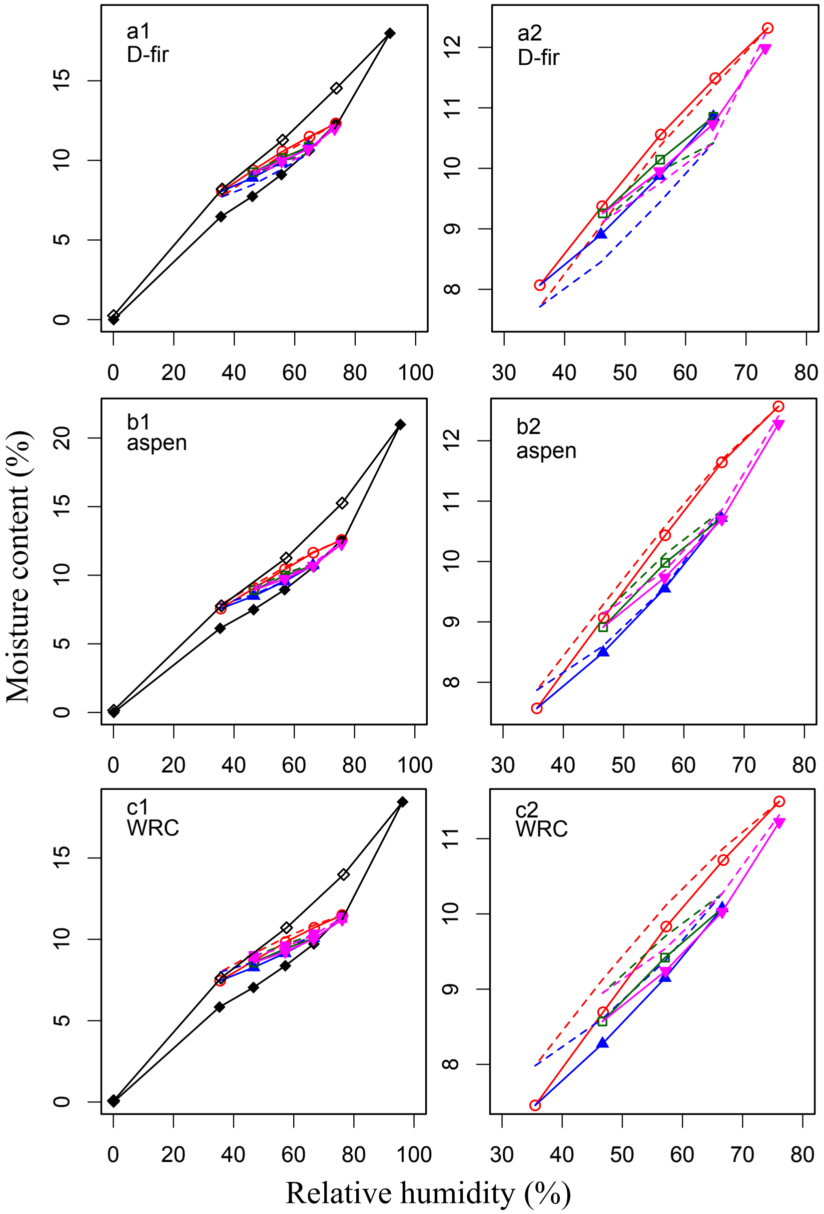

Figure 4.12: predicted scanning curve values (dash lines) versus data (solid lines) at 25°C using MPM-B. a: D-fir; b: aspen; c: WRC. Solid symbols represent adsorption process and open symbols represent desorption. Symbol diamond indicates the boundary curve data points, and symbols circle, triangle, square, and inverted triangle indicate the primary to 4th scanning curve data points.

The model performance was evaluated by means of the variables *SSE*, *MSE*, and *NMSE*.

Sum of squared error (*SSE*):

$$SSE = \sum_{i=1}^{n} \Delta M_i^{\ 2} \tag{4.27}$$

where ΔM_i is the difference between modeled M value and data for the ith evaluation point and n is the total number of evaluated points.

Mean of squared error (*MSE*):

$$MSE = \sqrt{SSE/(n-1)} \tag{4.28}$$

Normalized mean of squared error (*NMSE*):

$$NMSE = MSE/(\frac{1}{n}\sum_{i=1}^{n} M_i) \tag{4.29}$$

where M_i is the moisture content data for the ith evaluation point.

Table 4.1 (data at 25°C) summarizes the results of the tested samples for each species based on the above variables. All aspen and WRC samples show high levels of accuracy. However, for D-fir, the overall deviation is larger. This calculation confirms the result observed from the previous plots (Fig. 4.12).

Table 4.1: Summary of accuracy of modeled hysteresis patterns (e) for D-fir, aspen, and WRC at 25 and 40°C.

		Data at 25°C			Data at 40°C		
Species	Sample	SSE	MSE	NMSE (%)	SSE	MSE	NMSE (%)
D-fir	1	2.7031	0.4746	4.75	0.4862	0.2013	2.18
D-fir	2	5.2148	0.6592	6.55	0.7654	0.2526	2.68
D-fir	3	0.7013	0.2417	2.39	0.7121	0.2436	2.70
Aspen	1	0.3174	0.1626	1.64	5.3854	0.6699	7.73
Aspen	2	0.2886	0.1551	1.58	0.1471	0.1107	1.30
Aspen	3	0.0925	0.0878	0.96	1.2278	0.3199	3.65
WRC	1	1.1579	0.3106	3.31	0.1804	0.1226	1.42
WRC	2	0.5024	0.2046	2.18	0.3471	0.1701	2.02
WRC	3	0.3940	0.1812	1.89	0.2709	0.1503	1.82

The model was also evaluated for the three species at the temperature level of 40°C. Table 4.1 shows that the model works also well as in the case of 25°C. There should be no surprise with this result since the temperature variable is not part of the model structure. In addition, similar hysteresis patterns were found at 25°C and 40°C in chapter 3.

4.6 Comparison of FSD, MPM-A and MPM-B

Two representative models in literature, namely, the FSD and MPM-A models were evaluated based on this study's dataset. Fig. 4.13a shows the fitted primary descending curves based on the FSD for a WRC sample at 25°C. The 0.2603 MSE and 4.90% NMS value is comparable to the prediction errors based on the MPM-B model (Table 4.1, data at 25°C, WRC sample 2).

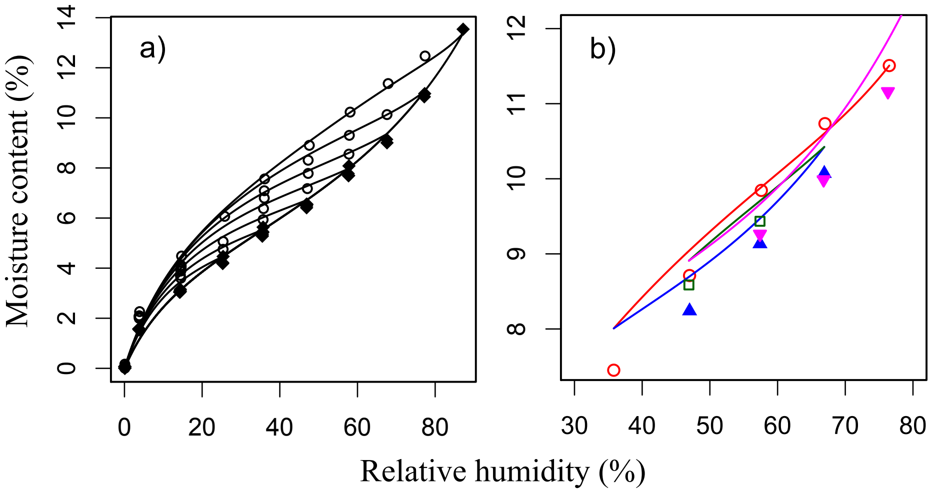

Figure 4.13: Fitted and predicted scanning curves for WRC at 25°C using the FSD. a: fitted primary scanning curves; b: predicted high-order scanning curves. Solid symbols represent adsorption process and open symbols represent desorption. Symbol diamond indicates the boundary curve data points, and symbols circle, triangle, square, and inverted triangle indicate the primary to 4th scanning curve data points.

Qualitatively, these primary descending curves are not interacting with each other and tend to merge at the origin, following the geometric characteristics of the hysteresis pattern (b). However, the predicted high-order scanning curves (Fig. 4.13b) are not acceptable as they largely deviate the wiping-out property illustrated from pattern (e), although the calculated 0.3422 *MSE* and 3.64% *NMSE* seems to be adequate.

Unfortunately, the seven unknown parameters in the MPM-A cannot be estimated from the current dataset using the statistical software R. It is possible that too many parameters are included in the nonlinear model, which works satisfactorily only in case of specific datasets. Alternatively, pattern (e) was predicted based on the dataset provided by Zillig (2009). Fig. 4.14a shows that the wiping-out property is maintained well, however, the near disappearance of the inner loop is not acceptable.

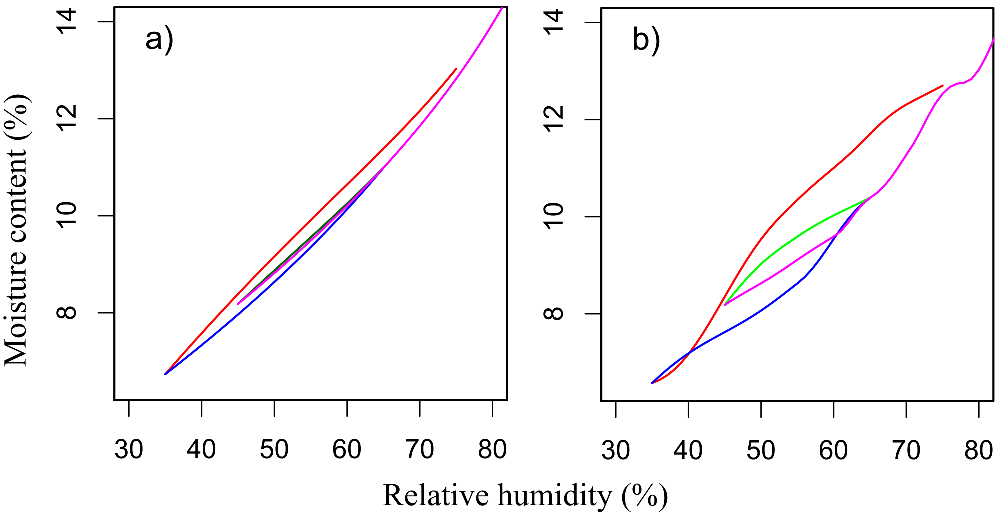

Figure 4.14: Predicted hysteresis pattern (e) using Zillig's (2009) dataset: a) from the MPM-A; b) from the MPM-B.

The evaluation of the MPM-B performance with a different dataset is also of interest. Fig. 4.14b presents the predicted pattern (e) from the MPM-B with Zillig's (2009) data. Comparing Figs.

4.14a and 4.14b, it is noticed that larger hysteresis is predicted from the MPM-B. The wiping-out property is well maintained, however, the curves show unrealistic fluctuations. These fluctuations are caused by the instability in interpolating the sparse and less accurate dataset by means of the bivariate spline interpolation function included in the MPM-B. This illustrates one potential problem of the MPM-B, i.e. that it relies too much on the input dataset. A good performance is expected only in case of accurate, sufficient, and preferably evenly distributed dataset.

4.7 Conclusion

The geometric interpretation of the P-model satisfactorily explained the five hysteresis patterns identified in the experimental phase indicating its distinctive advantage over other mathematical models. Further quantitative modeling with a nonparametric numerical implementation could be considered as satisfactory. From the consistence and differences presented by the tested three species, it is expected that the developed model will work for most wood species, but with different degrees of accuracy in the temperature range of 25 to 40°C. Compared to FSD and MPM-A, our proposed MPM-B has the advantage of predicting the high-order scanning curves with high accuracy without relying on any unknown parameters. However, our approach requires a large, accurate and evenly distributed input dataset from experimentally obtained primary descending curves.

Chapter 5: Physical Modeling of Sorption and Hysteresis

5.1 Introduction

The sorption experiments in chapter 3 have suggested the independence of cell wall pores. Therefore, the hysteresis origin based on the currently proposed theory becomes the existence of metastable states in a single cell wall pore. In this chapter, this origin will be demonstrated through physical modeling of water sorption and hysteresis in wood.

Different from mathematical modeling, physical modeling requires clear underlying mechanisms and proper simplification of the wood-water system. Although several theories have been proposed to explain the origin of hysteresis (chapter 2), few have been applied towards the development of a physical model.

Chen and Wangaard (1968) focused on hysteresis for *H*s above 60% and assumed capillary condensation as the sorption mechanism. Then, they modeled hysteresis with Kelvin's equation by assuming different contact angles for water filling and emptying the capillary pores. Popper et al. (2009) also claimed that hysteresis is related to capillary condensation and used Kelvin's equation in modeling it. However, they assumed the same contact angle, but different interface configurations, i.e. a cylindrical concave surface for adsorption and a spherically concave surface for desorption. Merakeb et al. (2009) modeled the sorption based on enthalpy of sorption. Thereafter, hysteresis was modeled through different enthalpy in adsorption and desorption processes. Willems (2014) proposed that hysteresis originated from "non-equilibrium excess sorption sites being occupied". The relaxation of these sites was modeled as a first-order rate process with constant relaxation time.

Physical modeling of hysteresis cannot be separated from modeling of the sorption process. Most existing models assumed capillary condensation as the sorption mechanism, which has been theoretically argued based on the micro-mesoporous feature of cell walls in chapter 2. Further examination of capillary condensation in the entire hygroscopic region is needed. Another concern is oversimplification of the wood-water system, which leads the developed "physical" models to resemble mathematical ones.

The intent of this chapter is to simplify the wood-water system, and subsequently develop a physical model capable of describing both sorption and hysteresis. The capillary condensation and water metastable states will be examined using the molecular simulation technique. In other words, the proposed origin of hysteresis based on IDM will be evaluated.

5.2 Methodology

The starting point for model development is the plausible simplification of wood-water systems. Since water vapor is unlikely to condense inside cell lumina in the hygroscopic range, the focus here is the system composed of cell walls and water. The pore size characterization tests in chapter 3 revealed the wide pore size distribution and dominance of 0.6 – 2.2nm cell wall pores in the hygroscopic range. Regardless of swelling or shrinking during sorption, the final equilibrium states of the system can be simplified to water confined in cell wall nanopores. Not only is this nanopore-water system simple enough to emulate behavior of water in cell walls, but it is also flexible enough to analyze the effect of different wall polymers on adsorbed water. Cell wall swelling is compensated by adjusting pore size distributions. The later are then used as superposition weights to restore the gross sorption isotherm from simulated single isotherms at a series of pore sizes.

The main challenge following comes from the extreme small size of the cell wall pores. Studies on fluids confined in nanopores have revealed that these liquids exhibit very different heterogeneous structures compared to homogeneous structures in bulk states due to strong interactions from the pore walls (Lowell et al. 2004). A major outcome from this heterogeneous structure is that it becomes less accurate to apply some macroscopic thermodynamic approaches such as wetting, surface tension and contact angle, just to name a few. What matters most in this study is the validity of Kelvin's equation in predicting the critical relative pressure (or relative humidity) where capillary condensation occurs. The original Kelvin's equation, assuming the cylindrical pore shape and zero wetting angle, has the form:

$$ln\frac{p}{p_0} = \frac{-2\gamma V_L}{r_p R\tau} \tag{5.1}$$

where p (Pa) is critical pressure where capillary condensation happens; p_0 (Pa) is saturated pressure at a constant temperature; V_L (m^3 mol^{-1}) is mole volume of the bulk liquid; r_p (m) is the radius of the pore; R is gas constant (8.314 J mol^{-1} K); τ (K) is temperature; γ (N m^{-1}) is surface tension of the liquid. As early as 1972, Skaar had questioned the validity of Eq. (5.1) for capillary radii below 10nm. From Table 1.5 in his book, the calculated radius was 10.1nm at $\frac{p}{p_0} = 0.9$, which is much larger than the characterized cell wall pore size in this study.

Cohan (1938) modified Eq. (5.1) by assuming that the pore walls were covered by a thin film of adsorbed liquid at the onset of pore condensation. The modified equation has the form:

$$ln\frac{p}{p_0} = \frac{-2\gamma V_L}{R\tau(r_p - t_c)} \tag{5.2}$$

where t_c (m) is the thickness of adsorbed films before condensation. Eq. (5.2) is supposed to be more accurate in predicting capillary condensation in smaller nanopores. However, Neimark and Ravikovitch (2001) found that this modified equation was in error even for pores as large as 20nm.

They also examined another model, the Derjaguin-Broekhoff-de Boer (DBdB) in which influence of the surface force on the equilibrium and stability of adsorption films was further considered. They reported that the DBdB equation was justified for pores with diameters larger than 7nm, and that significant differences were found for pores smaller than 4nm. Indeed, more advanced microscopic theories are required to model the cell wall nanopore-water system.

Density function theory (DFT) and molecular simulation have been developed to describe the sorption and phase behavior of fluids confined in nanoporous materials (Lowell et al. 2004). Both approaches worked well for simple fluids such as Ar, N_2, CO_2, amongst others, in silica or carbon systems (Ravikovitch et al. 2001, Neimark and Ravikovitch 2001), but application of DFT on complicated polar fluids like water has not been satisfactory (Gillan et al. 2016). Hence, in this study, the molecular simulation approach was chosen.

Molecular simulation stems from statistical mechanics and discreet time Markov chains (dtMC) (Frenkel and Smit 1996, Allen and Tildesley 1989). It aims at generating a series of microscopic configurations of the system with probability distributions conforming to the ones calculated from statistical mechanics. Nevertheless, generating strictly independent multivariate random variables with complicated distribution functions in simulation is very difficult. This problem was solved by introducing dtMC: a probability model that generates less-strictly independent random variables. The irreducible ergodic dtMC guarantees that once the chain reaches equilibrium, a stationary distribution of configurations that are independent is obtained (Ross 2010). Moreover, the ergodic theorem ensures that average over time, equals average over space states. Practically, in a simulation, trial moves like translation and rotation are performed to each particle (i.e. water molecule) in the system (Frenkel and Smit 1996). These moves are accepted or rejected based on rules derived from statistical mechanics and controlling algorithms of dtMC transitions. Depending on the size (number of water molecules) of the simulated system, usually 10^6 – 10^7 steps are needed to allow the dtMC to reach equilibrium. Then, another 10^7–10^8 steps are required to allow a good sampling of the microscopic configurations. Eventually, the simulated equilibrium microscopic configurations will allow calculation of most thermodynamic properties of interest, such as density and energy of the system. Details of the models and simulations are given in the following two sections.

5.2.1 Cell wall and water models

The cell wall model is composed of solid cell wall substance and evenly distributed cylindrical nanopores with different sizes, where water molecules are adsorbed (Fig. 5.1).

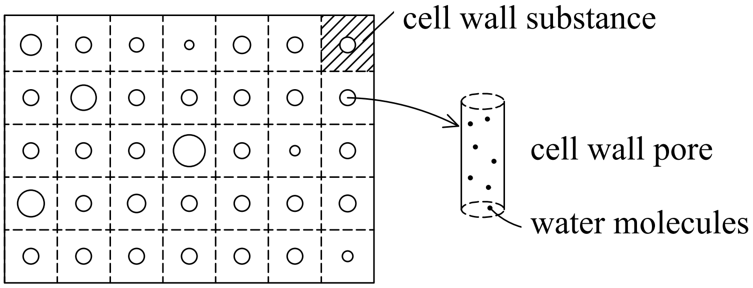

Figure 5.1: Schematic design of the cell wall model.

These pores are independent of each other and have full access to the environment. More specifically, "independent" means these pores are not connected to each other, and filling/emptying one pore will not affect the others. The pore walls are modeled as rigid walls composed of carbon and oxygen atoms. The detailed molecular configurations of these atoms are not considered here, and hydrogen atoms are neglected due to their negligible contribution to interaction energy calculations. Two types of pore walls PW_1 and PW_2 have been investigated.

PW_1 is associated with polysaccharides (amorphous cellulose and hemicellulose), with more sorption sites (accessible hydroxyls and other polar groups) and stronger wall-water interactions; PW_2 is associated with lignin, with fewer sorption sites and weaker wall-water interactions.

The sorption sites are modeled as negative energy pits attached to walls (Fig. 5.2). The number of energy pits is set as one pit for every 0.5nm for PW_1 and one for every 1.5nm for PW_2 (Hill 2006) based on the estimated number of accessible hydroxyl groups associated with polysaccharides and lignin. Table 5.1 summarizes the number of pits for walls with different sizes at a pore length of 6.332nm. Here "*nps_c*" represents number of pits in the lateral direction, and "*nps_l*", number of pits in the longitudinal direction.

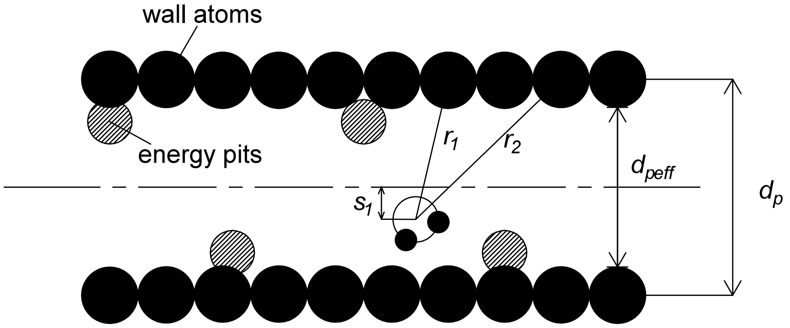

Figure 5.2: Schematic of effective cylindrical pore diameters and energy pits with one water molecule inside.

Table 5.1: Number of pits for walls with different sizes.

Pore Diameter (nm)	PW_1		PW_2	
	nps_c	*nps_l*	*nps_c*	*nps_l*
0.63	3	12	3	4
0.95	3	12	3	4
1.6	4	12	4	4
2.2	4	12	4	4

The radius of the energy pits is set at 0.3166nm, the collision diameter of water molecules, and its strength was set at 4.5kal/mol, an average value for hydrogen bonding energy in liquid bulk water. By conformational analysis, Pizzi et al. (1987a, 1987b) theoretically estimated sorption energy mostly around 5.5 kcal/mol for cellulose I crystals and 6.5kcal/mol for amorphous cellulose. On the other hand, the initial sorption energy at 0% *M* was estimated to be 5.4kcal/mol from heat of wetting measurements (Kelsey and Clark 1956, Walker 2006).

Water is represented by the extended simple point charge SPC/E model (Fig. 5.3) (Karniadakis et al. 2005). One site with charge -0.8476*e* (*e* is elementary charge, approximately $1.602 \times 10\text{-}^{19}$C) corresponds to the oxygen atom, and the other two sites with charge +0.4238*e*, correspond to the hydrogen atoms. The distance between the oxygen site and hydrogen site is 0.1nm, and the H-O-H angle is 109°, and both are kept constant during the simulation.

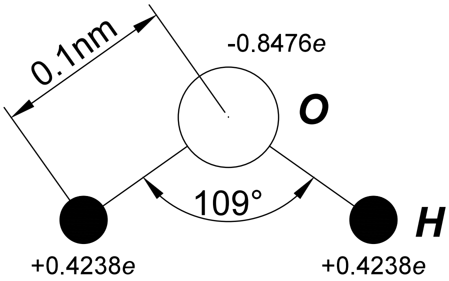

Figure 5.3: The extended simple point charge water model.

5.2.2 Simulation details

The simulation system is water confined in infinite long cylindrical nanopores at different *H*s under constant temperature. Grand canonical Monte Carlo (GCMC) was used to calculate sorption isotherms for each single pore of variable size. In a grand canonical ensemble, the system temperature, pore volume and environmental chemical potential are kept constant. Under a specified chemical potential (corresponding to a specified *H*), the number of water molecules inside the pore is calculated, thus obtaining one sorption isotherm equilibrium point. Sorption hysteresis is then obtained by comparing adsorption and desorption curves.

The key to molecular simulation is the calculation of the system interaction energy since the dtMC move is controlled by the energy difference. The interaction energy of water molecules is calculated as the sum of the Lennard-Jones (LJ) potential and the Coulombic potential. The LJ potential energy u_{LJ}^{ij} between particle i and j with a displace r is calculated as:

$$u_{LJ}^{ij} = 4\varepsilon \left(\frac{\sigma}{r}\right)^{12} - \left(\frac{\sigma}{r}\right)^{6} \tag{5.3}$$

where ε (J) is the depth of the well at the minimum in $u(r)$, and the collision diameter σ (m) is the separation at which $u(r) = 0$.

The Coulombic potential between particle i and j with a displace r is calculated as

$$u_{C}^{ij}(r) = \frac{1}{4\pi\varepsilon_0}\frac{q_i q_j}{r} \tag{5.4}$$

where q_i (C) and q_j (C) are charges particle *i* and *j* carried, and $\varepsilon_0 = 8.854\ Fm^{-1}$ is the vacuum permittivity.

The interaction energy U (J) between one water molecule and the pore wall can be calculated by integrating Eq. (5.3) over the wall atoms,

$$U(s_1) = \int_{solid} u_{LJ}^{ij}(\boldsymbol{r})\, d\boldsymbol{r} \tag{5.5}$$

where s_1 (nm) is the distance of the water molecule from the pore center, and $\boldsymbol{r}$ (nm) is the displacement vector between the water molecule and the wall atom (Fig. 5.2). The integration in Eq. (5.5) is performed according to Peterson et al. (1986).

The LJ potential, as well as geometric and charge parameters for water are taken from Berendsen et al. (1987). The determination of the LJ parameters between the pore wall and water is more complicated. Theoretically, the walls are composed of carbon and oxygen atoms, so the interaction energy should be bounded by the interaction of water with the pure carbon wall and the pure oxygen wall. Following this, the interaction parameters of water with the carbon nanotubes seem to be suitable references. Because of higher percentage of oxygen atoms in PW_1, the interaction strength of PW_1 is expected to be higher than that of PW_2. Therefore, the LJ parameters in Walther et al. (2001) and the ones in Kaukonen et al. (2012) were used for PW_1-water and PW_2-water interactions, respectively. Table 5.2 summarizes the LJ potential parameters used in the current simulations.

Table 5.2: The LJ potential parameters in simulation.

Interaction	LJ Potential Parameters	
	ε/k_B (K)	σ (nm)
water-water	78.23	0.3166
PW_1-water	58.29	0.3281
PW_2-water	37.60	0.3190

The number density of wall atoms N_s is defined as number of atoms per unit wall volume. Assuming an average wall density of 1500kg/m^3, and a chemical composition $(C_6H_{12}O_5)_n$, it can be calculated as:

$$N_s = \frac{1.5g}{164g/mol} \times N_A \times 11cm^{-3} = 60.5nm^{-3} \tag{5.6}$$

where N_A is the Avogadro constant, and 11 comes from 6 “C” atoms and 5 ”O” atoms in each “$C_6H_{12}O_5$” monomer.

Let ε_{ww} and σ_{ww} be LJ parameters of water-water interaction. The simulated pores have a length of $l_p = 20\sigma_{ww}$ with diameters $d_p = 3\sigma_{ww}$, $4\sigma_{ww}$, $6\sigma_{ww}$ and $8\sigma_{ww}$, corresponding to effective diameters of 0.63nm, 0.95nm, 1.6nm and 2.2nm, respectively. Here, d_p (nm) is defined as the distance between centers of opposite wall atoms. Effective pore diameters d_{peff} (nm) is estimated as $d_p - \sigma_{ww}$ (Fig. 5.2). Periodic boundary condition is only applied to the pore length direction.

The simulation for each point at the sorption isotherm is run for 4×10^7 steps for initial conditioning and another 6×10^7 steps for equilibrium. Each step includes a trial DTMC move chosen randomly from translation, rotation, insertion and removal of water molecules. Two temperature levels, namely, 25 and 40°C were run for all simulated sorption isotherms.

5.3 Results and Discussion

5.3.1 Simulated sorption isotherms

Fig. 5.4 is a representative plot of simulated sorption isotherms of a PW_1 pore at 25°C. Here, relative density is defined as number density of water within the pore divided by number density of bulk liquid water, and it describes the quantity of water molecules adsorbed in a single pore. The adsorption branch is barely detectable until *H* reaches a critical point A where an abrupt increase of relative density occurs. Then, the curve increases slowly with *H*, and eventually levels off. The desorption branch decreases gradually with *H* until reaching critical point B where abrupt decrease of relative density occurs. The loop enclosed by the two branches shows hysteresis.

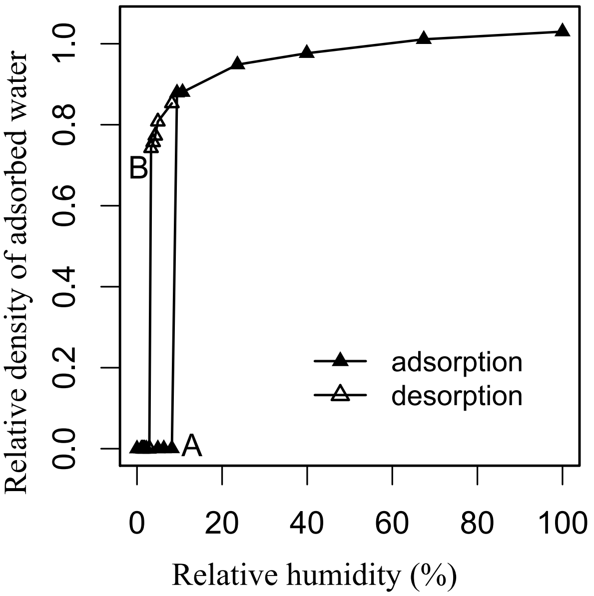

Figure 5.4: A simulated sorption isotherm of PW_1 pore at 25°C with an effective diameter of 0.95nm.

The sudden increase of relative density of the adsorbed water (point A in Fig. 5.4) indicates occurrence of capillary condensation. Figs. 5.5a and b are the snapshots of a 0.95nm PW_1 pore before and after capillary condensation. Water molecules almost fill the pore after capillary

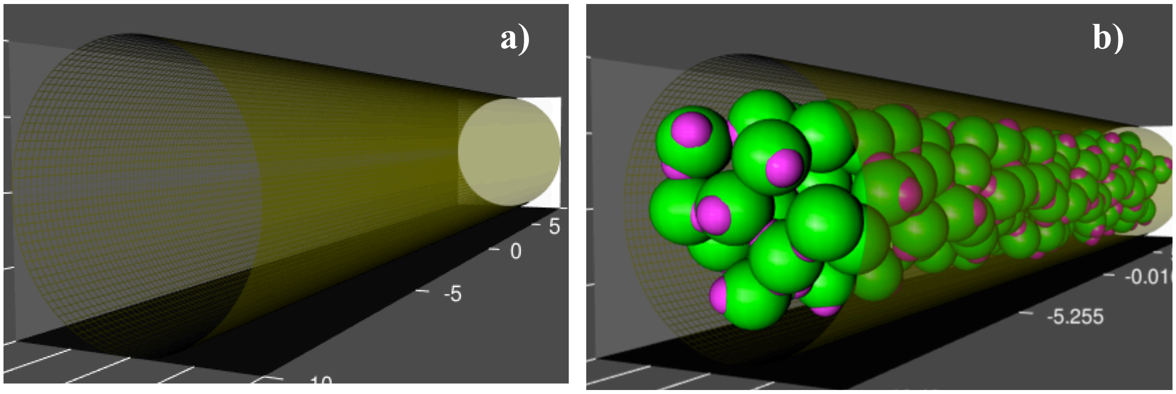

Figure 5.5: Snapshot of 0.95nm PW_1 pore. a) before capillary condensation; b) after capillary condensation.

condensation. The empty space in Fig. 5.5a is caused by the low the relative density of adsorbed water. The density is so low that the average number of water molecules inside the simulated pore is less than 1.

Similarly, the abrupt decrease of relative density of adsorbed water (point B in Fig. 5.4) indicates occurrence of capillary evaporation.

5.3.2 Origin of hysteresis

The origin of hysteresis in Fig. 5.4 seems to be associated with capillary condensation or evaporation. A direct way to examine the proposed hysteresis theory is observation of metastable states from the adsorption branch before point A, and/or metastable states from the desorption branch before point B. To illustrate this more clearly, a sketch of a theoretical sorption isotherm is given in Fig. 5.6, but replacing *H* with the chemical potential. The solid lines in Fig. 5.6 correspond to simulated points (e.g., points in Fig. 5.4); the dashed line EFG is where the vapor-liquid phase coexistence occurs; lines GA and FB correspond to metastable states. In order to find the coexistence line, it is necessary to simulate those unstable points between points A and B. These points usually present as a sigmoid curve like AS_vS_lB in Fig. 5.6.

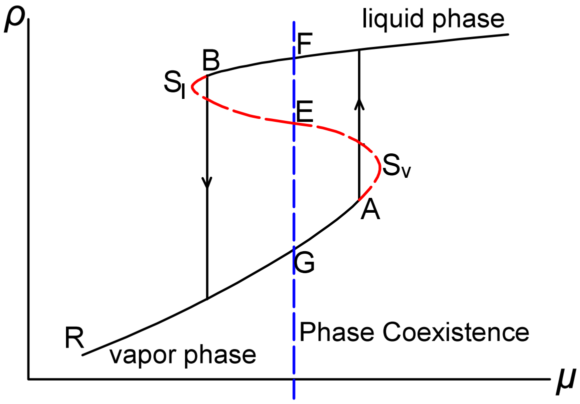

Figure 5.6: Sketch of a theoretical sorption isotherm with two limit spinodal points S_v and S_l. $\boldsymbol{\rho}$ represents the density of adsorbed water, and $\boldsymbol{\mu}$ represents chemical potential.

Afterwards, the grand thermodynamic potential density (Vishnyakov and Neimark 2001) can be calculated by

$$\frac{\Omega(\mu,\tau)}{V} = \frac{\Omega(\mu_r,\tau)}{V} - \int_{\mu_r}^{\mu} \rho(\mu,\tau) d\mu = -k_B \tau \rho(\mu,\tau) - \int_{\mu_r}^{\mu} \rho(\mu,\tau) d\mu \tag{5.7}$$

where μ (J) is chemical potential, ρ (kg m^{-3}) is the density of adsorbed water, τ (K) is temperature, V (m^{-3}) is the volume of the simulated pore, Ω (J) is the grand thermodynamic potential (Ω is defined as $F - \mu N$ where F (J) is Helmholtz free energy and N is number of adsorbed water), k_B is Boltzmann constant (1.38066×10^{-23} J K^{-1}), and $\Omega(\mu_r,\tau)$ is the grand potential of a reference state with a sufficiently small μ. It is known that at the phase coexistence point, the grand potential of the vapor phase and the liquid phase is the same. Geometrically, this means that in Fig. 5.6, the area of GS_vE equals that of ES_lF (Maxwell's rule).

The Gauge Cell method developed by Vishnyakov and Neimark (2001) was used to simulate those unstable points on a sorption isotherm. Fig. 5.7a shows the unstable points for the sorption isotherm in Fig. 5.4. The dashed line FG indicates the place where the coexistence of vapor and condensed water occurs. For the adsorption branch, all the points after G until the vapor-like spinodal S_v are in metastable states. Similarly, all the points before F until the liquid-like spoinodal

S_l are in metastable states. The result is further illustrated by calculated grand potentials (Fig. 5.7b). The coincidence of the grand potential of the vapor-like branch and liquid-like branch illustrates the phase coexistence points F and G. At any other chemical potential, lines with the lowest grand potential correspond to stable state; the dashed line with the highest grand potential corresponds to the unstable states; lines GS_v and FS_l with the second lowest grand potential correspond to metastable states. So far, it is clear that metastable states exist for both adsorption and desorption branches (lines GA and FB in Fig. 5.7a), and both contribute to hysteresis.

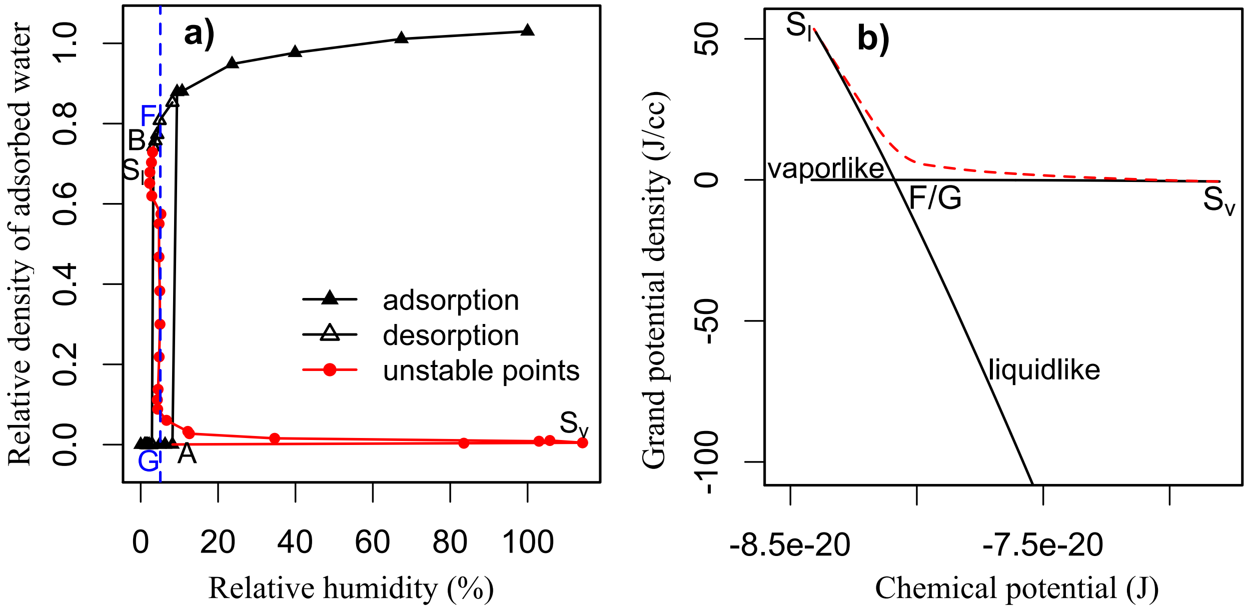

Figure 5.7: a) Simulated sorption isotherms of 0.95nm PW_1 pore at 25°C with unstable points simulated from the gauge cell method: the dashed blue line illustrates coexistence of vapor and condensed water; b) calculated grand potential density for sorption points in a).

Alternatively, an argument based on the general first order phase transition can be made to prove the existence of metastable states and their relationship to hysteresis. The large density differences and observed hysteresis are both signs of a first order phase transition. Since another characterization of first order phase transition is a latent heat (Kittel and Kroemer 1980), further calculation of energy change associated with capillary condensation and evaporation was proceeded. Applying the first law of thermodynamics and the ideal gas assumption for the vapor-like phase, the released heat from vapor during capillary condensation Q_{cond} (kcal/mol) is calculated as:

$$Q_{cond} = \Delta U - W = U_l - U_g - p\,\Delta V \approx U_l - U_g - p\,V_g \approx U_l - U_g - RT \tag{5.8}$$

where U_g (J) and U_l (J) are internal energy of water phases before and after condensation. Since at 25°C, $U_l \gg U_g$, Eq. (5.8) is further simplified as:

$$Q_{cond} \approx U_l - RT \tag{5.9}$$

U_l is approximated from the total interaction energy calculated in simulation. Likewise, the absorbed heat from adsorbed water during capillary evaporation Q_{evap} (kcal/mol) is calculated as:

$$Q_{evap} \approx -U_l + RT \tag{5.10}$$

It is known that the experimental heat of vaporization of water at 25°C is 10.51 kcal/mol. For the sorption isotherm in Fig. 5.4, the calculated Q_{cond} is -11.81 kcal/mol, and Q_{evap}, 11.50 kcal/mol. Hence, this computation shows that the energy change of water in capillary condensation and evaporation are very close to that of first-order phase transition from vapor to liquid water and vice-versa. Therefore, it can be concluded that first-order phase transition occurs in both adsorption and desorption. As a result, the existence of metastable states, like supersaturated vapor and liquid, in first-order phase transitions should explain the hysteresis here.

The modeled cell wall has an assembly of pores with different sizes. Therefore, the sorption isotherm of the gross cell wall could be obtained by the supposition of the sorption isotherm at each pore size. Figs. 5.8a and 5.8b present the simulated water sorption isotherms of PW_1 and PW_2 pores ranging from 0.63 to 2.2nm at 25°C.

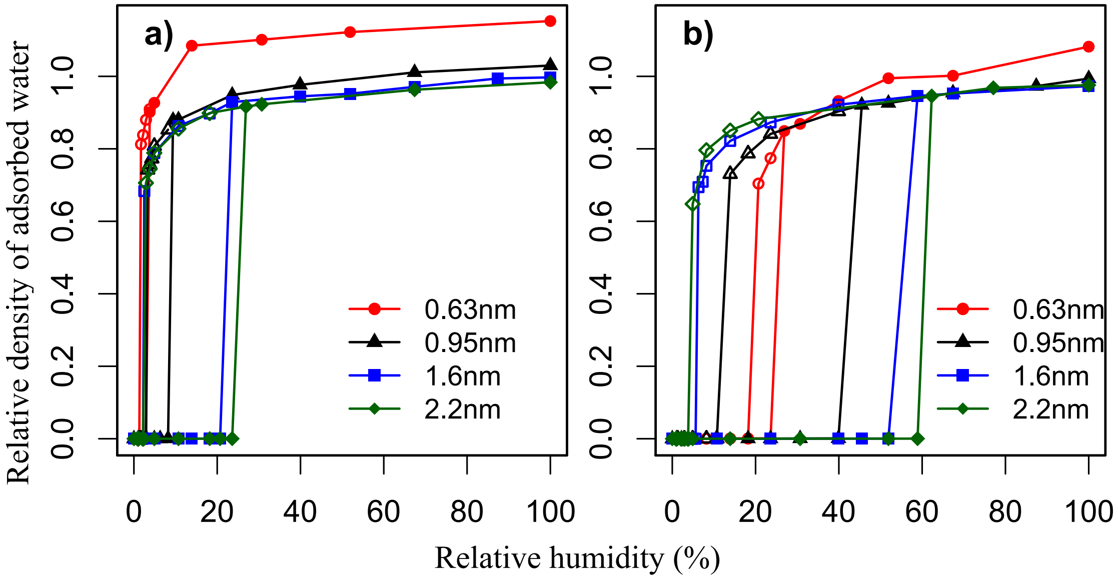

Figure 5.8: Simulated sorption isotherms of cell wall pores at 25°C with effective diameters of 0.63, 0.95, 1.6 and 2.2nm. a) PW_1 pores; b) PW_2 pores. Solid symbols, adsorption; open symbols, desorption.

Obviously, capillary condensation and hysteresis occurred for all the pores sizes and wall types of interest. The modeled cell wall pores are not able to swell and shrink. As a result, for different M ($<M_{fsp}$), a *PSD* has to be assumed and used as weights for the sorption isotherm at a specific pore size. By changing the weights, different shapes of hysteresis loops can be obtained. Because of infinite possibilities of the weights, only two characteristic examples were presented in Fig. 5.9 showing the gross sorption isotherm from superposition of sorption isotherms in Fig. 5.8 using equal and unequal weights. These sorption isotherms are quite rudimentary, but agree with general experimental trends. A much smoother curve can be expected when more single pore sizes are simulated. It is certain, however, no matter how the weights are adjusted, hysteresis always exists. This in turn, strongly indicates that hysteresis will take place at the macroscopic cell wall level and share the same origin.

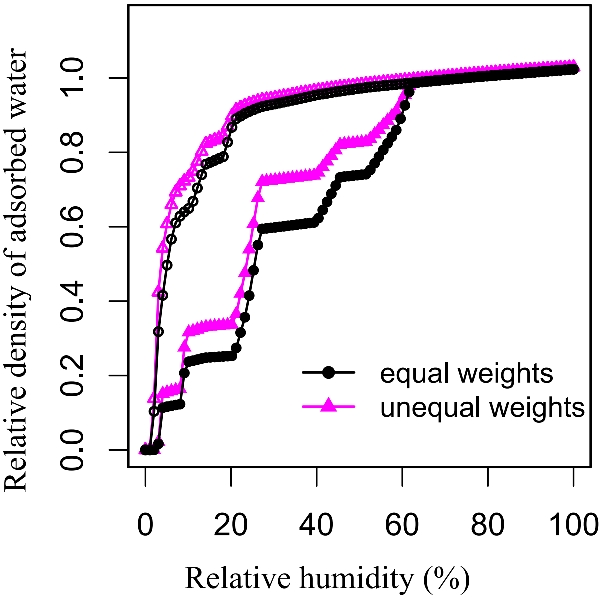

Figure 5.9: An example of sorption isotherms obtained by superposition of sorption isotherms in Fig. 5.8. Solid symbols, adsorption; open symbols, desorption.

By now, both simulation results and arguments have strongly supported the existence of metastable states in water sorption in woods and their contribution to hysteresis. Next, the discussion will focus on some interesting experimental observations that can be explained by this new theory.

5.3.3 Effect of pore size on hysteresis

For both PW_1 and PW_2 pores, Figs .5.8a and 5.8b demonstrate that the critical *H*, where capillary condensation happens, becomes larger with increased pore sizes, and the magnitude of the hysteresis loop also increases. These simulated trends are consistent with experimental findings from sorption isotherms of nanoporous silica or activated carbon materials and wood as described in chapter 2.

With the increase of the pore size, the interaction between wall and water molecules become weaker as shown from the wall potential depth in Fig. 5.10a for PW_1, and Fig. 5.10b,

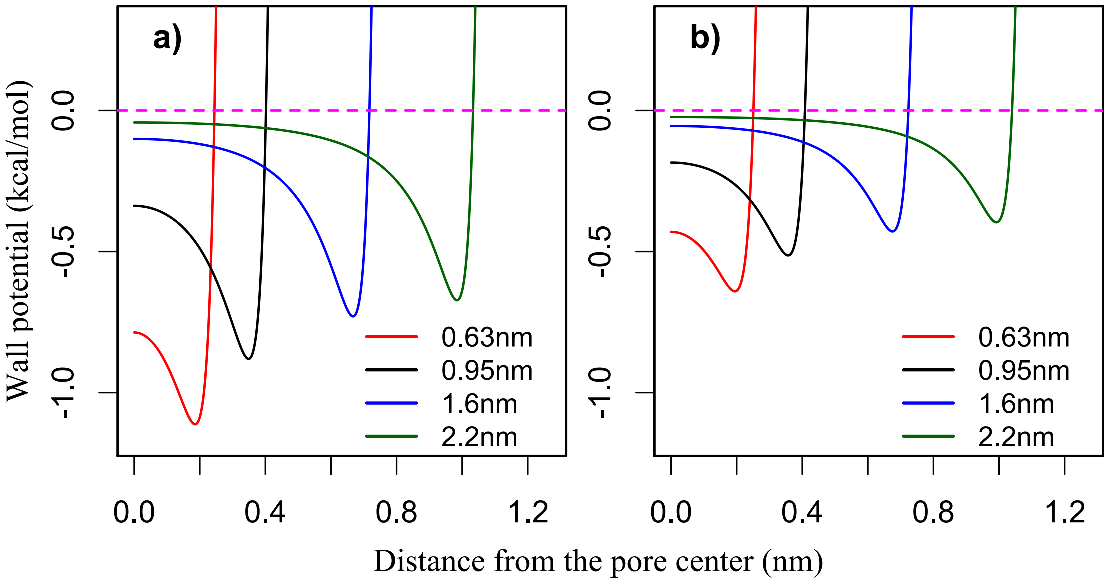

Figure 5.10: Water–wall potential of pores with effective diameters of 0.63, 0.95, 1.6 and 2.2nm. a) PW_1 pores; b) PW_2 pores.

PW_2 pores. Figs. 5.11a and 5.11b show partial adsorption isotherms of these pores before capillary condensation in expanded scales. Together with Fig. 5.10, it is apparent that the pore walls with weaker wall-water interaction adsorb water at the same *H*. It appears that the weaker interaction stabilizes the metastable states of adsorbed vapor-like water, and that also delays capillary condensation. Both indicate that more metastable states exist before capillary condensation. According to the developed hypothesis that hysteresis is caused by the existence of metastable states, more metastable states will result in additional hysteresis.

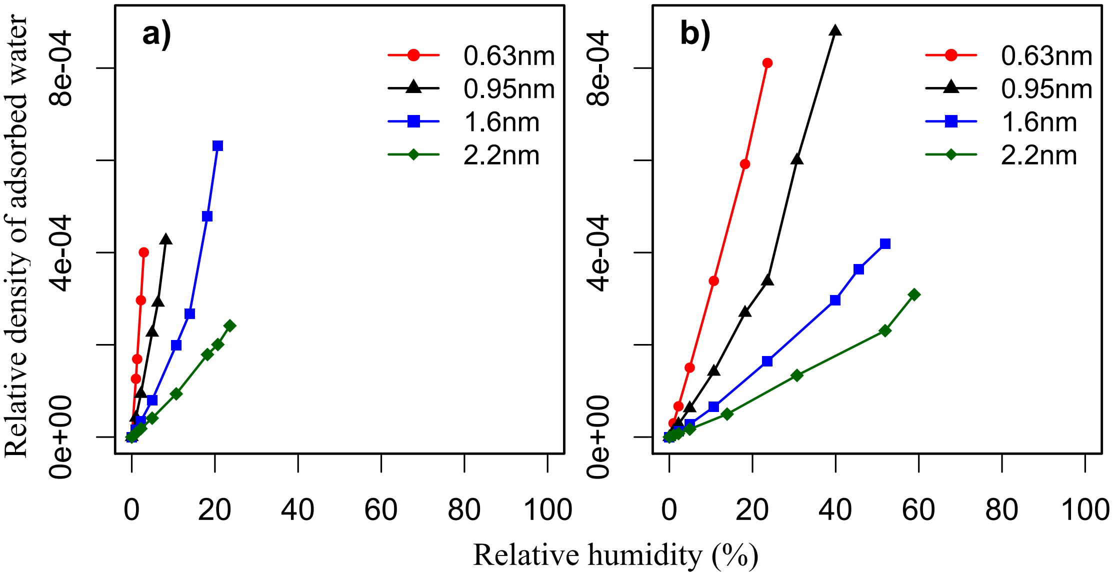

Figure 5.11: Partial adsorption isotherms before capillary condensation of pores with effective diameters of 0.63, 0.95, 1.6 and 2.2nm. a) PW_1 pores; b) PW_2 pores.

5.3.4 Effect of chemical composition on hysteresis

Another interesting experimental finding is lignin's larger contribution to hysteresis magnitude compared to other cell wall polymers. Previous studies have reported that the hysteresis magnitude of isolated lignin is larger than that of isolated cellulose, holocellulose, and native wood samples (Chirkova et al. 2006, Christensen and Kelsey 1958). By investigating a series of natural fibers, Hill et al. (2009) also found that a larger hysteresis loop was related to high lignin content in those fibers.

Comparing the simulated sorption isotherms of PW_1 and PW_2 pores (Fig. 5.8a vs. Fig. 5.8b), the magnitude of hysteresis loops of PW_2 pores are much larger than that of PW_1 pores at all pore sizes of interest. By revisiting the cell wall model, PW_2 represents the pore wall associated with lignin, and PW_1, polysaccharides. It is thus evident that the simulation results support lignin's larger contribution to hysteresis magnitude.

Fig. 5.12 compares adsorption isotherms of two types of 0.95nm pores in Fig. 5.8 before capillary condensation. Much less water is adsorbed on the PW_2 pore at the same *H*, and the critical *H*, where capillary condensation happens, is shifted towards a much larger value. It appears that lignin stabilizes the metastable states of adsorbed vapor-like water, whereas, more intensive hydroxyl groups in polysaccharides disturb the metastable states. However, the critical *H*, where capillary evaporation happens, is not significantly affected (Fig. 5.8). This is probably due to similar roles of lignin and polysaccharides in stabilizing adsorbed liquid-like water. Since hysteresis is caused by the presence of metastable states as per our proposed theory, more such states brought by lignin in the adsorption branch contribute to overall larger hysteresis loops.

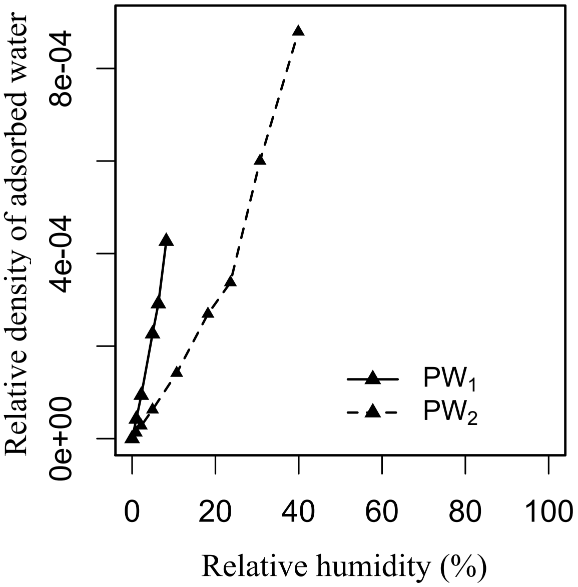

Figure 5.12: Partial adsorption isotherms of 0.95nm pores in Fig. 5.8 before capillary condensation.

5.3.5 Simulated sorption isotherms at 40°C

Figs. 5.13a and 5.13b demonstrate simulated water sorption isotherms of PW_1 and PW_2 pores with sizes in the range of 0.63 to 2.2nm at 40°C. Overall, the trends observed at 25°C, also hold at 40°C. Capillary condensation occurs at all pore sizes of interest and hysteresis is highly affected by pore size and pore wall type. In addition, the temperature tends to cause water condensation at higher *H*s, and the hysteresis loops become narrower. These trends are consistent with the sorption isotherm data for D-fir, aspen and WRC at 25 and 40°C as described in chapter 3. The reduced hysteresis magnitude might be attributed to larger thermal fluctuations at the higher temperature, which can destabilize the metastable states more easily. Fewer metastable states will correspond to smaller hysteresis as per the current proposed theory. Interestingly, for 0.63nm PW_1 pore (Fig. 5.13a), hysteresis has disappeared. Further simulations on higher temperatures reveal that a critical

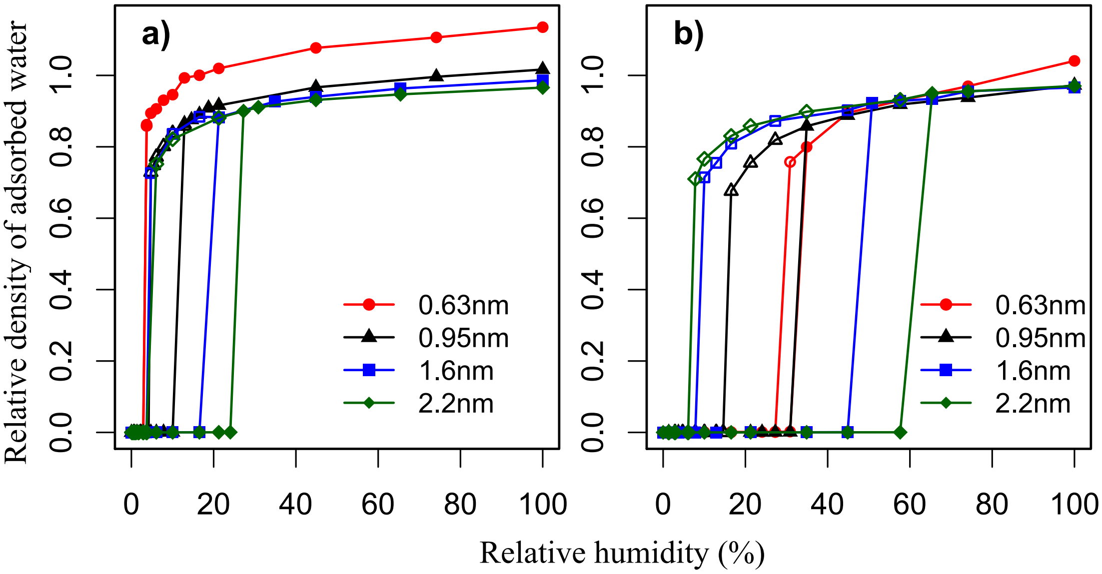

Figure 5.13: Simulated sorption isotherms of cell wall pores at 40°C with effective diameters of 0.63, 0.95, 1.6 and 2.2nm. a) PW_1 pores; b) PW_2 pores. Solid symbols, adsorption; open symbols, desorption.

temperature, where hysteresis disappears, can be found for each pore size and wall type, and eventually, a critical temperature for wood where no hysteresis exists.

5.3.6 Sorption mechanism: capillary condensation vs. layering and clustering theories

Layering and clustering theories are two major theories accepted at low to medium *H* regions, whereas capillary condensation was believed to take place only at very high *H* regions (>70%) (Avramidis1997, Walker 2006). The support of the layering theory (like BET) partly comes from the S-shape of experimental sorption isotherms, which belong to Type II ones, and usually are well described by the multilayer sorption theory. However, the foundation of BET is a nonporous surface, contrary to the porous nature of wood at nanoscale. Another supporting evidence comes from a good match between experimental data and BET fitted curves. Simpson's (1980) investigation on various mathematical sorption models has suggested good fitting of most models regardless of the underling mechanisms. However, unsatisfactory predictions of heat of sorption from those models were reported. Additionally, the role of hydroxyl groups in the sorption process has been challenged (Rautkari et al. 2013). In view of all that unbiguity in the litterature, one may expect an altervative sorption mechanism.

Simulation results in this chapter show that capillary condensation may take place at the low *H* region of 0 – 30% for cell wall pores associated with polysaccharides (Fig. 5.8a), and the medium *H* region of 20% – 60% for pores associated with lignin (Fig. 5.8b). It suggests dominance of capillary condensation in the entire *H* region. Furthermore, before capillary condensation, there is no sign of formation of a monolayer or clusters (Fig. 5.5a). To better understand this, the conditions at which a monolayer or cluster forms were explored by adjusting the energy strength of the sorption sites and interaction energy between the wall and water molecules in the simulations.

Fig. 5.14 demonstrates clusters formed on a simulated 0.95 nm PW_2 pore at *H* of 1.31% with an average sorption site energy strengthened to -18.03kcal/mol from -4.51kcal/mol. All the sorption sites (blue balls in Fig. 5.14) absorb at least one water molecule, and most of them adsorb 3 to 4 water molecules to form water clusters. In fact, if the sorption site energy in wood can be as strong as twice the water-water interaction, formation of water clusters is a strong possibility. However, these clusters can only exist under very low *H*s (<2%) for as *H* increases, capillary condensation takes place. As cell walls swell with the increase of *H*, it is possible that more pores are created at medium to high *H* levels, say, >30%. Should this occur, the adsorption process would be initiated by formation of water clusters, but eventually would be dominated by capillary condensation when reaching equilibrium.

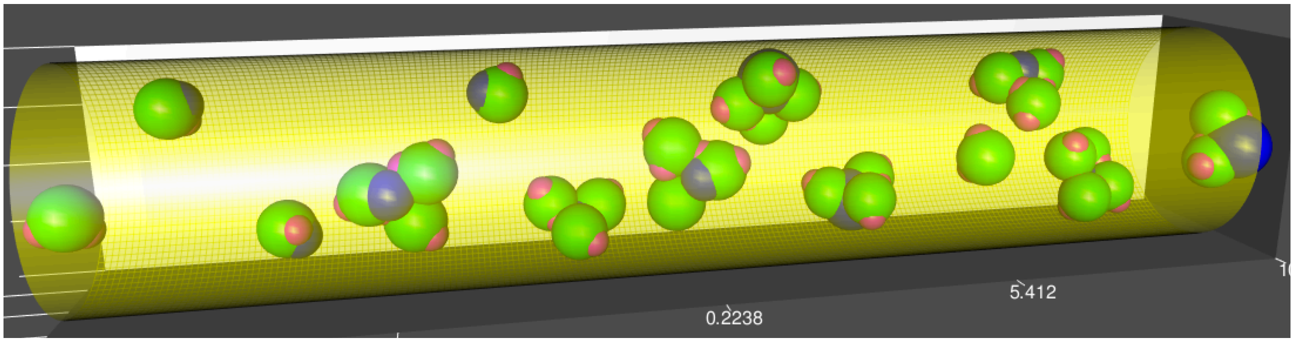

Figure 5.14: A snapshot showing simulated clusters formed on a 0.95nm PW_2 pore with strengthened sorption site energy. Each green ball with attached two magenta balls represents one water molecule, and blue balls represent sorption sites.

Fig. 5.15 presents a simulated monolayer formed on a 1.6nm pore at *H* of 0.0005% when LJ parameter ε/k_B of wall-water interaction is increased to 874.35K from 58.29K. The sorption sites are removed to preclude additional influence from them.

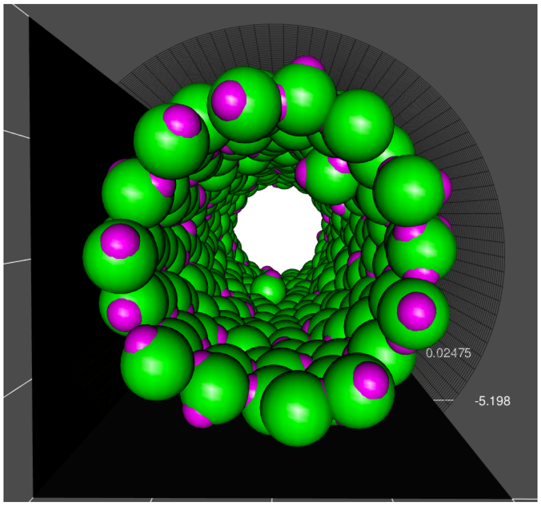

Figure 5.15: A snapshot showing a monolayer formed on a1.6nm pore with strengthened wall-water interaction and no sorption sites. Each green ball with attached two magenta balls represents one water molecule.

The interaction energy between water and the pore wall has been strengthened to an extent that does not seem to be possible for real wood-water systems. Furthermore, even if a material is very hydrophilic, like the simulated case here, the water monolayer forms at an extremely low *H*. One can almost presume the existence of a water monolayer before the material is even exposed to a humid environment.

The unusual sorption behavior illustrated in the aforementioned simulations is probably because of the strong interactions among water molecules due to the hydrogen bonding. The normal strong interactions between adsorbates and sorbents become relatively weak, so under this circumstance, it seems reasonable to expect some alternative sorption mechanism like capillary condensation to take control of the process. Earlier nuclear magnetic resonance (NMR) and differential scanning calorimeter (DSC) investigations both indicated two types of bound water: one is less mobile than the other (Walker 2006). The less mobile water is often assigned to water adsorbed on sorption sites or the monolayer water. The new sorption mechanism offers another possible interpretation to these two types of bound water. The less mobile bound water can be assigned to water in smaller pores, and more mobile one, water in larger pores.

5.4 Conclusion

The grand canonical Monte Carlo has been satisfactorily applied in a simplified wood-water system to simulate the sorption isotherms and hysteresis at 25 and 40°C. Hysteresis is well explained by the existence of metastable states associated with capillary condensation and evaporation of water in cell walls. Unlike capillary evaporation, capillary condensation occurs in the wide hygroscopic range and is sensitive to wall-water interaction, pore size and temperature. The simulations suggest that the weaker wall-water interaction, brought in by either larger pore size or less hydrophilic characteristic of lignin, stabilizes the metastable states before capillary condensation, thus contributing to larger hysteresis observed in earlier experiments. Likewise, less metastable states at the higher temperature due to larger thermal fluctuations can explain the reduced hysteresis magnitude. Lastly, the simulation casts doubt on the layering and clustering sorption theories, and instead it provides an alternative sorption mechanism driven by capillary condensation.

Chapter 6: Physical Model Parameters Investigations

6.1 Introduction

In Chapter 5, the water sorption isotherm of wood and related hysteresis were simulated using the molecular simulation. However, in the simplified wood-water system, the values of several model input parameters are not certain. These uncertainties are challenging the generality of conclusions from the simulated sorption isotherms, especially the occurrence of capillary condensation used for explaining hysteresis.

In this chapter, a detailed study is conducted on two most uncertain model parameters, namely, wall-water interaction strength and number of sorption sites, as well as, on justification of the cell wall pore shape.

6.2 Methodology

To minimize the simulation time, the investigations were focused on intermediate cell wall pore size of 0.95nm and room temperature of 25°C.

6.2.1 Wall-water interaction strength

Further the two types of pore walls, PW_1 and PW_2 in chapter 5, six additional types labeled as PW_3 – PW_8 were considered here. PW_3 and PW_4 are comprised of pure oxygen and carbon atoms, respectively. PW_5 to PW_7 are modified PW_1 with different extent of enhancement of wall-water interaction strength, whereas PW_8 are modified PW_2 with decreased interaction strength. Table 6.1 lists the LJ potential parameters used in the simulation of the eight aforementioned walls. To avoid the complications from hydrogen bonding, energy pits were not added on these walls.

Table 6.1: Summary of LJ potential parameters of 8 types of pore walls and water.

Interaction	LJ Potential Parameters	
	ε/k_B (K)	σ (Å)
PW_1-water	58.29	3.281
PW_2-water	37.60	3.190
PW_3-water	78.23	3.166
PW_4-water	28	3.4
PW_5-water	87.435	3.281
PW_6-water	174.87	3.281
PW_7-water	291.45	3.281
PW_8-water	7.52	3.190

6.2.2 Number of sorption sites

The sorption sites were modeled as energy pits attached on pore walls as in chapter 5. The number of these sites could easily be changed by varying parameter *nps_l*. Another parameter *nps_c* was kept constant considering the limited perimeter of a 0.95nm pore. Table 6.2 provides the assessed values of *nps_l*.

Table 6.2: Summary of number of energy pits on simulated cylindrical pore walls.

PW_1		PW_2	
nps_c	*nps_l*	*nps_c*	*nps_l*
3	12	3	4
3	16	3	6
3	8	3	2

6.2.3 Cell wall pore shape

6.2.3.1 Slit pore model

Similar to the cylindrical pore walls, the slit pore walls were comprised of evenly distributed LJ atoms. The pore had infinite length in the y-z plane and width *w* in the *x* direction (Fig. 6.1).

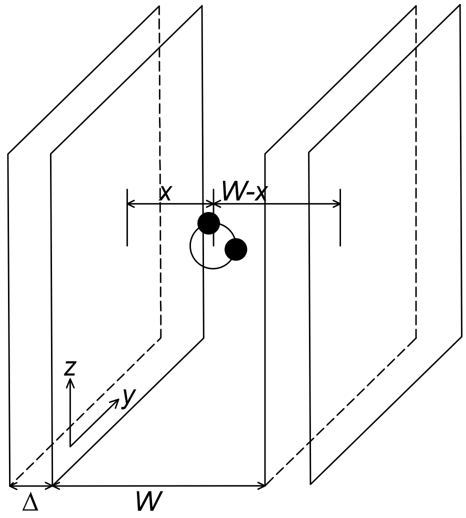

Figure 6.1: Schematic of a slit pore with one water molecule inside.

The interaction energy between one water molecule and the pore wall can be calculated from the Steele 10-4-3 potential (Steele 1974):

$$U(x) = U_{left-wall}(x) + U_{right-wall}(x) = 2\pi\rho_s\varepsilon_{sf}{\sigma_{sf}}^2\Delta\left[\frac{2}{5}\left(\frac{\sigma_{sf}}{x}\right)^{10} - \left(\frac{\sigma_{sf}}{x}\right)^4 - \frac{{\sigma_{sf}}^4}{3\Delta(x+0.61\Delta)^3}\right] +$$

$$2\pi\rho_s\varepsilon_{sf}{\sigma_{sf}}^2\Delta\left[\frac{2}{5}\left(\frac{\sigma_{sf}}{W-x}\right)^{10} - \left(\frac{\sigma_{sf}}{W-x}\right)^4 - \frac{{\sigma_{sf}}^4}{3\Delta(\mathrm{W}-x+0.61\Delta)^3}\right] \quad (6.1)$$

where x (nm) is the distance of the water molecule from the left wall; W (nm) is the width of the pore; Δ (nm) is the distance of two neighboring layers of the wall; ε_{sf} (J) and σ_{sf} (nm) are LJ parameters of interaction between wall atoms and water molecules; ρ_s (kg m^{-3}) is the density of the wall atoms. $\Delta = 0.335$nm is taken from the activated carbon walls (Müller et al. 1996).

6.2.3.2 Sphere pore model

The sphere pore walls are also composed of evenly distributed LJ atoms (Fig. 6.2).

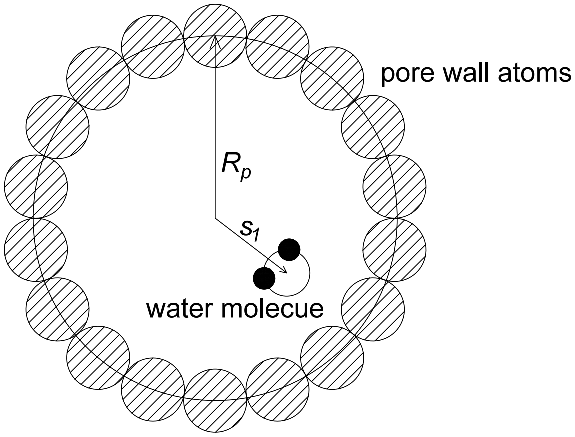

Figure 6.2: Schematic of a sphere pore with one water molecule inside.

Applying Eq. (5.3) and integrating over the sphere surface, the pore–water interaction energy U (Kaminsky et al. 1994) is calculated as:

$$U(s_1) = 16\pi\varepsilon_{sf}{\sigma_{sf}}^2\rho_A\left[\left(\frac{\sigma_{sf}}{R_p}\right)^{10}\frac{1+12\frac{{s_1}^2}{{R_p}^2}+25.2(\frac{{s_1}^2}{{R_p}^2})^2+12(\frac{{s_1}^2}{{R_p}^2})^3+(\frac{{s_1}^2}{{R_p}^2})^4}{(1-\frac{x^2}{{R_p}^2})^{10}}-\left(\frac{\sigma_{sf}}{R_p}\right)^4\frac{1+\frac{{s_1}^2}{{R_p}^2}}{(1-\frac{{s_1}^2}{{R_p}^2})^4}\right] \tag{6.2}$$

where s_1 (nm)is the distance of the water molecule from the pore center; R_p (nm) is the radius of the sphere; ρ_A (m-^{2}) is the density of the atoms per unit area of the pore wall, which can be approximated from the number density of wall atoms N_s in chapter 5.

6.3 Results and Discussion

6.3.1 The effect of wall-water interaction strength on simulated sorption isotherms

Figs. 6.3a and 6.3b present the simulated sorption isotherms for PW_1 to PW_8 pores. As the wall-water interaction becomes stronger, water condenses at a lower H and the hysteresis loop becomes narrower. When the interaction becomes very weak as in PW_4 and PW_8 (Fig. 6.3b), water cannot condense on pore walls. The maximum density of condensed water was found proportional to the wall-water interaction strength. In most cases, the condensed water density was lower than bulk water density of 1.0g/cc. However, the strong interaction could bring the water density closer to or even higher than 1.0g/cc as in the case of PW_6 and PW_7 shown in Fig. 6.3a.

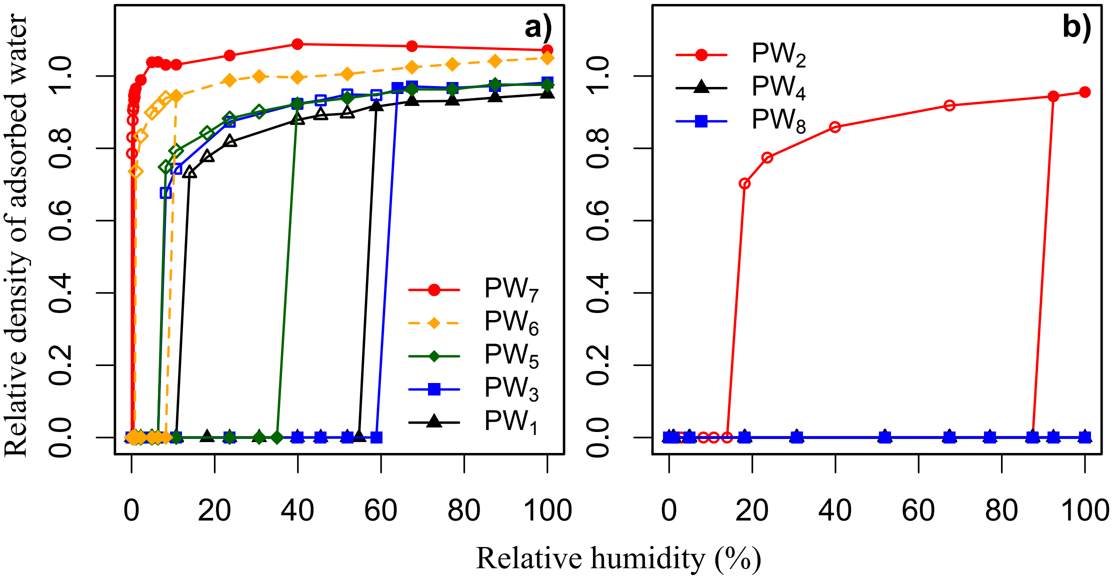

Figure 6.3: Simulated sorption isotherms of 0.95 nm cell wall pores at 25°C. a) PW_1, PW_3, PW_5, PW_6 and PW_7; b) PW_2, PW_4 and PW_8. Solid symbols, adsorption; open symbols, desorption.

6.3.2 The effect of number of sorption sites on simulated sorption isotherms

Figs. 6.4a and 6.4b demonstrate how the number of sorption sites affects the simulated sorption isotherms. For both PW_1 and PW_2 pores, more sorption sites cause water to condense at lower *H* and the hysteresis loop becomes narrower. In addition, PW_2 is more sensitive to the variation of the number of sorption sites. Like the effect of wall-water interaction, more sorption sites produce denser adsorbed water.

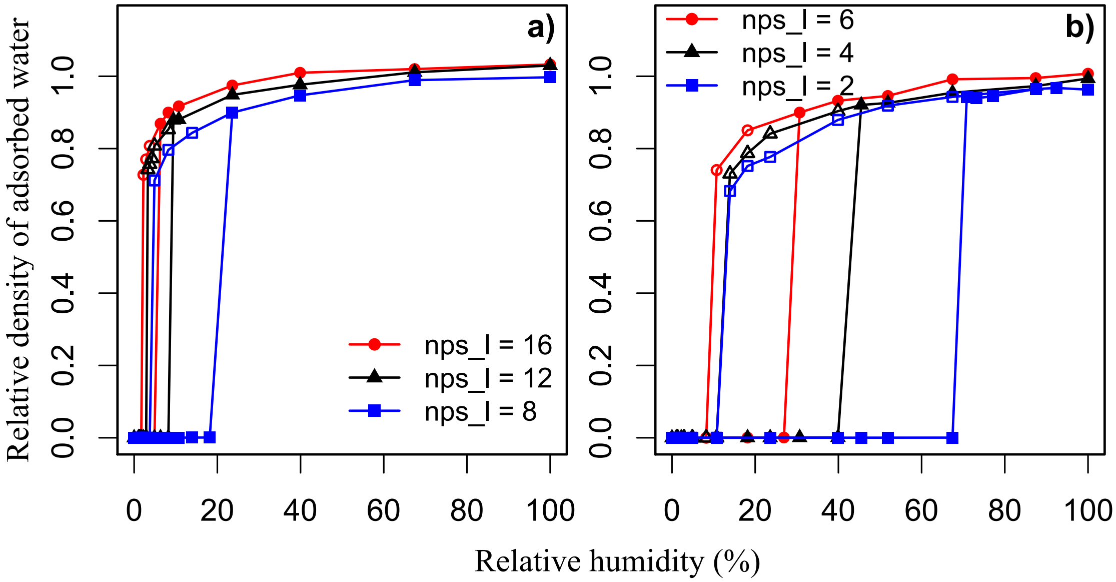

Figure 6.4: Simulated sorption isotherms of 0.95 nm cell walls at 25°C with different sorption sites numbers. a) PW_1 pores; b) PW_2 pores. Solid symbols, adsorption; open symbols, desorption.

6.3.3 Interaction of model parameters

The trends given by different wall-water interaction strength and sorption site numbers are similar, and they also resemble the trend shown by different cell wall pore sizes as discussed in chapter 5. In general, the above three model parameters — pore size, wall-water interaction strength and number of sorption sites — largely affect the simulated sorption isotherms. Furthermore, it is very likely that these parameters are interacting with each other.

In a typical plot of simulated sorption isotherms (Fig. 6.5), there are two essential critical points. One is point A where capillary condensation occurs, and another is point B where capillary evaporation occurs. By letting H_u and H_l be the H at these two points then, the hysteresis loop width can be denoted as $\Delta H = H_u - H_l$.

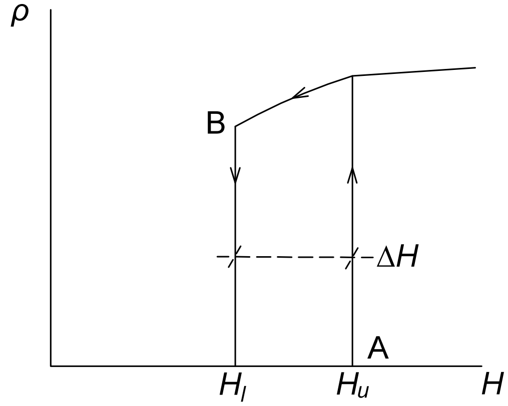

Figure 6.5: Plot of a simulated sorption isotherm: ρ denotes the relative density of adsorbed water.

By pooling all simulated data from varied model parameters (Table B.1 in Appendix), a statistical model was employed to analyze how the parameters affect H_u, H_l and ΔH and how they interact with each other. In chapter 5, the failure of Kelvin's equation in predicting H_u was argued, however, the form of this equation provides an insight regarding the interactions among the parameters. In Eq. (5.1), by replacing γ with ε_{sf} and then modifying it by the number of sorption sites n_{HB} ($n_{HB} = nps\_c \times nps\_l$), two candidate variables, $\frac{\varepsilon_{sf}}{r_p}$ and $\frac{n_{HB}}{r_p}$, could be identified for statistical modeling. Eqs. (6.3.1) to (6.3.3) are multiple linear regression models used to fit the data in Table B.1.

$$lnH_u = b_0 + b_1 \frac{\varepsilon_{sf}}{r_p} + b_2 \frac{n_{HB}}{r_p} \tag{6.3.1}$$

$$lnH_l = b_0 + b_1 \frac{\varepsilon_{sf}}{r_p} + b_2 \frac{n_{HB}}{r_p} \tag{6.3.2}$$

$$ln\Delta H = b_0 + b_1 \frac{\varepsilon_{sf}}{r_p} + b_2 \frac{n_{HB}}{r_p} \tag{6.3.3}$$

Reduced units (refer to Appendix B.2) were used for normalizing the fitted coefficients in the above models. Table 6.3 lists fitted coefficients in Eqs. (6.3.1) – (6.3.3) and corresponding adjusted

R^2. The large adjusted R^2 values indicates good fitting for H_u and ΔH, but not so satisfactory for H_l. Replacing r_p in Eq. (6.3.2) with $\sqrt{r_p}$, the adjusted R^2 could be improved to 0.780 from 0.700.

Table 6.3: Fitted coefficient values in Eq. (6.3.1) – (6.3.3).

	b_0	b_1	b_2	Adjusted R^2
H_u	5.156	-2.099	-0.077	0.946
H_l	3.042	-2.072	-0.044	0.700
H_l*	3.542	-2.018	-0.062	0.782
ΔH	5.102	-2.200	-0.097	0.944

Note: for H_l*, r_p in Eq. (6.3.2) is replaced by $\sqrt{r_p}$.

Apart from illustrating the interaction of r_p, ε_{sf} and n_{HB}, the fitted statistical models are useful in predicting sorption isotherms without long-time molecular simulation running in the future when more accurate parameter values are available.

6.3.4 Cell wall pore shape

Figs. 6.6a and 6.6b present simulated sorption isotherms of 0.95nm PW_1 and PW_2 pores with cylindrical, slit and sphere pore shapes at 25°C. To focus more on the effect of pore shapes, the HB number for all pores here was set to be zero. The simulated isotherms from the cylindrical and slit pore shapes were similar to each other; the weak wall-water interaction from PW_2 pushed H_u to a larger value and the hysteresis loop became larger. However, the sphere pores behaved differently, i.e. water could condense in PW_1 but not in PW_2 and the condensed water in PW_1 had a much smaller density (around 0.6 g/cc). Since water cannot condense in PW_4 and PW_8

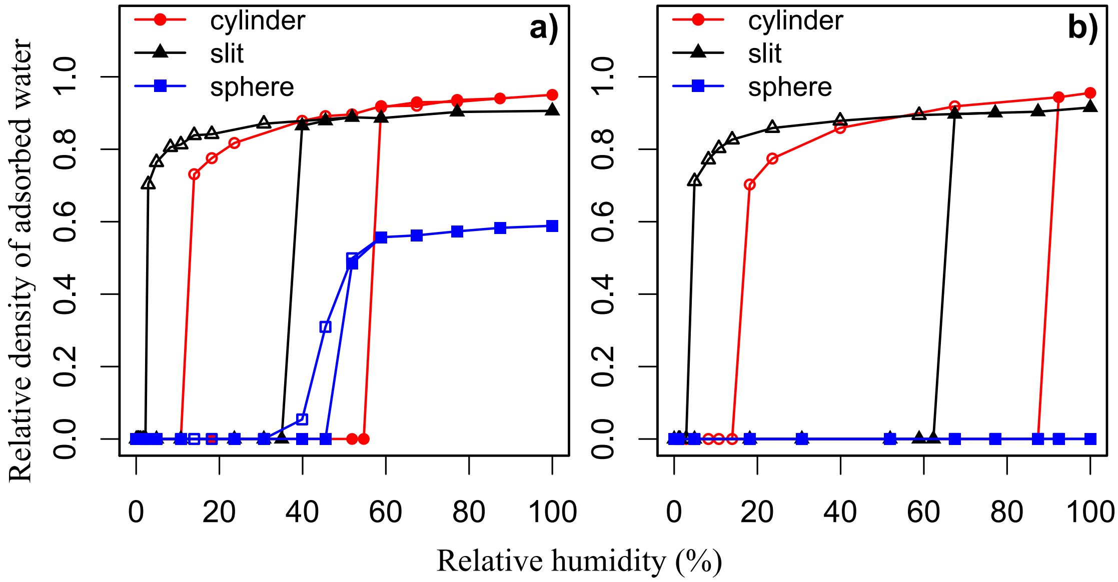

Figure 6.6: Simulated sorption isotherms of 0.95nm cell wall pores with cylindrical, slit and sphere pore shapes at 25°C. a) PW_1 pores; b) PW_2 pores. Solid symbols, adsorption; open symbols, desorption.

cylindrical pores (Fig. 6.3b) because of the very weak wall-water interaction, initially it was assumed that this weak interaction might happen in sphere pores too. Nevertheless, calculated wall potentials from the three pore walls revealed that the sphere pore wall has the strongest wall-water potential (the deepest energy well in Figs. 6.7a and 6.7b).

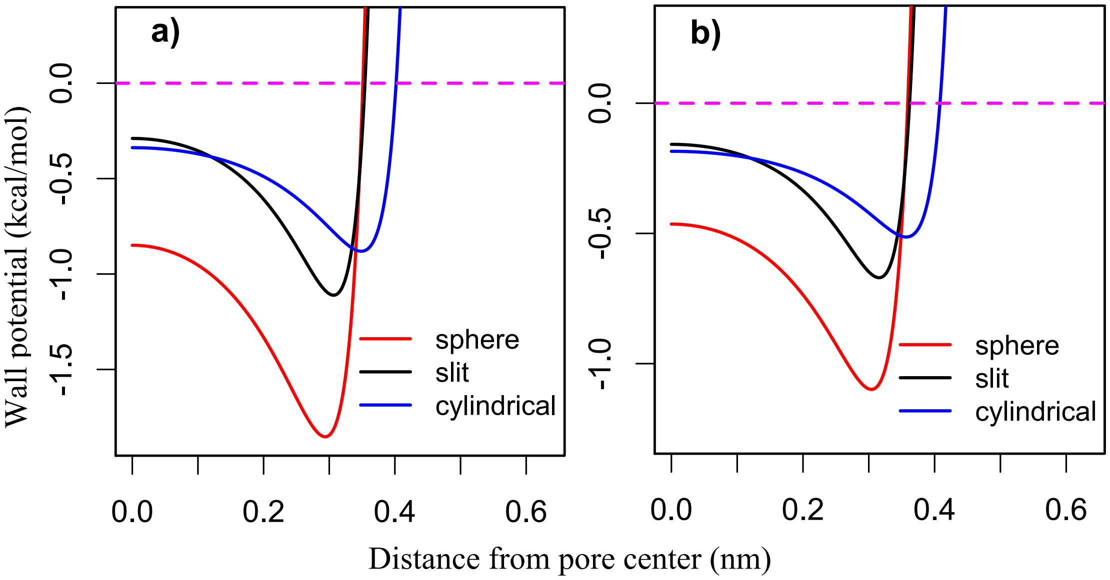

Figure 6.7: Wall potentials of pores with cylindrical, slit and sphere pore shapes. a) PW_1 pores; b) PW_2 pores.

Figs. 6.8a – 6.8c are snapshots of 0.95nm PW_1 cylindrical, slit and sphere pores filled with condensed water. They provide some insight of how different pore shapes restrict condensed water structure geometrically. When water is restricted one dimensionally (slit pore) and two dimensionally (cylindrical pores) by the pore, the integrity of liquid water structure is not significantly disturbed. However, when water is restricted down to 0.95nm in three dimensions by the sphere pore, only water clusters with an average size of 10 could be formed (Fig. 6.8c). Therefore, the hydrogen-bonding network in normal bulk liquid water was hardly maintained in confined water clusters. To further examine possibly denser adsorbed water in sphere pores, 6 sorption sites were added to the simulated pore in Fig. 6c. It turned out that the average adsorbed water density was increased to 0.691g/cc from 0.588g/cc. Fig. 6.8d shows how hydrogen bonding between water and pore surface shaped a larger water cluster composed of 14 molecules.

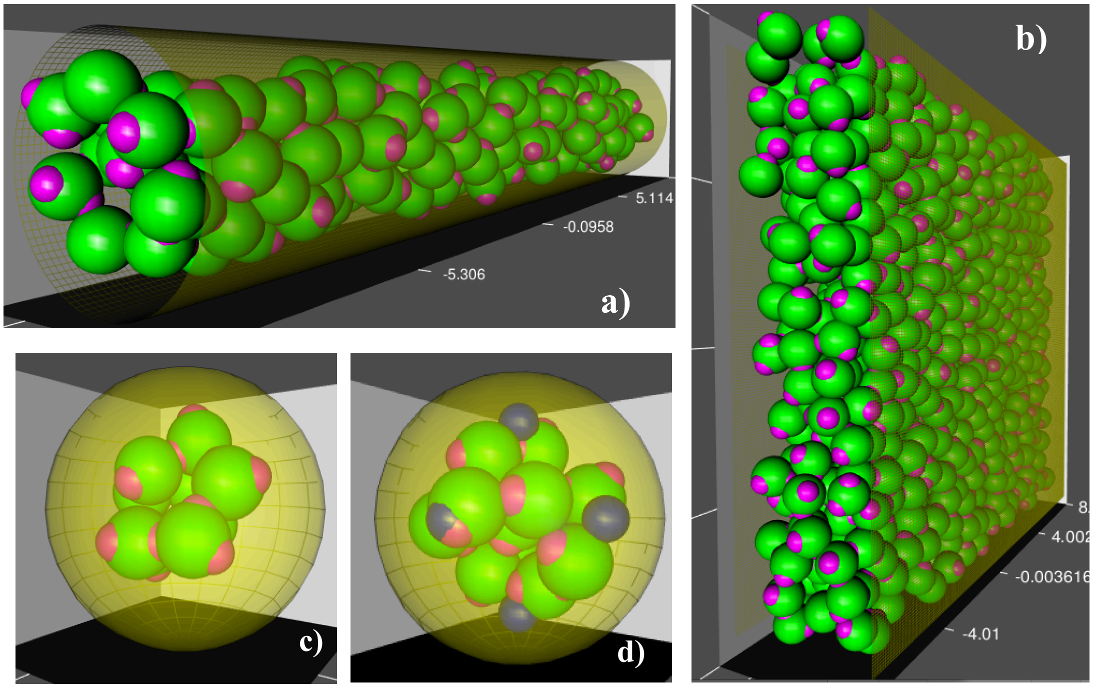

Figure 6.8: Snapshots of 0.95nm PW_1 pores filled with adsorbed water. a) cylindrical pore; b) slit pore; c) sphere pore with a water cluster composed of 9 molecules; d) sphere pore with a water cluster composed of 14 molecules. The blue spheres indicate the position of sorption sites.

6.3.5 Density of adsorbed water

The density of the adsorbed water in cell walls at M_{fsp} was estimated to be 1.017 g/cc from pycnometric measurements (Skaar 1972). The maximum adsorbed water density from simulated cylindrical and slit pores matched that 1.017 g/cc number well, but not in the case of sphere pores. If sphere pores dominated the cell walls, then the simulated water density at M_{fsp} would contradict the experimental value. Thus, from the density point of view, cell wall pores are more likely to be cylindrical and slit shapes. In general, the shape of cell wall pores is not likely to be so regular like the simulated cases here, but at least the simulation results suggest that these pores are not likely to be restricted to a few nanometers in three dimensions. If the cell wall polymers are organized along the direction of microfibrils as some researchers argued (Salmén 2004, Stevanic and Salmén

2009, Salmen et al. 2011), it is very likely that small voids in polymer structures connect with each other in that direction and form "infinite" long pores.

The density of adsorbed water at different *M* is also of interest. The simulations indicate increased adsorbed water density with increased *H*. Since higher *H* corresponds to higher *M*, it is obvious that the adsorbed water will be denser at elevated *M*s. However, this result did not agree with the one reported by Stamm and Seborg (1935). In fact, Stamm and Seborg made an error in calculating the compression of adsorbed water from the pycnometer measurement data. They ignored the volume of pores that initially existed in dried cell walls. Table 6.4 gives their calculated values of compression of adsorbed water. Translating "compression" into "density", the density of adsorbed water (column 3 in Table 6.4) was obtained.

Table 6.4: Density of adsorbed water at different *M*s from Stamm and Seborg (1935) sitka spruce data and corrected values.

M (%)	Compression of adsorbed water (cc/g dry material)	Density of adsorbed water (g/cc)	Corrected compression of adsorbed water (cc/g dry material)	Corrected density of adsorbed water (g/cc)
0.7	0.0045	2.800	-0.0255	0.215
2.5	0.0117	1.880	-0.0183	0.577
4.8	0.0183	1.616	-0.0117	0.804
10.6	0.0267	1.337	-0.0033	0.970
12.5	0.0288	1.299	-0.0012	0.990
20	0.0325	1.194	0.0025	1.013
23	0.0333	1.169	0.0033	1.015
30	0.0340	1.128	0.0040	1.014

These values are obviously too high for water under the ambient pressure and the room temperature. Furthermore, when $M = 30\%$, approaching M_{fsp}, the density 1.128g/cc is much higher than the generally accepted value 1.017g/cc (Skaar 1972). Assuming a general 0.03cc pore volume per gram dried cell walls, the corrected compression and density values were calculated (columns 4 and 5 in Table 6.4). The corrected density of adsorbed water at $M = 30\%$ is more reasonable. It has to be pointed out that in the above calculation, the filling of initial pores within dried cell walls was oversimplified. It was assumed that all initial pores were fully filled by water once the cell walls were exposed to humid environments. It is possible that those initial pores are only partly filled with water at low Ms. Therefore, the corrected density values at $M = 0.7\%$, 2.5% and 4.8% might not accurate. Considering the aforementioned analysis, the trend between M and density agrees with the simulated trend well.

6.4 Conclusion

Three variables, namely, H_u, H_l and ΔH were defined to characterize the critical properties of the simulated sorption isotherms. These isotherms are sensitive to model input parameters, i.e., pore size, wall-water interaction strength, number of sorption sites and pore sizes. By considering the interactions of these parameters, statistical models were developed to predict the H_u, H_l and ΔH. These models should be useful in predicting the simulated sorption isotherms without long-time computation in the future when more accurate parameter values are available.

In addition to cylindrical pores, slit and sphere pores were discussed. The simulated isotherms from sphere pores present a very low condensed water density of around 0.6 g/cc. This low density can be attributed to the three-dimensional geometric restriction imposed by the sphere wall. Considering the adsorbed water density, the cell wall pores are more likely to be slit or cylindrical.

A general conclusion from this parameter and pore shape investigation is that except for a few extreme cases, which are not likely to occur in reality, no matter how the parameters and pore shapes are changed, the general trends of simulated sorption isotherms are maintained. In other words, capillary condensation occurs in the wood-water system and can dominate the entire hygroscopic region. Therefore, the conclusions in chapter 5 should hold in more general terms.

Chapter 7: Cell Wall Pore Size Distributions in the Hygroscopic Range

7.1 Introduction

More and more efforts are being devoted to better understand cell wall architecture, largely due to the growing need for bio-fuels, bio-products and wood products with better in-service performance and higher strength (Busse-Wicher et al. 2014, Ding et al. 2012, Wilkerson et al. 2014). However, the interaction of cell wall biopolymers and a far more complicated biosynthetic process have made this task very challenging (Somerville et al. 2004, Oda and Fukuda 2012).

Cell wall pore structure is part of the cell wall architecture and there are three major difficulties in experimental evaluation. The first comes from the structural changes (swelling and shrinking) of the walls from moisture variation. Most experimental techniques have problems from preserving original cell wall structure when isolating moisture from wood. Freezing and solvent exchange drying attempted to solve this problem, however, they can only partly preserve the original structure (Clair et al. 2008). Recent attempts were made with alcohol exchange and supercritical drying techniques (Clair et al. 2008, Chang et al. 2009, 2015). One drawback of this method is that alcohol exchange is performed on fully saturated cell walls with no success on partly saturated cell walls.

The second difficulty is caused by the small pore sizes. Most pore analysis apparatuses, such as the porosimeter and the N_2 gas adsorption analyzer, are not capable to accurately detect pores below 1nm, though recent advances have been made by using the CO_2 gas adsorption technique (Kojiro et al. 2010). Nevertheless, a drawback of this technique is that the vacuum pretreatment will affect the moist cell wall pore structure. Thus, most gas absorption measurements are performed on dried cell walls.

The third difficulty is pore accessibility. In chapter 3, the connectivity among pores were indirectly evaluated through the scanning curve patterns. Unfortunately, no effort has been made on addressing accessibility of these pores so far. Indeed, it is probably fair to say that current experimental techniques do not allow accurate characterization of partly saturated pore structures. Hence, hysteresis-modeling approach might be the best way to predict cell wall pore change with moisture before new experimental techniques are developed.

In this chapter, the *PSD* and their association with the main wall polymers were explored in the hygroscopic range by bridging the gap between simulated sorption isotherms in chapter 5 and experimental ones. Since *PSD* at mostly room temperature is of interest, only one temperature level 25°C is considered here. Two additional variables, namely, the volumetric strain of cell walls and the adsorbed water density were derived from the predicted *PSD* to verify the soundness of assumptions and proposed calculation method.

There was an expectation that the elucidated cell wall pore structures could provide insights into formation of cell walls. For example, *PSD* of pores associated with lignin might provide some idea of lignin's deposition mechanism; and *PSD* of pores associated with cellulose might provide some insight into aggregation of cellulose microfibrils and their binding with hemicellulose. From a material point of view, the distributions of nanopores within wall polymers might provide an insight of cell wall deformations as influenced by individual polymers. Furthermore, it might inspire the designing of more advanced cell wall structures with higher strength, and optimize the material properties made from individual biopolymers such as lignin and cellulose by adjusting the *PSD* through thermal or chemical modifications. Likewise, insight could be obtained on how to better design the pore structure of cell walls by pretreatments to facilitate saccharification of lignocelluloses in biofuel production.

7.2 Methodology

7.2.1 Definition of pores associated with wall polymers

The pores associated with the major wall polymers were defined. Pores inside hemicellulose chains, at the interface of the hemicellulose and cellulose, and at the interface of hemicellulose and lignin were defined as pores associated with hemicellulose (PAH). Pores in “pure” amorphous cellulose chains were defined pores associated with cellulose (PAC). Pores inside lignin structures were defined as pores associated with lignin (PAL). Consequently, the total cell wall pores (PAT) was obviously the sum of PAH, PAC and PAL.

Subsequently, the weights of PAH, PAC and PAL were assigned according to the chemical composition data in chapter 3 for D-fir, aspen and WRC. 60% amorphous cellulose was assumed locating at microfibril surfaces based on general crystallinity values (Walker 2006). Since no published data could be found to support the proportion of lignin located at the interface of hemicellulose and lignin, 20% was assumed as an acceptable level.

7.2.2 Assumptions made on swelling of cell walls

The most challenging question of this investigation pertains to the changes of cell wall pore sizes with *M*. A general assumption here was that the swelling can cause either generation of new pores or swelling of existing pores. It was further assumed that 0.63nm pores (the smallest pores considered in the simulation) were firstly generated in cellulose, hemicellulose and lignin. In other words, the initial values of PAH, PAC and PAL were 0.6nm. Then, with the increase of *M*, these pores could become larger. The maximum values of PAH, PAC and PAL were assumed inversely proportional to the reported modulus of elasticity of the wall polymers under moist conditions (Salmén 2004). For example, PAH with the least modulus could swell to the largest pore size of

2.2nm, and PWC and PWL corresponding to larger moduli could only swell to 0.95nm. Theoretically, the pore sizes were supposed to continuously increase, however, as only four pore sizes (0.63nm, 0.95nm, 1.6nm, 2.2nm) were simulated in this study, pores could only swell from 0.63nm to 0.95nm, from 0.95nm to 1.6nm, and from 1.6nm to 2.2nm.

It is generally accepted that generation of new pores is accompanied by exposing more accessible hydroxyls. Since the accessible hydroxyls were found to increase while H reaches around 65% (Taniguchi 1978), it is assumed that new pores could be created when $H > 65\%$. It was further assumed that for cellulose 0.63nm and 0.95nm pores begin to form at H =5% and 25%, respectively. For hemicellulose, the four pore sizes begin to form at H =5%, 15%, 45% and 95%, respectively. The values of these critical Hs are based on H_u (the H where capillary condensation occurs), predicted from simulated sorption isotherms in chapter 5.

The *PSD* at the absolute dried states from chapter 3 provided a good boundary condition at M=0%. The detected micropores were assigned to lignin based on arguments made by Kojiro et al. (2008, 2010) and Nakatani et al. (2008). The *PSD* at fully saturated state from chapter 3 provided another boundary condition at M_{fsp}. The uncertainties in this boundary condition were large because of the difficulties in determining M_{fsp} and large experimental errors coming from the solute exclusion method, however, it restrained the maximum pore size reasonably.

When pores swell from one level to another, the increased volumes are calculated from the volume differences at the two levels. By letting V_0—V_3 be pore volumes at pore sizes of 0.63nm, 0.95nm, 1.6nm and 2.2nm, after swelling they become $V_1 = 2.27V_0$, $V_2 = 2.84V_1$ and $V_3 = 1.89V_2$. These pores will be filled with water when H is larger than H_u.

7.2.3 Pore size distribution calculation method

Eventually, the gap between simulated sorption isotherms in chapter 5 and experimental ones could be bridged by assigning volume weights to 0.63 – 2.2nm pores. From these volume weights at each *M*, the *PSD*s in the entire hygroscopic range could be obtained. The main calculation procedure is summarized below:

1. Update objective *M* and mass of adsorbed water in existing pores according to the new *H*.
2. Certainty percentage of existing empty pores are filled by water if the water condensation conditions are met.
3. Certain percentage of 1.6nm pores transform to 2.2nm if the swelling assumptions are met.
4. Certain percentage of 0.95nm pores transform to 1.5nm if the swelling assumptions are met.
5. Certain percentage of 0.65nm pores transform to 0.95nm if the swelling assumptions are met.
6. New 0.65 nm pores are generated if all pore generation assumptions are met.

Since the percentages in steps 2–5 and the quantity of new generated pores in step 6 were not certain, the "trial and error" approach was used. These steps were repeated until the simulated *M*s were equal to experimental ones and the relationship between cell wall volume and *M* was more or less linear.

The aim here was to predict *PSD* at *M*s corresponding to *H* = {0, 5%, 15%, 25%, 35%, 45%, 55%, 65%, 75%, 85%, 95%}. First, two numerical tables (Tables 7.1 and 7.2) were prepared from experimental (Fig. 7.1) and simulated sorption isotherms (Figs. 5.8a and 5.8b) by simple linear interpolations. Since the focus was swelling of cell walls from dried states, all data points were taken from adsorption sections. Table 7.1 provided the objective *M* at each *H*, and Table 7.2 was used to calculate the mass of water inside simulated pores. The gas-like adsorbed water is ignored in mass calculation because of their much smaller densities compared to that of the liquid-like state.

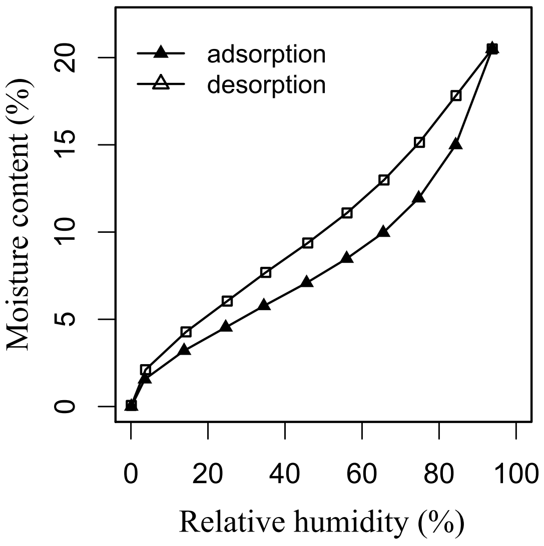

Figure 7.1: An experimental sorption isotherm for aspen at 25°C.

Table 7.1: *M*s linearly interpolated from Fig. 7.1 at the *H*s of interest.

H (%)	*M* (%)	
	Adsorption	Desorption
0	0	0.06
5	1.79	2.36
15	3.35	4.39
25	4.59	6.04
35	5.83	7.69
45	7.02	9.23
55	8.34	10.91
65	9.89	12.85
75	12.03	15.17
85	15.39	17.99
95	20.5	20.5

Table 7.2: Adsorbed water density in PW_1 and PW_2 pores linearly interpolated from simulated sorption points in Fig. 5.8a and 5.8b.

H (%)	adsorbed water density in PW_1 pores (g/cc)				adsorbed water density in PW_2 pores (g/cc)			
	0.63nm	0.95nm	1.6nm	2.2nm	0.63nm	0.95nm	1.6nm	2.2nm
0	0	0	0	0	0	0	0	0
5	0.9288	2.310E-04	8.216E-05	4.182E-05	1.537E-04	6.390E-05	2.835E-05	1.734E-05
15	1.0857	0.9031	3.217E-04	1.425E-04	4.838E-04	2.149E-04	9.848E-05	5.525E-05
25	1.0955	0.9509	0.9304	0.3890	0.3607	3.893E-04	1.760E-04	1.052E-04
35	1.1054	0.9681	0.9400	0.9276	0.8984	7.305E-04	2.571E-04	1.533E-04

H (%)	adsorbed water density in PW_1 pores (g/cc)				adsorbed water density in PW_2 pores (g/cc)			
	0.63nm	0.95nm	1.6nm	2.2nm	0.63nm	0.95nm	1.6nm	2.2nm
45	1.1153	0.9829	0.9478	0.9385	0.9587	0.8386	3.580E-04	1.991E-04
55	1.1241	0.9954	0.9558	0.9495	0.9962	0.9318	0.4190	2.653E-04
65	1.1305	1.0080	0.9681	0.9604	1.0007	0.9501	0.9506	0.9498
75	1.1368	1.0154	0.9799	0.9679	1.0205	0.9615	0.9573	0.9652
85	1.1431	1.0212	0.9914	0.9742	1.0451	0.9707	0.9636	0.9709
95	1.1494	1.0270	0.9960	0.9805	1.0696	0.9856	0.9699	0.9742

The calculation was based on 1 g dry aspen wood (the same approach was used for the other two species). From the chemical composition analysis (Table 3.7) and definitions of PAC, PAH and PAL, the effective mass of amorphous cellulose, hemicellulose and lignin (Table 7.3) for *PSD* calculations were obtained. They served as the foundation for further volume weights calculation for different pore sizes.

Table 7.3: Effective mass of wall polymers of aspen for *PSD* calculations.

Substance	Mass (g)
Dry wood	1.0000
Crystalline cellulose	0.3059
Amorphous cellulose	0.0816
Hemicellulose	0.3754
Lignin	0.1894
Extractive	0.0418

The calculation details for determining *PSD* when increasing *H* from 0 to 5% and from 55% to 65% were provided as two examples. At the initial dry state (*H* = 0), from the measured micropore size distribution (Fig. 3.8b), the cumulative pore volume in the range of 0.4 – 0.82nm and 0.82 – 1.47nm were assigned to 0.63nm and 0.95nm PAL, respectively (column 3 in Table 7.4). When *H* was increased to 5%, the following steps were followed.

Step1: the objective *M* = 1.79% (Table 7.1) corresponding to 0.0017 g total condensed water in the cell wall pores.

Step 2: no condensed water would fill existing PAL.

Steps 3 – 5: these steps were skipped as the swelling assumptions were not met.

Step 6: The 0.0017g water were distributed to PAC and PAH according to their mass weights, and then, the converted to volumes (column 4 in Table 7.3) based on density values in Table 7.2.

Table 7.4: Examples of calculating pore volumes of PAL, PAC and PAH at four pore sizes for aspen.

Pore volume	Pore Size	*H* from 0 to 5%		*H* from 45% to 55%			
		initial	final	initial	IS1	IS2	final
PAL (cc)	0.63nm	0.0167	0.0167	0.0169	0.0169	0.0169	0.0169
	0.95nm	0.0077	0.0077	0.0079	0.0079	0.0079	0.0079
	1.6nm	0	0	0	0	0	0
	2.2nm	0	0	0	0	0	0
PAC (cc)	0.63nm	0	0.0034	0.0058	0.0058	0.0051	0.0052
	0.95nm	0	0	0.0029	0.0029	0.0045	0.0045
	1.6nm	0	0	0	0	0	0
	2.2nm	0	0	0	0	0	0
PAH (cc)	0.63nm	0	0.0158	0.0258	0.0258	0.0227	0.0232
	0.95nm	0	0	0.0147	0.0132	0.0202	0.0202
	1.6nm	0	0	0.0015	0.0057	0.0057	0.0057
	2.2nm	0	0	0	0	0	0

When *H* was increased from 45% to 55%, the following steps were followed.

Step 1: the objective *M* = 7.02% corresponded to 0.702g total condensed water in the cell wall pores; water mass in existing pores was updated based on density values at 55% *H* in Table 7.2.

Step 2: water started to condense in existing 0.95nm PAL. Initially, 100% 0.95nm PAL was allowed to be filled with water instantaneously. However, this led to very small swelling of the cell wall, which was not consistent with the linear relationship between swelling and *M* from past experiments reported in literature (Skaar 1972). Therefore, the filling percentage was adjusted to 60%, thus having an additional water amount of 0.0076g.

Step 3: this step was skipped as no 2.2nm pore could be formed at this stage.

Step 4: the first intermediate state (column IS1 in Table 7.4) was obtained by assuming 10% of 0.95nm PAH transformed to 1.6nm PAH.

Step 5: the second intermediate state (column IS2 in Table 7.4) was obtained by assuming 12% of 0.63nm PAC and PAH converts to 0.95nm.

Step 6: At this point, the unassigned additional water was 0.0008g. Let 80% additional water be condensed water in newly generated 0.63nm PAC and PAH, and 20% additional water in 0.63nm PAL. The distribution of water within the 0.63nm PAC and PAH are based on their mass weights.

As it was pointed out earlier, the values of percentage in steps 3 – 5 were found by "trial and error". From experience built in this project, this usually requires 5 – 8 times manual adjustment. In this way, the final *PSD* at *H* = 55% (column 8 in Table 7.4) was obtained.

All calculations were based on 1g of dry wood. The calculated pore volumes were not normalized by the maximum pore volume at each pore size because the absolute volumes related to wall polymers is more interesting than their relative probabilities.

7.2.4 Smoothing of *PSD*

The obtained *PSD* was very coarse due to the limited four sizes simulated. In order to smooth the *PSD*, for each pore size, the following normal distribution was assumed:

$$lnd_{effi} \sim N(\mu_i, \sigma^2) \qquad (7.1)$$

where d_{effi} is the effective pore diameter (nm), and i = {1, 2, 3, 4}.

The means χ_i = {0.63nm, 0.95nm, 1.6nm, 2.2nm}, and standard deviation (ψ) were assumed to be 0.15nm. By letting j_1—j_4 be the volume weights for the four pore sizes the final soothed *PSD* was:

$$lnd_{eff1} = j_1 lnd_{eff1} + j_2 lnd_{eff2} + j_3 lnd_{eff3} + j_4 lnd_{eff4} \sim \sum_{i=1}^{4} j_i N(\chi_i, \psi^2) \qquad (7.2)$$

7.3 Results and Discussion

7.3.1 Calculated *PSD* and smoothed curves

Table 7.5 presents calculated pore volumes of PAL, PAC and PAH corresponding to four sizes {0.63nm, 0.95nm, 1.6nm, 2.2nm} at 0 – 95% humidity range for D-fir, aspen, and WRC. After smoothing, the obtained *PSD*s were plotted in Figs. 7.2–7.4.

Table 7.5: Pore volumes of PAL, PAC and PAH at four pore sizes from 0–95%*H* for 1g aspen, D-fir and WRC.

Species	Pore volume	Pore size	*H*										
			0	5%	15%	25%	35%	45%	55%	65%	75%	85%	95%
D-fir	PAL (cc)	0.63nm	0.0114	0.0114	0.0114	0.0114	0.0114	0.0116	0.0117	0.0105	0.0092	0.0069	0.0046
		0.95nm	0.0067	0.0067	0.0067	0.0067	0.0067	0.0067	0.0067	0.0095	0.0123	0.0176	0.0228
		1.6nm	0	0	0	0	0	0	0	0	0	0	0
		2.2nm	0	0	0	0	0	0	0	0	0	0	0
	PAC (cc)	0.63nm	0	0.0033	0.0051	0.0059	0.0062	0.0057	0.0051	0.0045	0.0040	0.0030	0.0020
		0.95nm	0	0	0	0.0012	0.0018	0.0032	0.0048	0.0060	0.0072	0.0095	0.0118
		1.6nm	0	0	0	0	0	0	0	0	0	0	0
		2.2nm	0	0	0	0	0	0	0	0	0	0	0
	PAH (cc)	0.63nm	0	0.0177	0.0262	0.0304	0.0322	0.0294	0.0262	0.0218	0.0174	0.0122	0.0064
		0.95nm	0	0	0.0027	0.0086	0.0120	0.0184	0.0246	0.0322	0.0363	0.0409	0.0426
		1.6nm	0	0	0	0	0	0.0027	0.0080	0.0149	0.0314	0.0520	0.0813
		2.2nm	0	0	0	0	0	0	0	0	0	0	0.0067
Aspen	PAL (cc)	0.63nm	0.0167	0.0167	0.0167	0.0167	0.0167	0.0169	0.0169	0.0151	0.0122	0.0077	0.0031
		0.95nm	0.0077	0.0077	0.0077	0.0077	0.0077	0.0079	0.0079	0.0119	0.0184	0.0287	0.0391
		1.6nm	0	0	0	0	0	0	0	0	0	0	0
		2.2nm	0	0	0	0	0	0	0	0	0	0	0
	PAC (cc)	0.63nm	0	0.0034	0.0053	0.0063	0.0061	0.0058	0.0052	0.0047	0.0038	0.0024	0.0010
		0.95nm	0	0	0	0.0012	0.0019	0.0029	0.0045	0.0057	0.0077	0.0109	0.0141
		1.6nm	0	0	0	0	0	0	0	0	0	0	0
		2.2nm	0	0	0	0	0	0	0	0	0	0	0
	PAH (cc)	0.63nm	0	0.0158	0.0235	0.0279	0.0273	0.0258	0.0232	0.0195	0.0143	0.0082	0.0027
		0.95nm	0	0	0.0024	0.0077	0.0109	0.0147	0.0202	0.0258	0.0319	0.0357	0.0300
		1.6nm	0	0	0	0	0	0.0015	0.0057	0.0138	0.0299	0.0589	0.1058
		2.2nm	0	0	0	0	0	0	0	0	0	0	0.0084
WRC	PAL (cc)	0.63nm	0.0136	0.0136	0.0136	0.0136	0.0136	0.0138	0.0169	0.0159	0.0131	0.0094	0.0044
		0.95nm	0.0079	0.0079	0.0079	0.0079	0.0079	0.0079	0.0079	0.0102	0.0165	0.0248	0.0363
		1.6nm	0	0	0	0	0	0	0	0	0	0	0

Species	Pore volume	Pore size	*H*										
			0	5%	15%	25%	35%	45%	55%	65%	75%	85%	95%
		2.2nm	0	0	0	0	0	0	0	0	0	0	0
	PAC (cc)	0.63nm	0	0.0035	0.0055	0.0064	0.0064	0.0061	0.0056	0.0052	0.0043	0.0031	0.0014
		0.95nm	0	0	0	0.0012	0.0020	0.0030	0.0044	0.0051	0.0072	0.0100	0.0138
		1.6nm	0	0	0	0	0	0	0	0	0	0	0
		2.2nm	0	0	0	0	0	0	0	0	0	0	0
	PAH (cc)	0.63nm	0	0.0151	0.0223	0.0263	0.0264	0.0251	0.0231	0.0208	0.0157	0.0106	0.0040
		0.95nm	0	0	0.0023	0.0073	0.0103	0.0140	0.0185	0.0219	0.0294	0.0337	0.0335
		1.6nm	0	0	0	0	0	0.0015	0.0046	0.0099	0.0211	0.0420	0.0818
		2.2nm	0	0	0	0	0	0	0	0	0	0	0.0060

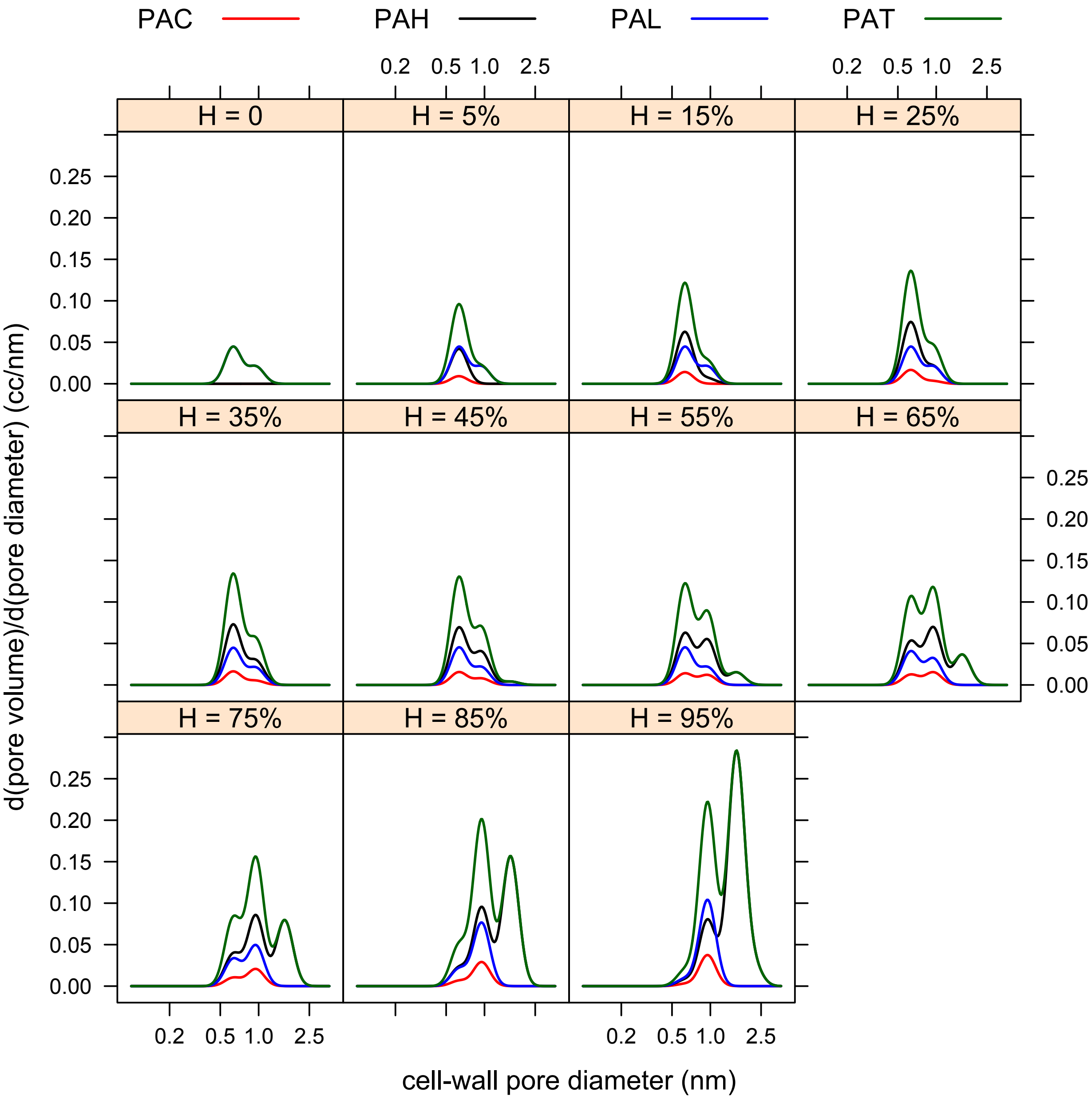

Figure 7.2: Smoothed *PSD* of PAC, PAH, PAL and PAT from 0 – 95% relative humidity range for 1g of aspen.

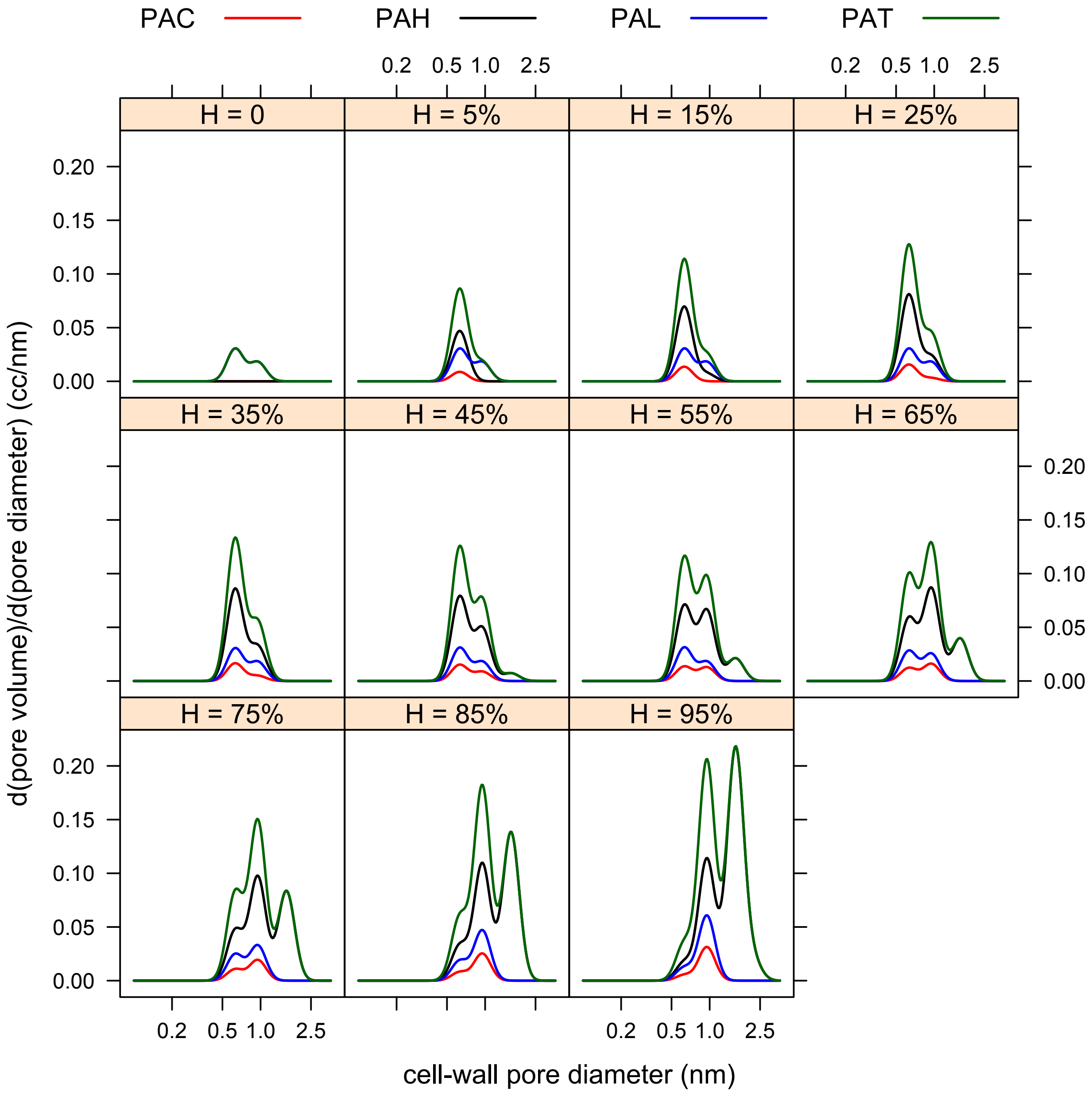

Figure 7.3: Smoothed *PSD* of PAC, PAH, PAL and PAT from 0 – 95% relative humidity range for 1g of D-fir.

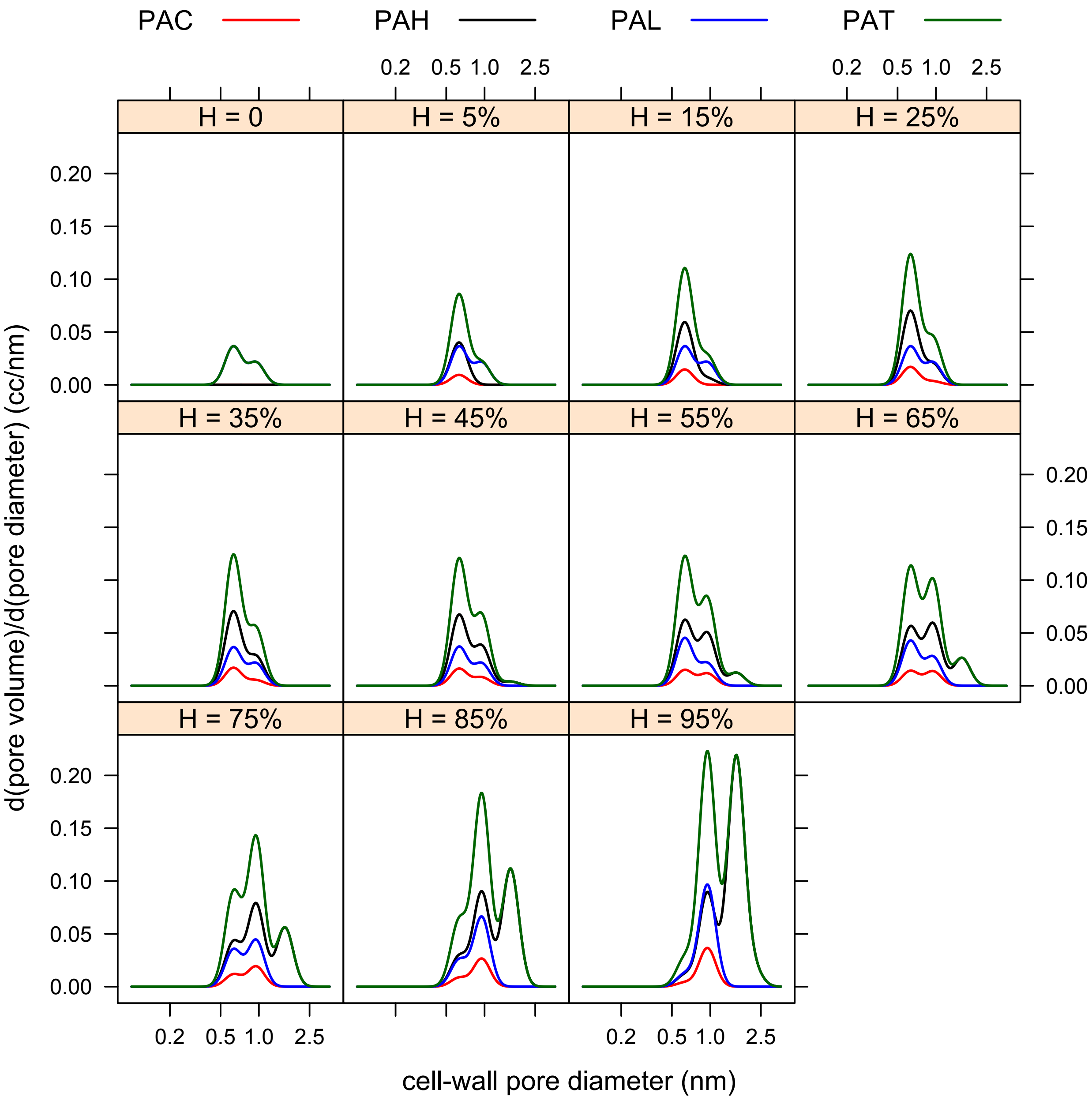

Figure 7.4: Smoothed *PSD* of PAC, PAH, PAL and PAT from 0 – 95% relative humidity range for 1g of WRC.

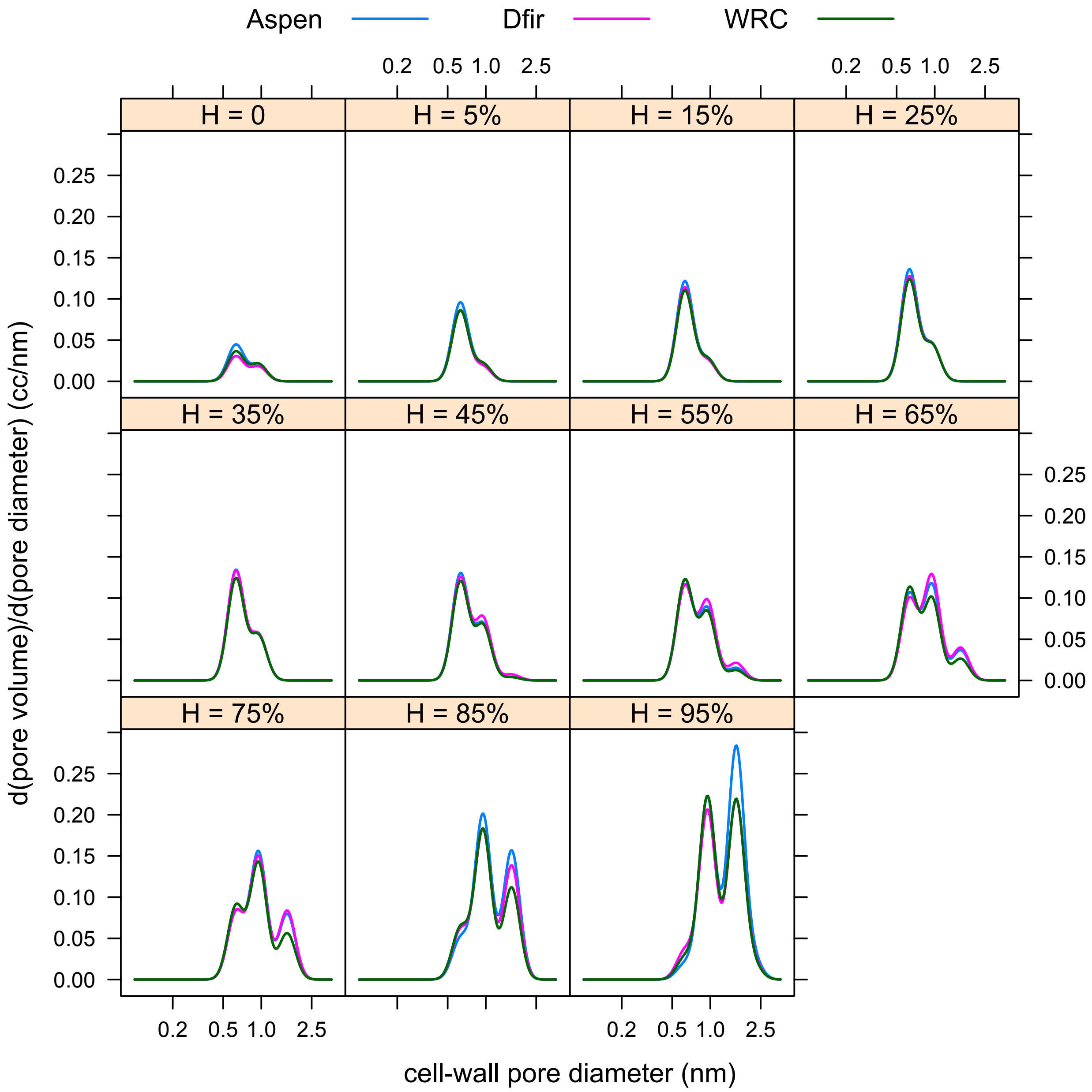

Figure 7.5: Comparison of smoothed *PSD*s evolution with *H* of PAT from the three species.

Generally, the main characteristics shown in calculated *PSD*s reflected the assumptions made on swelling of cell walls. For example, the two bumps of PAL in Figs. 7.2 – 7.4 came from the assumption made on pores in dried cell walls. Later, PAH plays a leading role in pore volume evolution with increasing *H* especially after 65% when 1.6nm pores become dominant. This was caused by two factors. One was the definition of pores associated with wall polymers. The effective mass of amorphous cellulose, hemicellulose and lignin in Table 7.3 corresponded to the wall matrix of PAC, PAH and PAL. Obviously, the wall substance of PAH = 0.3754g was the largest. The second factor was the assumption of being much easier to generate and swell pores in the hemicellulose matrix. Even though the chemical components, initial pore distributions and M_{emc} at specified *H*s were different for the three species, no prominent differences could be detected from *PSD*s in Fig. 7.5. This was probably because the same assumptions and calculation procedures were followed.

The above results clearly demonstrate that the obtained *PSD* evolution with *H* mainly depends on the assumptions made in calculations. Currently, there are no better ways to test these assumptions and no past research data to compare to. Furthermore, the "trial and error" approach might bring additional numerical errors. In steps 2–4 of the calculation process it was possible to have different percentages, but still meet the final *M* criterion. Further calculation could be carried out on the volumetric strain of cell walls and the adsorbed water density from the *PSD* in the hygroscopic range. The strain-*M* and adsorbed water density-*M* relationships could provide indirect ways to test *PSD* evolution with *M*.

7.3.2 Swelling volumetric strain of cell walls

By assuming that the cell wall volume is the sum of the pore and cell wall substance volume and that the cell wall substance volume does not change with *M*, the swelling volumetric strain of the cell walls (ε_{vcw}) at *M* can be computed as:

$$\varepsilon_{vcw} = \frac{V_{cw}-V_{cw0}}{V_{cw0}} \qquad (7.3)$$

where V_{cw} is the cell wall volume (cc) at *M*, and V_{cw0} is the cell wall volume at the dried state (cc). Similarly, the swelling volumetric strain of the wood (ε_v) at *M* can be computed as:

$$\varepsilon_v = \frac{V - V_0}{V_0} \tag{7.4}$$

where V is the volume of the wood at M (cc), and V_0 is the volume of dried wood (cc). Furthermore, by assuming that the volume of wood is the sum of the volume of cell walls and lumen (V_{lum}) and V_{lum} does not change with M, then

$$V - V_0 = V_{cw} + V_{lum} - (V_{cw0} + V_{lum}) = V_{cw} - V_{cw0} \tag{7.5}$$

Using this relationship for Eqs. (7.3) and (7.4), the following formula is obtained:

$$\varepsilon_{vcw} = \frac{V_0}{V_{cw0}} \varepsilon_v = C_v \varepsilon_v \tag{7.6}$$

where C_v is a constant. This equation demonstrates that swelling of cell walls should be linear in the hygroscopic range, which was partly consistent with the reported fact that swelling of the wood is very close to linear between 5%–25% M (Fig. 3.11 in Skaar 1972). Fig. 7.6 shows the relationship between ε_{vcw} and M for the three species. These curves were basically linear when M is larger than 10%. Considering the numerous assumptions that have been made concerning the

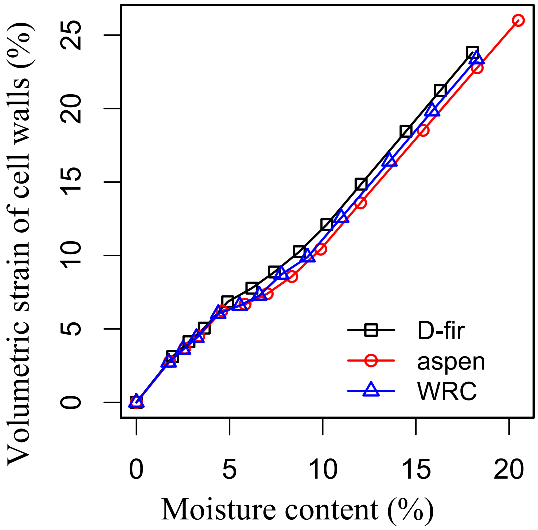

Figure 7.6: Relationship between volume strain of cell walls and M_{emc} for the three species.

swelling of cell walls and the numerical uncertainties in the simulation, the result here could be considered satisfactory.

7.3.3 Density of adsorbed water

The density of adsorbed water at each *M* could be calculated from the quotient of mass of adsorbed water divided by the volume of filled cell wall pores. Fig. 7.7 shows the density of adsorbed water in the hygroscopic range for the three species. A consistent trend was identified for the simulated densities, i.e. reaching a maximum value of 1.07g/cc at around 3.5% *M* and then leveling out to 1.01g/cc at around 20% *M*. However, for simulated sorption isotherms at one specified pore size (Figs. 5.8a and 5.8b), the density of adsorbed water increased with *H* monotonically. It seems that *PSD*s at different *M*s could modify the monotonic increase trend. The domination of large size pores at higher *H* (Fig. 7.5) gives more weight to condensed water in larger pores with lower densities, thus reversing the increasing trend.

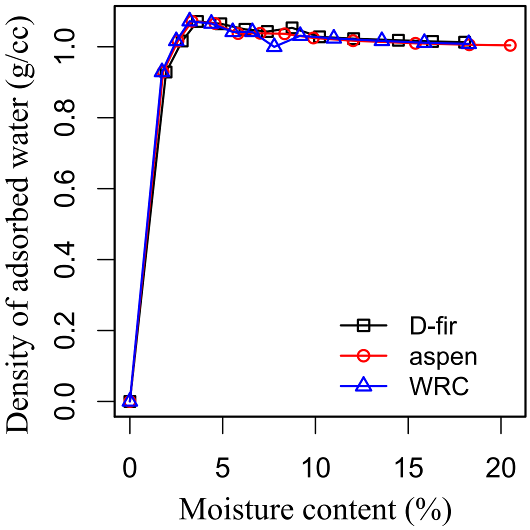

Figure 7.7: Density of adsorbed water in the hygroscopic range for the three species.

Compared with the corrected density of adsorbed water in the hygroscopic range from Stamm and Seborg (1935)'s sitka spruce data (Table 6.4), the simulated density reached the maximum value at a much lower *M*. This could have been caused by unreasonable *PSD*s at lower *M*s. For instance, the new pores were generated too fast, or more small pores could swell to larger ones. However, it was also possible that experimental errors existed in Stamm and Seborg (1935)'s data that skewed the trend. More solid data of density of adsorbed water in the hygroscopic range are needed in the future to justify the obtained *PSD*s.

7.4 Conclusion

Based on simulated sorption isotherms in chapter 5 and the assumptions made on swelling of cell walls, the cell wall *PSD*s in the hygroscopic range were obtained for the three species from a "trial and error" calculation approach. The consistent *PSD* trends from the three species indicated the leading role of assumptions in the entire calculation procedure. However, current experimental techniques do not allow justifying most assumptions made in calculation and verifying the attained *PSD*s directly. Instead, the volumetric strain of cell walls and the density of adsorbed water in the hygroscopic range were calculated and compared with the literature data. The predicted values agree with literature data qualitatively, indicating the soundness of the assumptions and the calculation procedures. More solid data of swelling of wood and adsorbed water density in the hygroscopic range are needed in the future to guide and analyze the derived *PSD*s.

Chapter 8: General Conclusion

The water sorption hysteresis phenomenon and cell wall pore structure were investigated in this study through a combined experimental, modeling and simulation approach. The main conclusions are as follows.

1. Five consistent hysteresis patterns revealing important geometric properties of scanning curves were observed for Douglas-fir, aspen and western red cedar at 25 and 40°C.
2. The satisfactory congruency and wiping-out properties revealed from the hysteresis patterns indicate that interactions among cell wall pores are negligible.
3. The geometric interpretation of the Preisach model satisfactorily explained the five hysteresis patterns, and further quantitative modeling with a nonparametric numerical implementation could be considered as satisfactory.
4. Grand canonical Monte Carlo (GCMC) technique was successfully applied in a simplified wood-water system to simulate the sorption isotherms and hysteresis at 25 and 40°C. Hysteresis is well explained by existence of metastable states associated with capillary condensation and evaporation of water in cell walls.
5. The simulation results cast doubt on the layering and clustering sorption theories, and instead suggest an alternative sorption mechanism driven by capillary condensation.
6. Based on simulated sorption isotherms and the assumptions made on swelling of cell walls, the cell wall *PSD*s in the hygroscopic range were obtained for the three species from a "trial and error" calculation approach. Further derived volumetric strain of cell walls and the density of adsorbed water in the hygroscopic range agree with literature data qualitatively, indicating the soundness of assumptions and proposed calculation procedures.

This study has raised many questions that need further investigation. For hysteresis patterns, more close *H* settings are needed to better describe the scanning curves. More wood species and temperature levels should be performed to test the generality of these patterns. Within one species, different regions such as heartwood and sapwood, mature wood and juvenile wood, wood from different tree heights and annual rings can be further studied. The large uncertainty from the solute exclusion method should be further analyzed in the future. More reliable solutes or technical improvement might be expected. The interesting hysteresis findings from the gas adsorption isotherms of dry wood should be explored in the future to reveal the underlying mechanism. As mentioned in chapter 7, more experiments should be conducted on the adsorbed water density and cell wall dimensional change with *M* in the hygroscopic region.

For simulations, on one hand more accurate model input parameters are needed, i.e., cell wall-water interaction strength and hydrogen bonding, available sorption sites for different wall polymers, and cell wall pore shape. More water models, such as TIP3P or TIP5P (Karniadakis et al. 2005), should also be considered. New experimental techniques are probably needed to explore these nanoscale variables. On the other hand, more direct experimental evidences regarding pore size distributions of partly saturated cell walls and cell wall density at different moisture contents are needed to examine the developed physical model and simulation approach.

Generally, the molecular simulation approach applied in this study demonstrates great potential in exploring the sorption process at nanoscale. This technique can be further developed to study more general fields in wood physics or mechanics.

References

Allen, M.P., Tildesley, D.J., Computer simulation of liquids. Oxford university press, Oxford, 1989.

Arthur, E., Tuller, M., Moldrup, P., de Jonge, L.W. (2016) Evaluation of theoretical and empirical water vapor sorption isotherm models for soils. Water Resour. Res., 52(1):190-205.

Avramidis, S. (1997) The basics of sorption. In: International Conference on Wood-Water Relations, June 16-17, Copenhagen, Denmark.

Barkas, W.W. (1942) Wood-water relationships, VII. Swelling pressure and sorption hysteresis in gels. Trans. Faraday Soc. 38:194-209.

Basu, S., Shivhare, U.S., Mujumdar, A.S., 2006. Models for sorption isotherms for foods: a review. Dry. Technol. 24(8):917-930.

Berendsen, H.J.C., Grigera, J.R., Straatsma, T.P. (1987) The missing term in effective pair potentials. J. Phys. Chem. 91(24): 6269-6271.

Busse-Wicher, M., Gomes, T.C., Tryfona, T., Nikolovski, N., Stott, K., Grantham, N.J., Bolam, D.N., Skaf MS, Dupree P (2014) The pattern of xylan acetylation suggests xylan may interact with cellulose microfibrils as a twofold helical screw in the secondary plant cell wall of Arabidopsis thaliana. Plant J. 79(3): 492-506.

Carmeliet, J., De Wit, M.H.D., Janssen, H. (2005) Hysteresis and moisture buffering of wood. Symposium of Building Physics in the Nordic Countries, June 13-15th, Reykjavík, Iceland, pp. 55-62.

Chang, S.S., Clair, B., Ruelle, J., Beauchêne, J., Di Renzo, F., Quignard, F., Zhao, G.J., Yamamoto, H., Gril, J. (2009) Mesoporosity as a new parameter for understanding tension stress generation in trees. J. Exp. Bot. 60(11): 3023-3030.

Chang, S.S., Quignard, F., Alméras, T., Clair, B. (2015) Mesoporosity changes from cambium to mature tension wood: a new step toward the understanding of maturation stress generation in trees. New Phytol. 205(3): 1277-1287.

Chen, C.M., Wangaard, F.F. (1968) Wettalility and the hysteresis effect in the sorption of water vapour by wood. Wood Sci. Technol. 2:177-187.

Child, T.F. (1972) Pulsed n.m.r. study of molecular motion and environment of sorbed water on cellulose. Polymer. 13:259-264.

Chirkova, J., Andersons, B., Andersone, I. (2007) Study of the structure of wood-related biopolymers by sorption methods. BioResources 4(3): 1044-1057.

Christensen, G.N., Kelsey, K. E. (1958) The sorption of water vapor by the constituents of wood: determination of sorption isotherms. Austr. J. Appl. Sci. Vol. 9(3): 265-282.

Clair, B., Gril, J., Di Renzo, F., Yamamoto, H., Quignard, F. (2008) Characterization of a gel in the cell wall to elucidate the paradoxical shrinkage of tension wood. Biomacromolecules. 9(2): 494-498.

Cohan, L.H. (1938) Sorption hysteresis and the vapor pressure of concave surfaces. J. Am. Chem. Soc. 60(2): 433-435.

Coasne, B., Gubbins, K.E., Pellenq, R.J. (2005) Domain theory for capillary condensation hysteresis. Phys. Rev. B. 72(2):024304.

Derome, D., Derluyn, H., Zillig, W., Carmeliet, J. (2008) Model for hysteretic moisture behavior of wood. Proceedings of the 8th Symposium on Building Physics in the Nordic Countries, June 16-18, Copenhagen, Vol. 2: 959-966.

Ding, S.Y., Liu, Y.S., Zeng, Y., Himmel, M.E., Baker, J.O., Bayer, E.A. (2012) How does plant cell wall nanoscale architecture correlate with enzymatic digestibility? Science. 338(6110): 1055-1060

Enderby, J.A. (1956) The domain model of hysteresis. Part 2.—Interacting domains. Trans. Faraday Soc. 52:106-120.

Everett, D.H., Whitton, W.I. (1952) A general approach to hysteresis. Trans. Faraday Soc. 48: 749-757.

Everett, D.H., Smith, F.W. (1954) A general approach to hysteresis Part 2: Development of the domain theory. Trans. Faraday Soc. 50: 187-197.

Everett, D.H. (1954) A general approach to hysteresis. Part 3.—A formal treatment of the independent domain model of hysteresis. Trans. Faraday Soc. 50: 1077-1096.

Everett, D.H. (1955) A general approach to hysteresis. Part 4. An alternative formulation of the domain model. Trans. Faraday Soc. 51: 1551-1557.

Frandsen, H.L., Svensson, S., Damkilde, L. (2007) A hysteresis model suitable for numerical simulation of moisture content in wood. Holzforschung, 61:175-181.

Frenkel, D., Smit, B. (1996) Understanding molecular simulations: from algorithms to applications. Academic Press, New York, pp444.

Froix, M.F., Nelson, R. (1975) The interaction of water with cellulose from Nuclear Magnetic Resonance Relaxation times. Macromolecules 8(6): 726-730.

Garcia-Martinez, J., Xiao, C., Cychosz, K.A., Li, K., Wan, W., Zou, X., Thommes, M. (2014) Evidence of intracrystalline mesostructured porosity in zeolites by advanced gas sorption, electron tomography and rotation electron diffraction. ChemCatChem 6(11): 3110-3115.

Gillan, M.J., Alfè, D., Michaelides, A. (2016) Perspective: How good is DFT for water? arXiv preprint arXiv:1603.01990.

Gregg, S.J., Sing, K.S.W. (1982) Adsorption, Surface Area and Porosity. Academic Press, New York, pp303.

Grosman, A., Ortega, C. (2005) Nature of capillary condensation and evaporation processes in ordered porous materials. Langmuir. 21(23):10515-10521.

Hartley, I.D., Avramidis, S. (1993) Analysis of the wood sorption isotherm using clustering theory. Holzforschung 47(2):163-167.

Hartley, I.D. (1994) Characterization of water in wood below the fibre saturation point, Ph.D. Thesis, University of British Columbia, Canada, pp147.

Harris, D.C. (2003) Quantitative chemical analysis. W.H. Freeman and Company, NewYork, pp744.

Hietala, S., Maunu, S.L., Sundholm, F., Jämsä, S., Viitaniemi, P. (2002) Structure of thermally modified wood studied by liquid state NMR measurements. Holzforschung 56(5):522-528.

Hill, C.A.S. (2006) Wood Modification: Chemical, Thermal and Other Process. John Wiley & Sons. Ltd, England, pp239.

Hill, C.A.S., Norton, A., Newman, G. (2009) The water vapor sorption behavior of natural fibers. J. Appl. Polym. Sci. 112(3):1524-1537.

Hill, C.A.S., Norton, A.J., Newman, G. (2010) The water vapor sorption properties of Sitka spruce determined using a dynamic vapor sorption apparatus. Wood Sci. Technol. 44(3):497-514.

Hill, C.A.S, Keating, B.A., Jalaludin, Z., Mahrdt, E. (2012a) A rheological description of the water vapour sorption kinetics behavior of wood invoking a model using a canonical assembly of Kelvin-Voigt elements and a possible link with sorption hysteresis. Holzforschung 66(1):35-47.

Hill, C.A.S., Ramsay, J., Keating, B., Laine, K., Rautkari, L., Hughes, M., Constant, B. (2012b) The water vapour sorption properties of thermally modified and densified wood. J. Mater. Sci. 47(7):3191-3197.

Hill, C.A.S., Ramsay, J., Gardiner, B. (2015) Variability in water vapour sorption isotherm in Japanese Larch (Larix kaempferi Lamb.)–earlywood and latewood influences. International Wood Products Journal. 6(2):53-59.

Jalaludin, Z. (2012) The water vapour sorption behaviour of wood, PhD Thesis, Edinburgh Napier University, U.K, pp231.

Jorge, M., Seaton, N.A. (2002) Molecular simulation of phase coexistence in adsorption in porous solids. Mol. Phys. 100(24):3803-3815.

Kaminsky, R.D., Conner, W.C., Maglara, E. (1994) A direct assessment of mean-field methods of determining pore size distributions of microporous media from adsorption isotherm data. Langmuir. 10(5):1556-1565.

Karniadakis, G., Beskok, A., Aluru, N. (2005) Microflows and Nanoflows: Fundamentals and Simulation. Springer Science+Business Media, Inc., NewYork, pp817.

Kaukonen, M., Gulans, A., Havu, P., Kauppinen, E. (2012) Lennard-Jones parameters for small diameter carbon nanotubes and water for molecular mechanics simulations from van der Waals density functional calculations. J. Comput. Chem. 33(6):652-658.

Kelley, S.S., Rials, T.G., Glasser, W.G. (1987) Relaxation behaviour of the amorphous components of wood. J. Mater. Sci. 22(2):617-624.

Kellogg, R.M., Wangaard, F.F. (1969) Variation in the cell-wall density of wood. Wood Fiber Sci. 1(3):180-204.

Kittel, C., Kroemer, H. (1980) Thermal physics. W. H. Freeman and Company, New York, pp473.

Kelsey, K.E., Clark, L.E. (1956) The heat of sorption of water by wood. Aust. J. Appl. Sci. 7(2):160-175.

Kelsey, K.E. (1957) The sorption of water vapour by wood. Aust. J. Appl. Sci. 8: 42-54.

Kojiro, K., Furuta, Y., Ishimaru, Y. (2008) Influence of heating and drying history on micropores in dry wood. J. Wood Sci. 54:202-207.

Kojiro, J., Miki, T., Sugimoto, H., Nakajima, M., Kanayama, K. (2010) Micropores and mesopores in the cell wall of dry wood. J. Wood Sci. 56(2):107-111.

Kruk, M., Jaroniec, M., Sayari, A. (1997) Adsorption study of surface and structural properties of MCM-41 materials of different pore sizes. J. Phys. Chem. B. 101(4):583-589.

Kymäläinen, M., Rautkari, L., Hill, C.A.S. (2015) Sorption behaviour of torrefied wood and charcoal determined by dynamic vapour sorption. J. Mater. Sci. 50(23):7673-7680.

Lowell, S., Shield, J.E., Thomas, M.A., Thommes, M. (2004) Characterization of porous solids and powders: surface area, pore size and density. Kluwer Academic Publishers, Boston, pp347.

Lilly, M.P., Finley, P.T., Hallock, R.B. (1993) Memory, congruence, and avalanche events in hysteretic capillary condensation. Phys. Rev. Lett. 71(25):4186.

Lilly, M.P., Hallock, R.B. (2001) Probing the internal structure of nuclepore with hysteretic capillary condensation. Phys. Rev. B. 63(17):174503.

Lin, J.K., Ladisch, M.R., Patterson, J.A., Noller, C.H. (1987) Determining pore size distribution in wet cellulose by measuring solute exclusion using a differential refractometer. Biotechnol. Bioeng.29(8):976-981.

Mayergoyz, I.D. (1986) Mathematical models of hysteresis. EEE Trans. Magn. 22(5):603-608.

Mayergoyz, I.D. (1991) Mathematical Models of Hysteresis. Springer, New York, pp207.

Merakeb, S., Dubois, F., Petit, C. (2009) Modelling of the sorption hysteresis for wood. Wood Sci. Technol. 43(7-8):575-589.

Miki, T., Sugimoto, H., Kojiro, K., Furuta, Y., Kanayama, K. (2012) Thermal behaviors and transitions of wood detected by temperature-modulated differential scanning calorimetry. J. Wood Sci. 58:300-308.

Mualem, Y. (1973) Modified approach to capillary hysteresis based on a similarity hypothesis. Water Resour. Res. 9(5):1324-1331.

Mualem, Y. (1974) A conceptual model of hysteresis. Water Resour. Res. 10(3):514-520.

Mullins, E.J., McKnight, T.S. (2000) Canadian woods: their properties and uses (Third Edition). University of Toronto Press, Toronto, pp389.

Müller, E.A., Rull, L.F., Vega, L.F., Gubbins, K.E. (1996) Adsorption of water on activated carbons: a molecular simulation study. J. Phys. Chem. 100(4):1189-1196.

Nakatani, T., Ishimaru, Y., Iida, I. (2008) Micropore structure of wood: change in micropore structure accompanied by delignification. J. Wood Sci. 54:252-255.

Neimark, A.V., Ravikovitch, P.I., Grün, M., Schüth, F., Unger, K.K. (1998) Pore size analysis of MCM-41 type adsorbents by means of nitrogen and argon adsorption. J. Colloid Interface Sci. 207(1):159-169.

Neimark, A.V., Ravikovitch, P.I., Vishnyakov, A. (2000) Adsorption hysteresis in nanopores. Phys. Rev. E. 62(2):R1493.

Neimark, A.V., Ravikovitch, P.I. (2001) Capillary condensation in MMS and pore structure characterization. Microp. Mesop. Mat. 44:697-707.

Oda, Y., Fukuda, H. (2012) Initiation of cell wall pattern by a Rho-and microtubule-driven symmetry breaking. Science. 337(6100):1333-1336.

Ohba, T., Kaneko, K. (2007) Cluster-associated filling of water molecules in slit-shaped graphitic nanopores. Mol. Phys. 105(2-3):139-145.

Olek, W., Majka, J., Czajkowski, L. (2013) Sorption isotherms of thermally modified wood. Holzforschung 67(2):183-191.

Östberg, G., Salmen, L., Terlecki, J. (1990) Softening temperature of moist wood measured by differential scanning calorimetry. Holzforschung 44(3):223-225.

Papadopoulos, A.N. (2005) An investigation of the cell wall ultrastructure of the sapwood of then Greek wood species by means of chemical modification. Holz als Roh- und Weskstoff 63(6):437-441.

Panagiotopoulos, A.Z. (1987) Adsorption and capillary condensation of fluids in cylindrical pores by Monte Carlo simulation in the Gibbs ensemble. Mol. Phys. 62(3):701-719.

Patera, A., Derluyn, H., Derome, D., Carmeliet, J. (2016) Influence of sorption hysteresis on moisture transport in wood. Wood Sci. Technol. 50(2): 259-283.

Peralta, P.N. (1995a) Sorption of moisture by wood within a limited range of relative humidities. Wood Fiber Sci. 27(1):13-21.

Peralta, P.N. (1995b) Modelling wood moisture sorption hysteresis using the independent-domain theory. Wood Fiber Sci. 27(3):250-257.

Peralta, P.N. (1996) Moisture sorption hysteresis and the independent-domain theory: The moisture distribution function. Wood Fiber Sci. 28(4):406-410.

Peralta, P.N., Bangi, A.P. (1998a) Modeling wood moisture sorption hysteresis based on similarity hypothesis. Part 1. Direct approach. Wood Fiber Sci. 30(1):48-55.

Peralta, P.N., Bangi, A.P. (1998b) Modeling wood moisture sorption hysteresis based on similarity hypothesis. Part II. Capillary-radii approach. Wood Fiber Sci. 30(2):148-154.

Patera, A., Derluyn, H., Derome, D., Carmeliet, J. (2016) Influence of sorption hysteresis on moisture transport in wood. Wood Sci. Technol. 50(2):259-283.

Peterson, B.K., Walton, J.P., Gubbins, K.E. (1986) Fluid behavior in narrow pores. J. Chem. Soc. Faraday Trans. 82(10):1789-1800.

Pidgeon, L.M., Maass, O. (1930) The adsorption of water by wood. J. Am. Chem. Soc., 52(3): 1053-1069.

Pizzi, A., Eaton, N.J., Bariska, M. (1987a) Theoretical water sorption energies by conformational analysis. Wood Sci. Technol. 21(3): 235-248.

Pizzi, A., Bariska, M., Eaton, N.J. (1987b) Theoretical water sorption energies by conformational analysis. Part 2. Amorphous cellulose and the sorption isotherm. Wood Sci. Technol. 21(4): 317-327.

Popescu, C.M., Hill, C.A.S. (2013) The water vapour adsorption–desorption behaviour of naturally aged Tilia cordata Mill. Wood. Polym. Degrad. Stabil. 98(9):1804-1813.

Popescu, C.M., Hill, C.A.S., Curling, S., Ormondroyd, G., Xie, Y. (2014) The water vapour sorption behaviour of acetylated birch wood: how acetylation affects the sorption isotherm and accessible hydroxyl content. J. Mater. Sci. 49(5):2362-2371.

Popper, R., Niemz, P., Croptier, S. (2009) Adsorption and desorption measurements on selected exotic wood species. Analysis with the Hailwood-Horrobin model to describe the sorption hysteresis. Wood Res. 54(4):43-56.

Quantachrome Instruments (2011) Adsorptives for physisorption experiments: selection and their physical properties. Powder Tech Note 52.

Ramírez, A., Sierra, L. (2006) Simulation of nitrogen sorption processes in materials with cylindrical mesopores: Hysteresis as a thermodynamic and connectivity phenomenon. Chem. Eng. Sci. 61(13):4233-4241.

Rautkari, L., Hill, C.A.S., Hurling, S., Jalaludin, Z., Ormondroyd, G. (2013) What is the role of the accessibility of wood hydroxyl groups in controlling moisture content. J. Mater. Sci. 48(18):6352- 6356.

Ravikovitch, P.I., Domhnaill, S.Ó., Neimark, A.V., Schüth, F., Unger, K.K. (1995) Capillary hysteresis in nanopores: theoretical and experimental studies of nitrogen adsorption on MCM-41. Langmuir. 11(12): 4765-4772.

Ravikovitch, P.I., Vishnyakov, A., Neimark, A.V. (2001) Density functional theories and molecular simulations of adsorption and phase transitions in nanopores. Phys. Rev. E, 64(1):011602.

Rayirath, P., Avramidis, S., Mansfield, S.D. (2008) The effect of wood drying on crystallinity and microfibril angle in black spruce (Picea mariana). J. Wood Chem. Technol, 28(3):167-179.

Rojas, F., Kornhauser, I., Felipe, C., Cordero, S. (2001) Everett's sorption hysteresis domain theory revisited from the point of view of the dual site-bond model of disordered media. J. Mol. Catal. A: Chem. 167(1):141-155.

Ross, S.M. (2010) Introduction to Probability Models (10th edition), Elsevier, New York, pp784

Salmén, L. (2004) Micromechanical understanding of the cell-wall structure. C. R. Biologies. 327(9):873-880.

Salmén, L., Olsson, A.M., Stevanic, J., Simonović, J., Radotić, K. (2011) Structural organization of the wood polymers in the wood fibre structure. BioResources. 7(1):521-532.

Seborg, C.O., Stamm, A.J. (1931) Sorption of water vapor by paper-making materials I - Effect of beating. Ind. Eng. Chem. Res. 23(11):1271-1275.

Simpson, W. (1980) Sorption theories applied to wood. Wood Fiber Sci., 12(3):183 -195.

Skaar, C. (1972) Water in wood. Syracuse University Press, New York, pp218.

Somerville, C., Bauer, S., Brininstool, G., Facette, M., Hamann, T., Milne, J., Osborne, E., Paredez, A., Persson, S., Raab, T., Vorwerk, S. (2004) Toward a systems approach to understanding plant cell walls. Science. 306(5705):2206-221.

Spalt, H.A. (1958) The fundamentals of water vapor sorption by wood. F.P.J. 8(10): 288-295

Stamm, A.J. (1964) Wood and cellulose science. The Ronald Press Company, New York, pp549.

Stamm, A.J., Seborg, R.M. (1935) Adsorption compression on cellulose and wood. I. Density measurements in benzene. J. Phys. Chem. 39(1):133-142.

Steele, W.A. (1974) The interaction of gases with solid surfaces. Pergamon, Oxford, PP349.

Stevanic, J.S., Salmén, L. (2009) Orientation of the wood polymers in the cell wall of spruce wood fibres. Holzforschung. 63(5): 497-503.

Stone, J.E., Scallan, A.M. (1968) The effect of component removal upon the porous structure of the cell-wall of wood. Part III. A comparison between the sulphite and kraft processes. Pulp and Paper Mag. Canada. 69(6): 69-74

Suchy, M., Virtanen, J., Kontturi, E., Vuorinen, T. (2010a) Impact of drying on wood ultrastructure observed by deuterium exchange and photoacoustic FT-IR spectroscopy. Biomacromolecules 11:515-520.

Suchy, M., Virtanen, J., Kontturi, E., Vuorinen, T. (2010b) Impact of Drying on Wood Ultrastructure: Similarities in Cell Wall Alteration between Native Wood and Isolated Wood-Based Fibers. Biomacromolecules 11:2161–2168.

Tanaka, H., Hiratsuka, T., Nishiyama, N., Mori, K., Miyahara, M.T. (2013) Capillary condensation in mesoporous silica with surface roughness. Adsorption. 19(2-4):631-641.

Taniguchi, T., H. Harada, K. Nakato. (1978) Determination of water adsorption sites in wood by a hydrogen – deuterium exchange. Nature.72: 230-231.

TAPPI T 222 om-11, Acid-insoluble lignin in wood and pulp, 2011.

TAPPI T 249 cm-09, Carbohydrate composition of extractive-free wood and wood pulp by gas-liquid chromatography, 2009.

TAPPI UM 250, Acid-soluble lignin in wood and pulp, 1991.

Thommes, M., Köhn, R., Fröba, M. (2000) Sorption and pore condensation behavior of nitrogen, argon, and krypton in mesoporous MCM-48 silica materials. J. Phys. Chem. B.104 (33):7932-7943.

Tiemann, H.D. (1906). Effect of moisture upon the strength and stiffness of wood. US Dept. of Agriculture, Forest Service. Bull. 70.

Urquhart, A.R. (1929) The mechanism of the adsorption of water by cotton. J. Tex. Inst. 20:T 125-T132.

Van Dyke, B.H. (1972) Enzymatic hydrolysis of cellulose: a kinetic study, Ph.D. thesis, Massachusetts Institute of Technology, USA, pp330.

Vishnyakov, A., Neimark, A.V. (2001) Studies of liquid-vapor equilibria, criticality, and spinodal transitions in nanopores by the gauge cell Monte Carlo simulation method. J. Phys. Chem. B 105(29):7009-7020.

Vonk, C.G. (1973) Investigation of non-ideal two-phase polymer structures by small-angle X-ray scattering. J. Appl. Crystallogr. 6(2):81-86.

Walker, J.C.F. (2006) Primary Wood Processing: Principles and Practice (2nd Edition). Springer, Netherland, pp596.

Walther, J.H., Jaffe, R., Halicioglu, T., Koumoutsakos, P. (2001) Carbon nanotubes in water: structural characteristics and energetics. J. Phys. Chem. B. 105(41):9980-9987.

Wang, Q.Q., He, Z., Zhu, Z., Zhang, Y.H., Ni, Y., Luo, X.L., Zhu, J.Y. (2012) Evaluations of cellulose accessibilities of lignocelluloses by solute exclusion and protein adsorption techniques. Biotechnol. Bioeng. 109(2):381-389.

Willems, W. (2014) The water vapor sorption mechanism and its hysteresis in wood: the water/void mixture postulate. Wood Sci. Technol. 48(3):499-518.

Wilkerson, C.G., Mansfield, S.D., Lu, F., Withers, S., Park, J.Y., Karlen, S.D., Gonzales-Vigil, E., Padmakshan, D., Unda, F., Rencoret, J., Ralph, J. (2014) Monolignol ferulate transferase introduces chemically labile linkages into the lignin backbone. Science. 344(6179):90-93.

Wootters, A.H., Hallock, R.B. (2000) Hysteretic behavior of superfluid helium in Anopore. J. Low Temp. Phys. 121(5-6):549-554.

Xie, Y., Hill, C.A.S., Xiao, Z., Mai, C., Militz, H. (2011) Dynamic water vapor sorption properties of wood treated with glutaraldehyde. Wood Sci. Technol. 45:49- 61.

Zillig, W. (2009) Moisture transport in wood using a multiscale approach. Ph.D. Thesis, Katholieke Universiteit Leuven, Belgium, pp201.

Appendices

Appendix A

A.1 Congruency and wiping-out properties

Mayergoyz (1991) defined "congruency" and "wiping-out" properties to describe the specific geometric characteristics on hysteresis scanning curves. Let H_1 and H_2 be two H inputs with different past histories. Starting from some point of time, H_1 and H_2 vary back-and-forth between the same two consecutive extreme values: ω_- and ω_+ (Fig. A.1a).

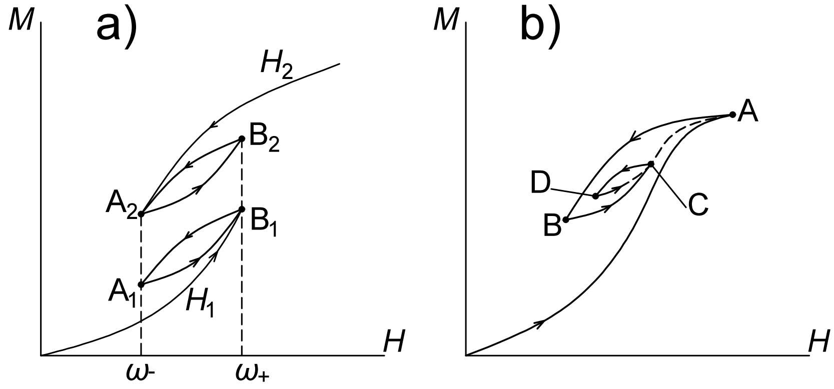

Figure A.1: Illustration of congruency, a) and wiping-out, b) properties defined by Mayergoyz (1991).

If hysteresis loops A_1B_1 and A_2B_2 from H_1 and H_2 have the same shape and size, these loops are defined as congruent. Wiping-out property means that each local input maximum H wipes out previous lower input maxima, and likewise each local input minimum wipes out previous higher local input minima. Fig. A.1b illustrates one example of this property. A – D denote the 1st to 4th reversing points on scanning curves. Starting from D, the 4th ascending curve returns to the track of the 2nd ascending curve (BCA) after passing point C as if the smaller sub-loop CD would not exist. Then, the curve returns to the boundary ascending curve after passing point A as if the bigger sub-loop AB would not exist. In this way, the history of loops CD and AB is wiped out.

Appendix B

B.1 Uncertainties of simulated sorption points in chapters 5 and 6

The uncertainty of simulated sorption points is evaluated by equally dividing the equilibrium Markov chain steps into 3 blocks and then calculating the standard deviation from the block average. Theoretically, when the system approaches phase transition, it becomes increasingly unstable. Correspondingly, the fluctuation of the system is largest at the phase transition point. To save computation time, only those sorption points close to the position of capillary condensation and evaporation were evaluated.

The error bars in Fig. B.1a indicate the uncertainties of simulated points for a 0.95 nm PW_1-wall pore at 25 °C. The vapor branches of the sorption isotherm are presented separately in Fig. B.1b with an expanded scale for a closer examination.

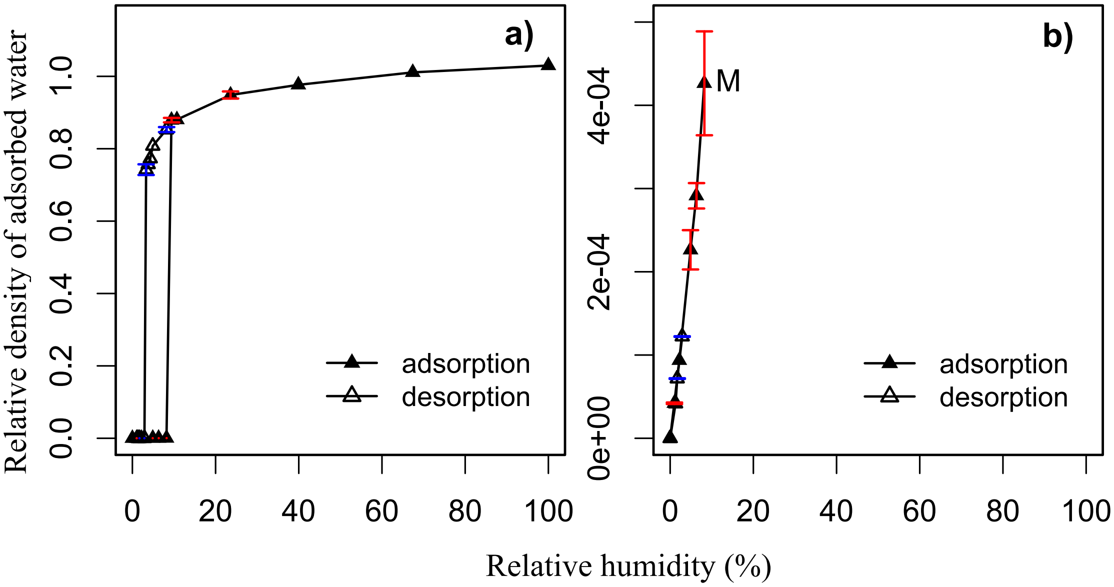

Figure B.1: a) Simulated sorption isotherms of PW_1 pore at 25°C with effective diameters of 0.95nm with error bars indicating standard deviations; b) partial curves before capillary condensation in a).

Indeed, as the points approach the position of capillary condensation or evaporation, the standard deviations become larger. The largest coefficient of variance (defined as standard deviation/mean) 14.64% comes from the adsorption point at H of 8.23% (Point M in Fig. A1b). Compared with variations in literature (Jorge and Seaton 2002, Panagiotopoulos 1987), the simulated data points in this study are satisfactory.

B.2 Reduced unit calculation in chapters 5 and 6

Following the unit convention in molecular simulation, reduced units normalized by LJ parameters of water-water interaction (ε_{ww} and σ_{ww}) were used in simulation.

Unit of length: σ_{ww};

Unit of energy: ε_{ww};

Unit of temperature: ε/k_B ($k_B = 1.38 \times 10^{-23}$ JK^{-1} is Boltzman constant);

Reduced length: $l^* = l/\sigma_{ww}$;

Reduced temperature: $\tau^* = \tau k_B/\varepsilon_{ww}$;

Reduced volume: $V^* = V/{\sigma_{ww}}^3$;

Reduced particle density (particle density is defined as N/V, where N is particle number and V is the volume): $\rho^* = \rho{\sigma_{ww}}^3$;

Reduced energy: $u^* = \frac{u}{\varepsilon_{ww}}$;

Reduced pressure: $p^* = p{\sigma_{ww}}^3/\varepsilon_{ww}$.

B.3 Pooled data for statistical modeling in chapter 6

Table B.1: Pooled simulation data for statistical modeling.

$\varepsilon_{\mathrm{sf}}$ (K)	r_p (nm)	n_{HB}	H_u (%)	H_l (%)	ΔH (%)
58.29	0.199	36	0.10	0.07	0.02
58.29	0.317	36	3.75	1.31	2.44
58.29	0.475	36	9.43	2.89	6.54
58.29	0.792	36	23.60	2.23	21.37
58.29	1.108	36	26.91	2.23	24.68
37.6	0.199	12	18.17	13.94	4.23
37.6	0.317	12	26.91	18.17	8.74
37.6	0.475	12	45.49	10.74	34.75
37.6	0.792	12	58.86	5.57	53.29
37.6	1.108	12	62.29	3.75	58.54
291.45	0.475	0	0.60	0.07	0.53
174.87	0.475	0	10.74	0.78	9.96
87.435	0.475	0	39.89	6.34	33.55
78.23	0.475	0	64.00	6.34	57.66
58.29	0.475	0	58.86	10.74	48.12
37.6	0.475	0	92.41	13.94	78.47
58.29	0.475	24	23.60	3.75	19.85
58.29	0.475	48	6.34	1.71	4.63
37.6	0.475	6	70.86	10.74	60.12
37.6	0.475	18	30.69	8.23	22.46